

Università degli Studi di Trieste

XXV Ciclo del Dottorato di Ricerca in Fisica

Dimensionality and ordering effects on the electronic structure of low dimensional strongly correlated electron transition metal oxides

Settore scientifico-disciplinare: FIS/03

Dottorando
Valentina Capogrosso

Coordinatore
Prof. Paolo Camerini

Supervisore
Prof. Fulvio Parmigiani

Co-Supervisore
Dr. Marco Malvestuto

Anno Accademico 2011/2012

Contents

Table of contents **ii**

1 Introduction **1**
1.1 Overview 1

2 State of the art **5**
2.1 Transition metal oxides 5
2.1.1 General properties 5
2.1.2 Crystal field theory 6
2.1.3 The Hubbard model 9
2.1.4 The Double-Exchange interaction 9
2.1.5 Low dimensional oxides 10
2.1.6 The 3*d* Manganites 11
2.1.6.1 Orbital Ordering 11
2.1.6.2 Charge Ordering 12
2.1.6.3 Magnetic ordering 13
2.1.6.4 The single layered half-doped $Pr_{0.5}Ca_{1.5}MnO_4$. 16
2.1.6.5 Photoinduced Phase Transitions: the case of Hidden Phase 17
2.1.7 The 4*d* Ruthenates 19
2.2 Soft X-ray spectroscopies 20
2.2.1 X-ray Absorption Spectroscopy 21
2.2.2 X-ray Emission Spectroscopy 21

3 Experimental tools **23**
3.1 Resonant X-ray Emission Spectroscopy 23
3.2 Soft X-ray Absorption Spectroscopy 25
3.2.1 Total Electron Yield Mode 29
3.2.2 Fluorescence Yield Mode 30
3.3 Time-resolved XAS 30
3.4 Time-resolved XAS apparatus at BACH beamline and T-ReX lab 33
3.4.1 The BACH beamline 33

3.4.2 Laser system at T-ReX lab . . . 37
3.4.3 Time resolved XAS setup . . . 38
3.5 Photoinduced surface semiconductor-metal transition in crystalline germanium . . . 42
3.5.1 Introduction . . . 42
3.5.2 Experimental procedure . . . 43
3.5.3 Results and discussion . . . 43

4 Theory and Modeling **49**
4.1 Introduction . . . 49
4.2 LDA and LDA +U . . . 51
4.3 WIEN2k: a tool for ab-initio electronic structure calculations and XAS spectra simulation . . . 53
4.3.1 Calculation of the Density of States . . . 54
4.3.2 Calculation of the X-ray Spectra . . . 55
4.3.3 Electron density plots . . . 55
4.4 Modeling PCMO . . . 56

5 Cases studied **63**
5.1 PCMO . . . 63
5.1.1 Adiabatic phase transition in PCMO . . . 63
5.1.1.1 Experimental procedure . . . 66
5.1.1.2 Results and Discussion . . . 67
5.1.1.3 Conclusions . . . 76
5.1.2 Time resolved XAS study of the 'hidden' photoinduced phase transition in PCMO . . . 76
5.1.2.1 Experimental procedure . . . 78
5.1.2.2 Results and Discussion . . . 78
5.2 Orbital structure evolution in the layered $Sr_{n+1}Ru_nO_{3n+1}$ (n=1,2,3) by means of RXES . . . 81
5.2.1 The Ruddlesden-Popper series of Sr Ruthenates . . . 81
5.2.2 Aim of this study . . . 84
5.2.3 Experimental procedure . . . 87
5.2.4 Results and discussion . . . 89
5.2.4.1 O *1s* edge spectra of SRO (n=1,2,3) . . . 89
5.2.4.2 RXES on the O *K* edge . . . 92
5.2.5 Conclusions . . . 96

6 Conclusions **97**

Bibliography **99**

List of publications **117**

Chapter 1

Introduction

1.1 Overview

Deepening into the physical properties of strongly correlated-electron materials is one of the major challenge of contemporary physics. These complex systems exhibit some of the most intriguing phenomena in condensed matter physics, such as superconductivity in cuprates or colossal magnetoresistance in manganites. The correlation of electrons in a solid produces a rich variety of states, by means of the many active degrees of freedom - spin, charge, lattice and orbital (see Fig.1.1) - which interact in a nonlinear, synergetic manner, leading to an intrinsic complexity.

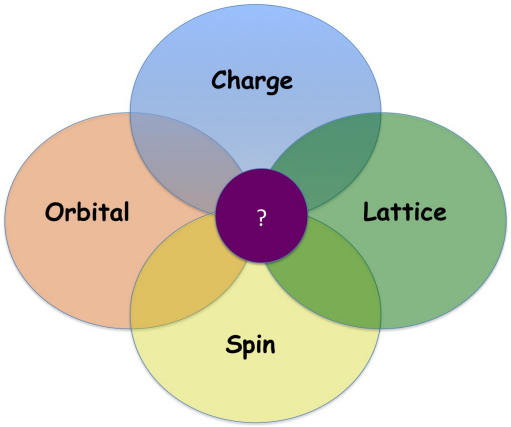


Figure 1.1: Cartoon of the coupling between the degrees of freedom (spin, charge and orbital) that dictate the properties of strongly correlated electron materials and give rise to their complexity.

In the vast scenario of strongly correlated-electron materials transition-metal oxides (TMOs) have attracted enormous interest because of their interesting physical properties. In particular, my interest was directed to a particular class

of materials, where *dimensionality* is one of the most important parameter. The two dimensional (2D) nature of layered materials commonly gives rise to interesting mechanical, magnetic, thermoelectric and electronic properties suitable for technological applications.
Several compounds belong to this class of layered materials, where crystal dimensionality plays a crucial role. Among them it is important to mention the copper oxides, whose layered structure is central for high-T_C superconductivity (HTSC) occurring in the CuO_2 planes.
Recently there has been a growing interest in the study of layered cobaltites of general formula $REBaCo_2O_{5+\delta}$ (RE=rare earth) which show a large oxygen non-stoichiometry. This degree of freedom allows a continuous doping of the square-lattice CoO_2 planes influencing the transport and magnetic properties. The members of this family show also thermoelectric behavior that make them very suitable for building thermoelectric devices.
Manganite compounds constitute another interesting family, where the most investigated phenomena are the colossal magnetoresistance (CMR) [1] and the charge or orbital ordering [2, 3], that take place in the MnO_2 layers.
Furthermore, ruthenates have emerged as an important family of perovskites because of the unexpected and unprecedented evolution from high-temperature isotropic ferromagnetism in $SrRuO_3$ to anisotropic ferro- or metamagnetic behavior of $Sr_4Ru_3O_{10}$ (n=3) dependent on the direction of the magnetic field, enhanced Pauli paramagnetism close to magnetic order of $Sr_3Ru_2O_7$ (n=2) and, finally, to low-temperature superconductivity in Sr_2RuO_4 (n=1) [4][5].
The goal of my Ph.D. thesis is to investigate the coupling between crystal dimensionality, which is strongly related to the lattice degree of freedom, and the electronic structure. This coupling can give rise to a charge, orbital and magnetic *ordering* and it is partly responsible of the complexities that characterize these layered oxides.
My experiments have been focused on two case-study systems: the single layered half-doped $Pr_{0.5}Ca_{1.5}MnO_4$ (hd-PCMO) and the layered $Sr_{n+1}Ru_nO_{3n+1}$ (n=1,2,3) family. In order to deepen into the physical properties of these systems the occupied and unoccupied density of states (DOS) of the valence and conduction band respectively, have been investigated. The chosen experimental tools are the X-ray emission spectroscopy (XES) and the X-ray absorption spectroscopy (XAS) technique.
Furthermore, on the basis of theoretical studies that predict the formation of transient *hidden* orbital and structural phases not thermally accessible, another goal of my studies has been to photoexcite a hidden metastable state in hd-PCMO. Pursuing this aim, I have measured the unoccupied DOS of the optically induced metastable state in hd-PCMO by means of time resolved XAS, which offers an innovative unique tool to measure site and symmetry projected DOS of metastable states in matter.
The second chapter of my Ph.D. thesis is divided into two sections. The first section introduces the reader into the orbital physics and the electronic phase

transitions in low dimensional transition metal oxides, with an excursus on the state of the art of $3d$ manganese compounds and the family of $4d$ Ruthenates. The second section is aimed to explain the importance of soft x-ray spectroscopic techniques as tools to investigate the electronic properties of solids. The description of X-ray absorption spectroscopy (XAS) and resonant X-ray emission spectroscopy (RXES) are reviewed in more details in chapter 3, which includes also the description of the experimental apparatus of BACH beamline and T-ReX lab at the Elettra synchrotron light source. Chapter 4 is dedicated to the Density Functional Theory (DFT) and Local Density Approximation plus U (LDA+U) theories and to the details of the modeling of the single layered half-doped $Pr_{0.5}Ca_{1.5}MnO_4$ (hd-PCMO) system. Chapter 5, which presents the cases studied, is divided into two sections: the case of PCMO, including static and time resolved XAS measurements, and the case of the Ruddlesden-Popper series of Sr Ruthenates investigated by means of RXES. In the final chapter the concluding remarks on this work are presented.

Chapter 2

State of the art

The first section of this chapter is dedicated to the physics of transition metal oxides. The second section is aimed to explain why soft x-ray spectroscopies, in particular x-ray absorption and x-ray emission spectroscopy, are particularly suitable to investigating the electronic properties of solids.

2.1 Transition metal oxides

Transition metal oxides (TMOs) form a series of compounds with a uniquely wide range of electronic properties. Some of these, the magnetism of lodestone and the colors of gems and minerals containing transition metals, have been known since antiquity. Other properties, especially the HTSC of mixed oxides containing copper, have been discovered only recently. Serious attempts to characterize and understand the electronic structure of TMOs began in the late 1930s, but these compounds continue to surprise in many ways, exhibiting a wide range of unusual and not yet sufficiently understood phenomena like dynamic lattice distortions, magnetic-, charge- and orbital-ordering.
Here below I will firstly go through the general properties of TMOs [6, 7]. I will present the most commonly used approaches to describe these compounds: the crystal field theory, the Hubbard model and the double exchange model. Then I will focus on low dimensional oxides, characterized by a reduced crystalline dimensionality. In the vast scenario of TMOs I will present, in particular, the families of $3d$ manganites and of $4d$ ruthenates.

2.1.1 General properties

The three transition series, shown in Fig.2.1, form the short groups of transition metal elements in the periodic table. The peculiarity, which distinguishes the transition metals from the main group metals (I-II), is the presence of unpaired d electrons, which are those involved in molecular bonding, and which determine the complex chemistry of transition metal compounds. All these

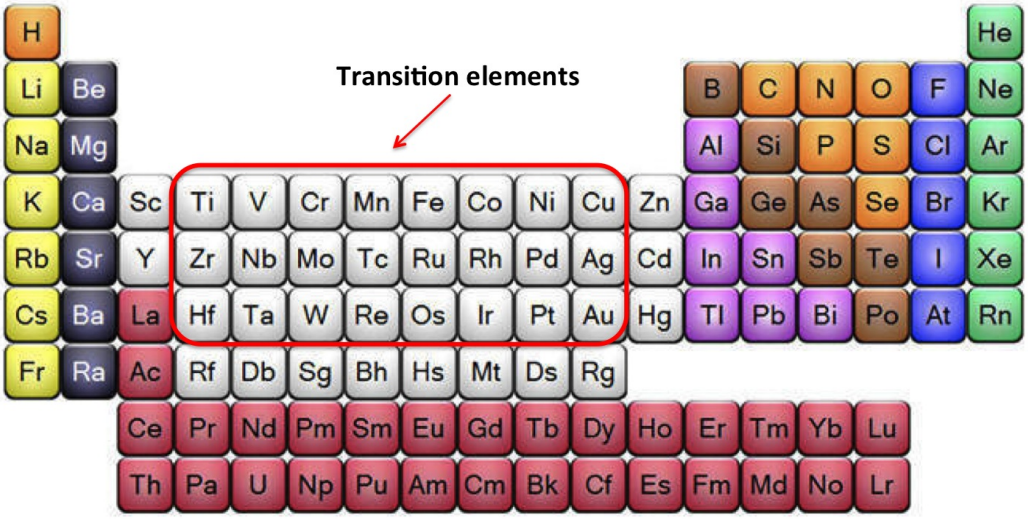


Figure 2.1: The periodic table of the elements. The red square underlines the transition elements.

compounds contain an element between Ti and Cu in the $3d$ series, between Zr and Ag in the $4d$ series, or between Hf and Au in the $5d$ series. TMOs are predominantly 'ionic' in their structural features: that is the closest interatomic distances are between metal and oxygen, and it is this metal-oxygen bonding that provides stability to the structure. The most significant geometrical factor, therefore, is the way in which a metal atom is surrounded by oxygen. The number of ligand atoms[1], which form bonds with the transition metal ion is often referred to as the *coordination number*, usually ranging from 4 to 6. The 4-coordinated complexes typically have a tetrahedral (T_d) or square-planar symmetry, whereas most of the 6-coordinated complexes exhibit an octahedral (O_h) symmetry. However, various distortions can be found as well.

2.1.2 Crystal field theory

A commonly used approach to describe the bonding of the transition metal complexes is the *crystal-field* (CF) theory. This theory implies an electrostatic approach, where the ligands are treated as negative point charges in the vicinity

[1]The neutral or anionic non-metal atom which surrounds and bonds to the transition metal atom is called *ligand*.

of the d-electrons of the transition metal ion. A representative picture of the 5 atomic d orbitals is illustrated in Fig.2.2. It shows the electron density

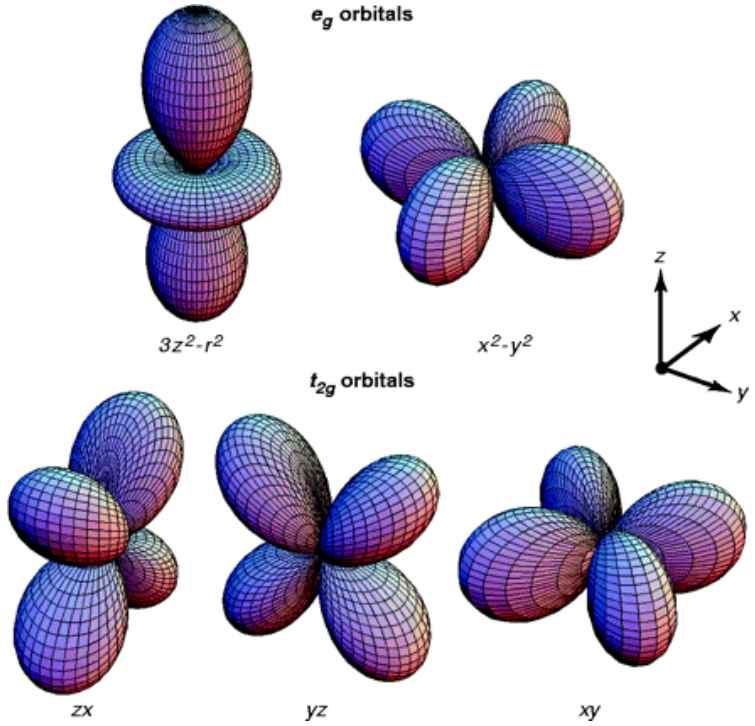


Figure 2.2: Transition metal d orbitals occur in 5 different forms as shown here [2]. Each of these d orbitals can accommodate 2 electrons, thus a total of 10 electrons can occupied in the d states. The orbitals d_{xy}, d_{yz} and d_{zx} are degenerate and are responsible for molecular bonding in T_d symmetry, whereas d_{z^2}) and $d_{x^2-y^2}$ are forming bonds in O_h symmetry.

associated with these orbitals in a Cartesian coordinate system, where the transition metal atom is placed at the origin, $(x, y, z) = (0, 0, 0)$. Three of the five orbitals (d_{xy}, d_{yz}, d_{zx}) are degenerate and are oriented between Cartesian axes. The remaining two orbitals (d_{z^2}) and ($d_{x^2-y^2}$), on the other hand, point along axes. The action of the ligands is treated, within perturbation theory, as an external electrostatic perturbation term, which has to be added to the total Hamiltonian describing the entire system, i.e. $H_{complex} = H_{atom} + H_{ligand}$, which distorts the spherical symmetry of the ionic metal d-levels and causes the energetic splitting between them. The symmetry of the ligands determines the degeneracy and relative energies of the ligand-field split ionic d-levels. In Fig.2.3 the examples in case of tetrahedral, octahedral and square planar ligand symmetries are shown. The energy splitting of the d-levels groups the five d-orbitals into 2 bands, namely t_{2g} and e_g. The d-orbitals that are oriented in-between the Cartesian axes in Fig.2.2 (i.e. d_{xy}, d_{yz}, d_{zx}) constitute the t_{2g} band. The e_g band contains the d-orbitals, which are directed along the Cartesian axes (i.e. $d_{x^2-y^2}$ and d_{z^2}). The parameter Δ, which describes the energetic gap between t_{2g} and e_g bands, is called the $crystal\text{-}field$ splitting, also denoted as $10Dq$. The effect of this parameter on the relative energies of the metal d-levels

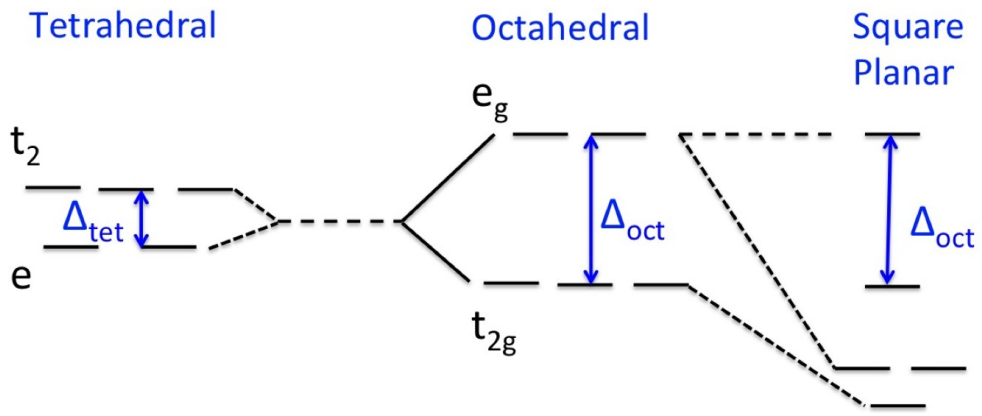


Figure 2.3: (From left to right)The energies of the d- orbitals in a tetrahedral, octahedral and square planar ligand crystal field. The electrostatic perturbation induced by the ligands causes the energy splitting Δ of the initially spherically symmetric metal levels, while the relative mean energy (as compared to the unperturbed free atom energy) remains unchanged.

can be described as follows. First, the strong repulsion of ligand electrons and metal electrons causes the initial destabilization of the d-levels. The splitting into t_{2g} and e_g bands stems from the rearrangement of the ligand electron pairs towards bonding directions. Finally, the electrostatic attraction between the ligand electron pairs and positive metal ion lowers the relative energies of the crystal-split d-levels, although the mean energy remains unchanged. The energy of a crystal field-state depends not only on the CF perturbation itself, but also on the various 'internal perturbations' that influence the energy of d^n states. At a formal level, a solution to the CF problem entails solving an eigenvalue problem, with the d orbitals as a basis, and the Hamiltonian

$$H = H_{CF} + H_{es} + H_{so}. \tag{2.1}$$

H_{CF} represents the CF splitting, H_{es} is the electrostatic repulsion between d electrons and H_{so} is the spin-orbit interaction. For $3d$ series the magnitude of spin-orbit effects is considerably smaller than the other terms. On the contrary, for $4d$ and $5d$ ions spin orbit coupling is stronger and can no longer be ignored. The CF and electrostatic terms are comparable in magnitude.

2.1.3 The Hubbard model

In TMOs the electron correlation term, which describes the way in which electrons alter their motion so as to avoid each other more effectively than an 'independent-electron' orbital wavefunction can describe, becomes important. The treatment of electron correlation, even in idealized models of simple metals, has a long and difficult history. An approximation especially useful in transition metal compounds is based on the ideas of Mott and Hubbard [8, 9], and consists of neglecting the repulsion between electrons except when they are on the same atom.
The *Hubbard model* takes into account the electron kinetic energy as well as electronic on-site interactions in a non-degenerate tight-binding band. In the second quantized form, the Hubbard Hamiltonian is given by:

$$H_H = H_t + H_U = -t \sum_{i,j} c^{\dagger}_{i,\sigma} c_{j,\sigma} + U \sum_{i} n_{i,\uparrow} c_{i,\downarrow}, \tag{2.2}$$

where $c^{\dagger}_{i,\sigma}$ and $c_{i,\sigma}$ are the creation and annihilation operators of an electron with spin σ [↑,↓] at site i. The symbols ↑ and ↓ denote spin-up and spin-down electrons, respectively. The occupation number operator writes $n_{i,\sigma}$=$c^{\dagger}_{i,\sigma}$ $c_{i,\sigma}$. The first term of the sum is the kinetic energy determined by the transfer integral t (*hopping term*). This is obtained from the overlap of two orbital wave functions at adjacent sites quantifying the probability that an electron moves from site i to site j. The second item describes the Coulomb repulsion of two electrons at the same site via the coupling strength U.

2.1.4 The Double-Exchange interaction

The concept of the double-exchange (DE) interaction was introduced by Zener [10] in order to explain the ferromagnetism of the perovskite manganites $AMnO_3$. The DE model describes the interplay of itinerant electrons in a partially filled band with magnetic moments localized at certain lattice sites. While accounting for an interband exchange interaction between the two subsystems, no direct exchange between the localized moments is regarded. The model Hamiltonian consists of two components:

$$H_{DE} = H_t + H_{Hund}. \tag{2.3}$$

While H_t represents the kinetic energy of the conduction electrons as in eq. above, H_{Hund} specifies Hund's exchange energy with coupling strength J_H (*exchange parameter*). This corresponds to an intra-ionic interaction between the conduction-electron spin σ^i and the localized magnetic moment S^i,

$$H_{Hund} = -J_H \sum_{i} \sigma^i S^i. \tag{2.4}$$

The positive sign of J_H determines the preferred ferromagnetic alignment of itinerant and localized spins. The double-exchange model predicts the ferromagnetic metallic phase as electron itineracy mediates ferromagnetic exchange

within the spin system. The spin scattering is not sufficient to reproduce the metal-insulator transition and there is substantial evidence that additional electron-lattice coupling is required to constitute the insulating state.

2.1.5 Low dimensional oxides

There is great interest in the low dimensional oxides (one-dimensional chain and two-dimensional layer compounds), which show spectacular anisotropy in their properties [11, 12]. In understanding the magnetic behavior of solids, it is necessary to take into account not only the dimensionality of the lattice [13, 14], but also the dimensionality of the spin or of the order parameter [13, 14], which together give rise to several possible types of magnetic system [15]. In addition, the coupling parameter J can be positive (ferromagnetic) or negative (antiferromagnetic), and this makes different types of system possible. The focus of my Ph.D. thesis is the study of 2D *layered materials*, where *dimensionality* is one of the most defining parameter. These materials are characterized by a reduced dimensionality associated to a particular direction which coincides with the direction of the metal-oxygen layers (see Fig.2.4). These planes are central to their electronic properties and the most part of the physical properties exhibited by layered materials is closely linked to this particular direction.

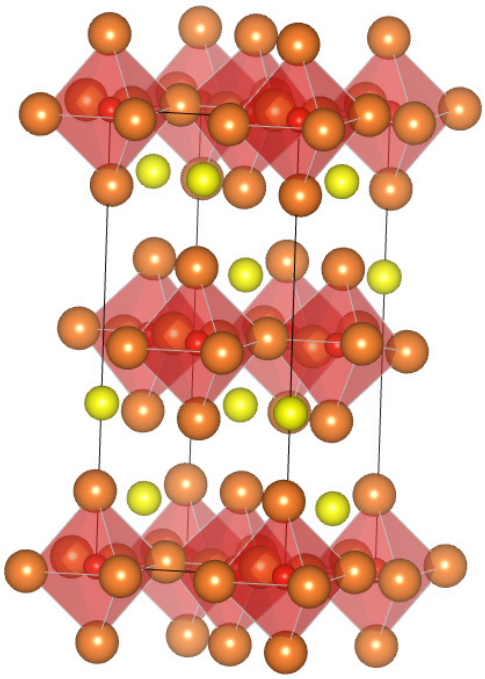


Figure 2.4: Generic layered crystal structure sketched by means of the three-dimensional visualization system VESTA.

The stacking of layers in a compound as well as the coordination of atoms in

the layer, layer thickness, and also symmetry and chemistry play a role in these materials. For instance, the standard charge transfer picture of copper oxides suggests that superconductivity occurs predominantly in the CuO_2 planes, while other (intercalated) layers behave as charge reservoirs [16]. However, the arguments were presented [17] that, in principle, it is possible to think that the intercalating metal oxygen layers are not just passive insulating layers, but are 'electronically active. In literature there exist various conflicting arguments on this subject.
Among several families belonging to this class of materials (briefly listed in the overview), the central issue of this work are the $3d$ layered manganites and the $4d$ layered ruthenates.

2.1.6 The $3d$ Manganites

The interesting phenomena in $3d$ TMOs originate from the competition between the localized nature of 3d orbitals and their bandwidth. Due to the relatively small radial extent of the wave function with respect to lattice parameters, $3d$-electron systems usually have a small overlap and narrow bandwidth. In the reduced bandwidth systems correlation among charge carriers plays an important role for their magnetic and electronic properties. The magnetic, charge and orbital ordering (described below) are representative phenomenona relevant to the long range Coulomb interaction among charge carriers [2, 3].

2.1.6.1 Orbital Ordering

Orbital ordering (OO) is an interesting phenomenon, where a real space ordering of the charge carriers in certain orbitals results from lattice distortion and Coulomb correlation of electrons. Two example of OO, where the orbitals are displaced in different zig-zag pattern, are sketched in Fig.2.5.

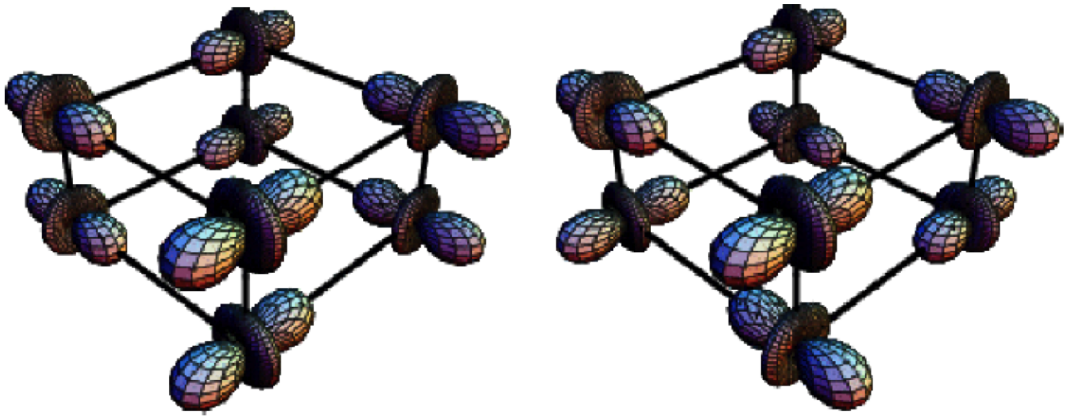


Figure 2.5: Schematic picture of the orbital ordering pattern that is observed in Jahn-Teller distorted $LaMnO_3$ and d-type $KCuF_3$ (left) and a-type $KCuF_3$ (right). The occupied orbitals are shown [18].

OO manifests itself in the site-dependent orientation of the quadrupole moment, as a result of the spatial distribution of the outermost valence d-electrons and it gives rise to the anisotropy of the electron-transfer interaction. This favors or disfavors the double-exchange interaction and the superexchange[2] (ferromagnetic or antiferromagnetic) interaction in an orbital direction-dependent manner and gives a complex spin-orbital coupled state. In the hole-doped manganese oxides, in which the double-exchange interaction emerges with the strength being dependent on the doping level, various orbital-ordered and disordered states show up, accompanying the respective spin-ordering features.

2.1.6.2 Charge Ordering

According to the *charge ordering* (CO) phenomenon, which was first envisaged by Eugene Wigner in the late 1930s, charges are localized on specific lattice sites leading to a disproportionation and an ordered superlattice. It appears in different patterns and occasionally accompanies the concomitant orbital ordering (OO), as it is schematized in Fig.2.6 for a manganite. It is often

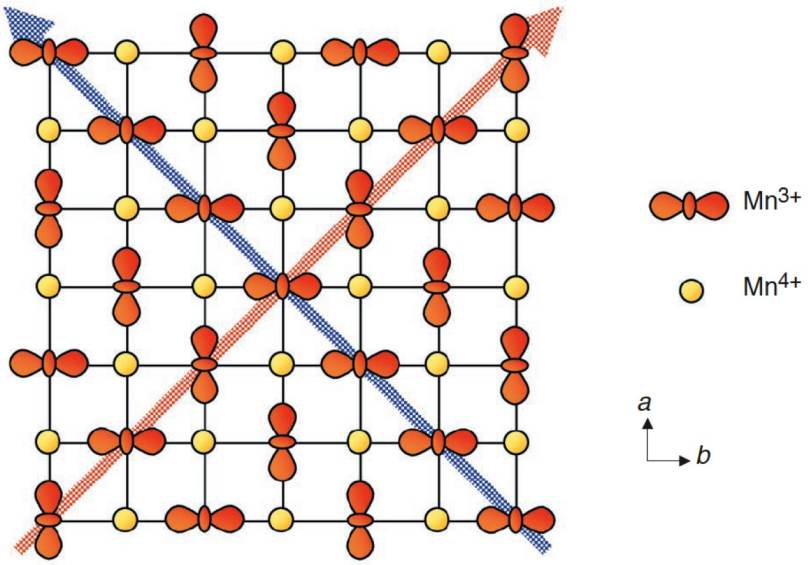


Figure 2.6: CE-type projected on the MnO_2 sheet (ab plane) for $La_{0.5}Sr_{1.5}MnO_4$ (LSMO) [2]. The different Mn^{3+} and Mn^{4+} charges are located in alternating lattice sites. The blue arrow distinguishes identical orbitals, while the red arrow distinguishes alternating orbitals; the charges are identical along both diagonals.

found in close proximity to superconductivity and colossal magnetoresistance

[2]Superexchange, or interaction between localized moments of ions in insulators that are too far apart to interact by direct exchange, operates through the intermediacy of a nonmagnetic ion (e.g. metal-oxygen-metal).

(CMR)[3], but there are also different cases as the case of hd-PCMO studied in this thesis.

2.1.6.3 Magnetic ordering

A well defined orientation of the spin in different lattice sites gives rise to the *magnetic ordering*. In Fig.2.7 two different kind of magnetic ordering are sketched: the ferromagnetic ordering (F) associated also to the $x^2 - y^2$ and $3z^2 - r^2$ orbital ordering; the antiferromagnetic ordering (A) associated to the $x^2 - y^2$ orbital ordering. The ferromagnetic case gives rise to two sub-lattices of metal ions with spin pointing in the same direction. On the contrary, the antiferromagnetic case gives rise to two sub-lattices of metal ions with spin pointing in opposite directions.

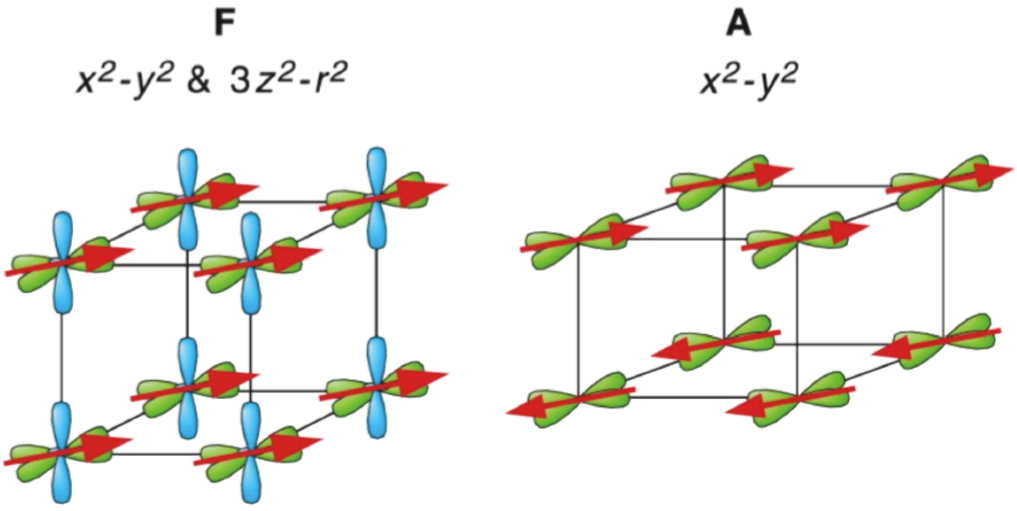


Figure 2.7: Two different kind of magnetic ordering are sketched: (on the left) the ferromagnetic ordering (F) associated also to the $x^2 - y^2$ and $3z^2 - r^2$ orbital ordering; (on the right) the antiferromagnetic ordering (A) associated to the $x^2 - y^2$ orbital ordering [2].

Magnetic ordering is a phase change associated with a discontinuity in the susceptibility; it may also involve a small change in lattice spacing and often in crystal symmetry. The commonest behavior in magnetic insulators is antiferromagnetism, where the susceptibility drops below the Neél temperature. Fig.2.8 illustrates this for the case of $R_{0.5}Ca_{1.5}MnO_4$ (RCMO) crystals.

Manganese oxides are prototypical of correlated electron systems where spin, charge, and orbital degrees of freedom are at play simultaneously, and where

[3]CMR, i.e. a very large decrease of resistance, is observed upon the application of an external magnetic field.

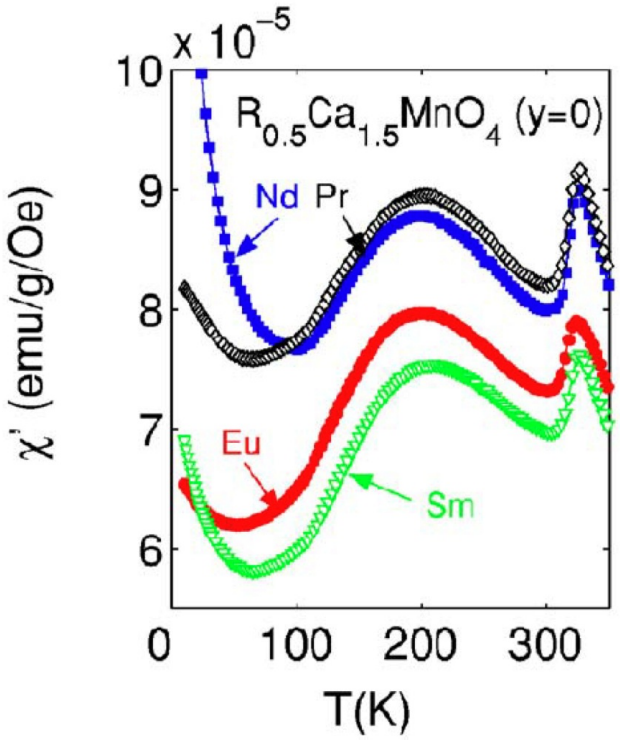


Figure 2.8: Temperature dependence of the in-plane component of the ac susceptibility χ for some of the $R_{0.5}Ca_{1.5}MnO_4$ (RCMO). In particular: R=Nd (blue curve); R=Pr (black curve); R=Eu (red curve); R=Sm (green curve) [19].

classical simplifications that neglect some interactions do not work [20]. Numerous reviews are available describing the properties and physics of manganites [2, 21–23].

A major motivation for the study of manganites is the richness of the low-temperature phases that emerge upon doping. The end members of the series, $RMnO_3$ and $DMnO_3$, where R is a rare-earth atom and D is a divalent substituent such as Ca or Sr, are antiferromagnetic insulators. $LaMnO_3$ and $CaMnO_3$, for example, were studied in some detail by Wollan and Koehler [24], more than 40 years ago with particular attention to the issue of orbital and spin ordering, examined more recently by Maezono et al. [25].

Upon doping, the manganites exhibit a wide variety of ordered states, including ferromagnetic and charge-ordered phases, in addition to the antiferromagnetism described before. In those compounds, in which the proportions of Mn^{3+} and Mn^{4+} ions are rational fractions (*mixed valency*[4]), CO and OO effects are particularly pronounced. Fig.2.9 reports CO-OO phase diagrams of various $R_{0.5}A_{0.5}MnO_3$ crystals (R and A are trivalent rare-earth and divalent

[4]Mixed valency means that an element is present in fractional oxidation states. Properties of mixed valency oxides are generally determined by the rate of electron transfer between the different oxidation states.

alkaline-earth ions, respectively).

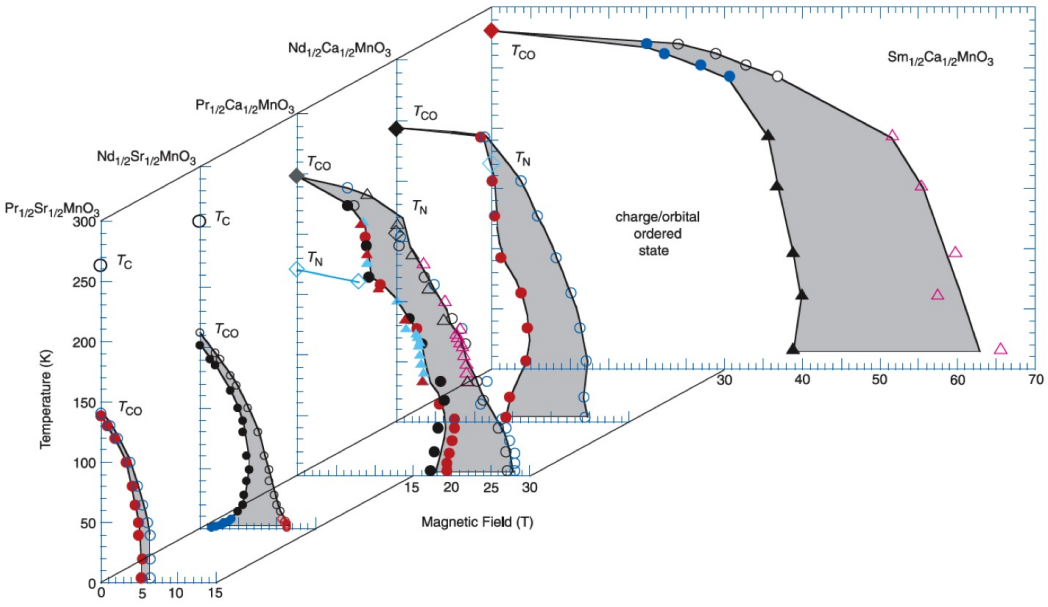


Figure 2.9: The charge/orbital-ordered phase diagrams in the plane of magnetic field and temperature for various $R_{0.5}A_{0.5}MnO_3$ crystals, R and A being trivalent rare-earth and divalent alkaline-earth ions, respectively. T_C, T_N and T_{CO} stand for the ferromagnetic, antiferromagnetic, and charge-ordering transition temperature, respectively [2].

With a decrease of the ionic radius, say from (Nd, Sr) to (Sm, Ca), the H-T region for the stable orbital/charge-ordered state is enlarged.
The 3D $AMnO_3$ are the end ($n = \infty$) members of the so-called Ruddlesden-Popper series $A_{n+1}Mn_nO_{3n+1}$ [26] (see Fig.2.10), where the MnO_6 octahedra are arranged in n planes, separated by two (Ln, A)O layers. Electrical conduction, magnetic correlation, and OO take place in the MnO_2 planes, and their number and separation determine physical properties. Similar to the $n = \infty$ case, intense and systematic research was renewed only after the discovery of large magnetoresistance [27, 28] in the $n = 2$ member, called *layered manganites*. Their physical properties, also related to the presence of both Mn^{3+} and Mn^{4+} ions placed in the center of an oxygen octahedron in the samples as in the case of the 3D compounds, are in addition anisotropic because the MnO_2 planes, where the magnetic correlations and electrical conductivity take place, are isolated by two AO planes [27].
In particular, CO-OO of half-doped manganites has attracted much attention [24, 29–33] and has been hotly debated [34–37].

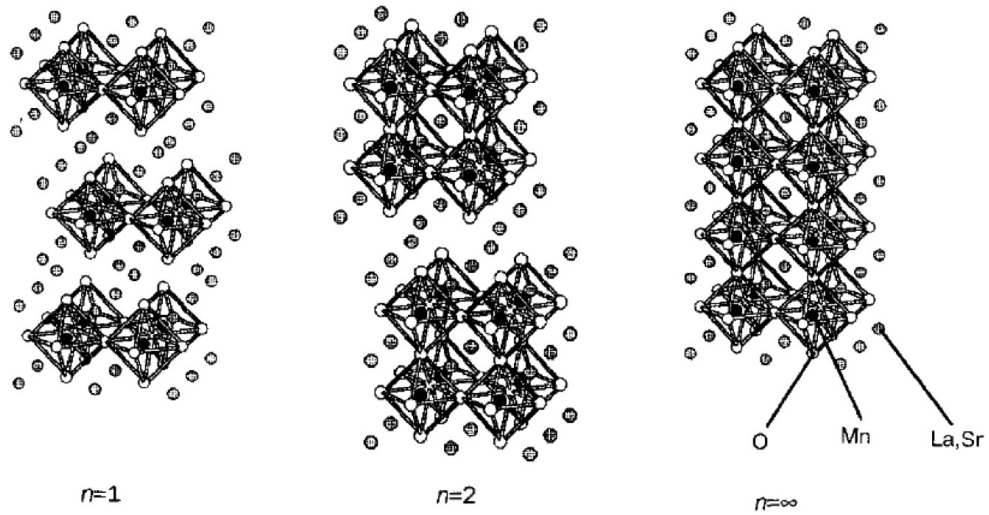


Figure 2.10: Structures of the $n = 1$, $n = 2$, and $n = \infty$ members of the Ruddlesden-Popper series of lanthanum manganites [27].

2.1.6.4 The single layered half-doped $Pr_{0.5}Ca_{1.5}MnO_4$

The single layered hd-PCMO is a case study for layered systems displaying charge, orbital and magnetic orderings. As it will be discussed in more details in Chapter 5, this system exhibits a CO-O transition at a remarkably high T_{CO} accompanied by an orthorhombic structural distortion. Below T_N=130K it develops checkerboard-like antiferromagnetic (AFM) order. The aim of the present study is to investigate, by changing temperature, the three different phases exhibited by the system by means of XAS linear dichroism (XLD) measurements.
Furthermore, on the basis of theoretical studies that predict the formation of transient *hidden* orbital and structural phases by optical stimulation (see below), another goal of this study has been to optically induce a metastable state in hd-PCMO by means of time resolved XAS, which offers a unique tool to measure site and symmetry projected DOS of metastable states in matter. This technique delivers information about the electronic transient structural changes, when interfaced with an ultrafast laser in a pump-probe scheme (described in Chapter 3) [38–40]. Moreover, XAS offers unique flexibility, since it is both element-selective and it can be applied to any kind of disordered or ordered systems.

2.1.6.5 Photoinduced Phase Transitions: the case of Hidden Phase

For many years, photoinduced phase transition (PIPT) phenomena have attracted particular interest. In these transitions, it is possible to generate not only a thermally accessible metastable state but also a *hidden* state of matter [41]. A first-order PIPT is required to generate a new state other than a higher-temperature phase, so different order parameters should be allotted to the original and photoinduced phases.
The most conventional method to form a free-energy barrier between two material phases is to couple two order parameters (e.g. P and Q) in their respective phases. The two phases, which can be exchanged by the PIPT, may have two sets of order parameters, e.g. (P_A, Q_B) and (P_B, Q_B), as shown in Fig.2.11. Even if only one of the order parameters is influenced by photoexcitation, an

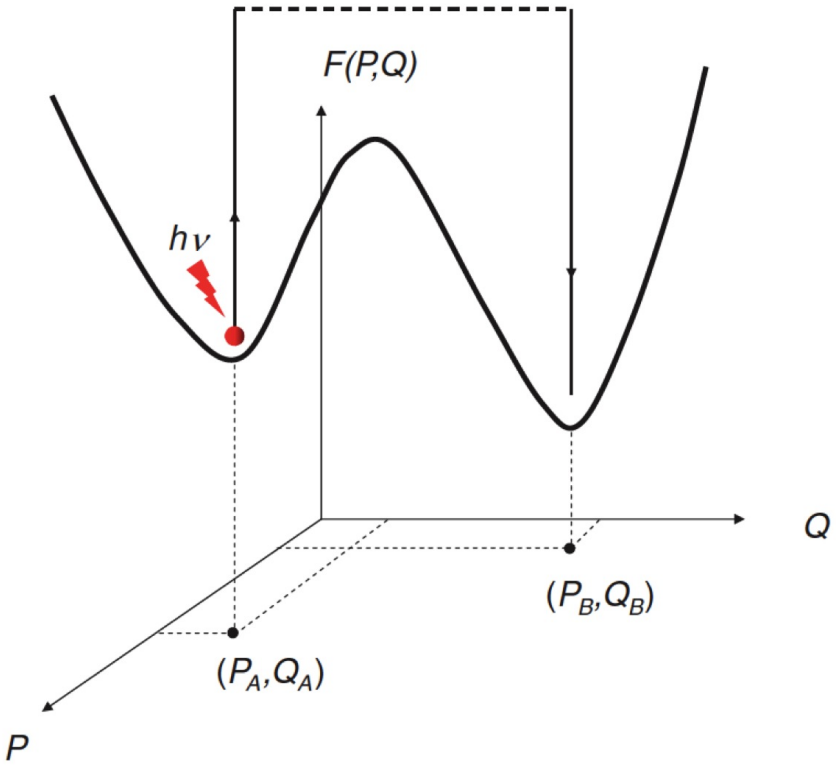


Figure 2.11: Free energy scheme exhibiting a potential barrier between two phases A and B characterized by a set of order parameters (P,Q) coupled biquadratically (see text)[41].

irreversible PIPT from phase A to phase B or vice versa may occur. This phenomenon is occasionally observed in the existing cases of PIPT since some type of electron-lattice interaction combines the specific electronic structure (P) with the crystal structure (Q), although only P can be directly modulated by photoexcitation.
Another strategy to induce the PIPT is to utilize bicritical (or multicritical) phase competition (Fig.2.12). When two different phases, e.g. phases A and B,

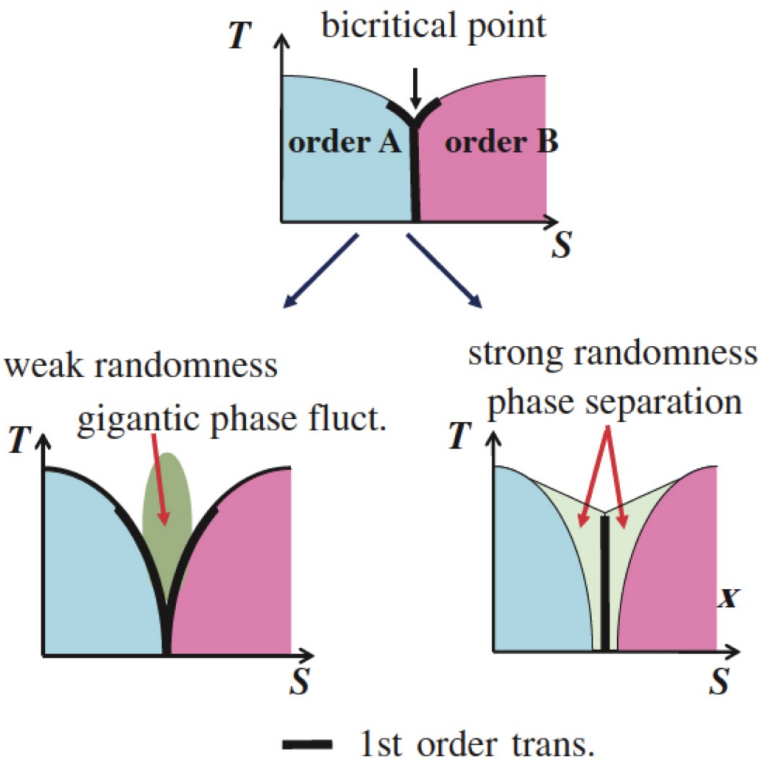


Figure 2.12: Bicritical competition between phases A and B with the control parameter S. The random potential originating from the quenched disorder produces a gigantic phase fluctuation characterized by the extended region of the first-order transition (weak disorder) or two-phase (A and B) coexistence at various length scales (strong disorder)[41].

with incompatible order parameters are in competition, a bicritical point can be obtained by tuning a control parameter (S). Two ordering temperatures T_A and T_B decrease toward the bicritical point because of the mutual suppression of their respective orders and eventually become equal at the same point. Around the bicritical point, the first-order phase transition region is extended, as shown by thick lines in Fig.2.12. When photoexcitation favors one of the competing phases in this bicritical region via the interaction of a photoexcited state with lattice, spin, orbital, or charge degrees of freedom, a dramatic phase conversion may occur either locally or globally. Such phase competition typically occurs in a correlated electron system in which multiple degrees of freedom of electrons - spin, charge, and orbital- are active to form various electronic and lattice phases.
Examples of PIPTs in terms of femto- and nanosecond pulse laser excitations [42–44] and X-ray irradiation have been for colossal magnetoresistance (CMR) manganites.

2.1.7 The 4*d* Ruthenates

The discovery of unconventional superconductivity in 4*d* layered Sr_2RuO_4 (n=1) [5] has initiated intense interest in 4*d* layered compounds because of the potential to discover novel phenomena. The single-layered ruthenate Sr_2RuO_4 has attracted much attention, both in its experimental and theoretical aspects, since it is an exotic material exhibiting triplet superconductivity in the solid state. By analogy with superfluidity in ^{3}He, the triplet superconductivity is believed to originate from ferromagnetic spin fluctuations enhanced by the Hund coupling [45].
There are several reasons that make this family of Ru oxides interesting [46]: (i) there are four electrons in the t_{2g} orbitals of the 4d level for Ru^{4+} and orbital degrees of freedom are active; (ii) the relativistic spin-orbit coupling (SOC) is reasonably large (161 meV for atomic value)[47], which may lead to various nontrivial effects in solids; and (iii) the electron correlation is moderately large leading to the various orderings.
Through the extensive investigations on ruthenates, after the discovery of the unconventional superconductivity in Sr_2RuO_4, a large understanding of the 4*d* TMOs has been accumulated. Numerous intriguing physical phenomena have been observed in the ruthenates and explained in terms of electron-electron interactions [48–50]. However, due to their more extended 4*d* orbitals, ruthenates should have weaker electron-electron interaction but stronger *p*-*d* hybridization effects than those of the 3*d* TMOs. In the perovskite ruthenates, a distortion in the RuO_6 networks results in a weakening of the π overlap between the oxygen *p* and the Ru t_{2g} orbitals. Such electron-lattice interactions, which are strongly coupled with the *p*-*d* hybridization, can be greatly enhanced due to the extended character of the 4*d* orbitals.
In addition to the triplet superconductivity, ruthenates exhibit complex magnetic properties and bear strong structural resemblance to the cuprate superconductors, with RuO_2 planes taking the place of the CuO_2 planes. Therefore, Ru 4*d* orbital occupation of the Ruddlesden-Popper series of strontium ruthenates ($Sr_{n+1}Ru_nO_{3n+1}$) have emerged as an important family of perovskites also because of the unexpected and unprecedented evolution from high-temperature isotropic ferromagnetism in $SrRuO_3$ to anisotropic ferro- or metamagnetic behavior of $Sr_4Ru_3O_{10}$ (n=3) dependent on the direction of the magnetic field and enhanced Pauli paramagnetism close to magnetic order of $Sr_3Ru_2O_7$ (n=2). An extensive description of these phases will be given in chapter 5.
When in Sr_2RuO_4 compound Sr is partially substituted by Ca, superconductivity is rapidly destroyed and paramagnetic metallic phase appears, while for $Ca_{1.5}Sr_{0.5}RuO_4$, a nearly FM metallic phase has been suggested. Upon further substitution, the system eventually transforms into an AFM insulator [51, 52]. The G-type AFM phase in Ca_2RuO_4 is characterized as a standard Neél state with spin S=1 [53]. A substantial orbital angular momentum has been detected in ruthenates [47, 54], suggesting the existence of spin-orbit coupling. These experimental facts denote that the orbital degree of freedom plays a crucial

role in the magnetic ordering. Moreover, the importance of magnetoelastic coupling has been experimentally pointed out [55]. Thus, these oxides belong to the family of 'spin-orbital-lattice' complex systems.
In the present thesis I will present the effect of dimensionality and crystal distortions on the electronic structure of $Sr_{n+1}Ru_nO_{3n+1}$ by means of polarization dependent X-ray absorption spectroscopy (XAS) and resonant X-ray emission spectroscopy (RXES) measurements. This comparative study could give insight into the comprehension of the physical properties of these compounds, which strongly depend on the number of RuO_6 octahedra layers in the unit cell.

2.2 Soft X-ray spectroscopies

Since their discovery in the year 1895 by Wilhelm Conrad Rontgen, x-rays have become an indispensable tool for studying the structure and electronic properties of matter. Equally important is the role x-rays have come to play in medicine, archeology, art, security, astronomy and other applications. The x-rays are assumed to be used as a weak, essentially nonperturbative *probe*.
Since the development of second generation synchrotron radiation sources in the 1970s, the use of x-rays has expanded widely.
The most characteristic feature of an x-ray is that it excites a core electron. In fact, in order to excite core electrons, we need the incident photons with energies larger than the core level binding energies (up to about 30 keV), which belong mainly to the x-ray region: soft x-rays up to 2 keV and hard-x-rays at higher energies.
X-ray spectroscopy has opened a new door on core level spectroscopy, which is a powerful tool for the study of electronic states in solids where the precise information of valence electron states can be detected through excitation of core electrons with a local and sensitive probe. A direct implication is that the information on core level spectroscopy is local and element specific. The experimental study of core level spectroscopy has made remarkable progress using high-brilliance third-generation synchrotron radiation sources.
In X-ray spectroscopy, transitions are involved in absorption (XAS, X-ray absorption spectroscopy) or emission (XES, X-ray emission spectroscopy) of X-rays, where the former probes the ground state to the excited state transitions, while the latter probes the decay process from the excited state. Both methods characterize the chemical nature and environment of atoms in molecules, and synchrotron sources provide a range of X-ray energies that are applicable to most elements in the periodic table. Here below I will briefly explain why these techniques are useful tools to investigate electronic properties of solids. A more detailed treatment of these spectroscopic techniques will be given in the next chapter.

2.2.1 X-ray Absorption Spectroscopy

In XAS a core electron is excited near to the threshold by the incident x-ray through the electric dipole transition. Since the core electron state is well-known, the XAS spectrum provides us with important information on the symmetry-projected partial density of states (P-DOS) of the excited states. The projected symmetry depends on the symmetry of the core electron states and the selection rule of the photo-excitation including the polarization of the incident x-ray.
XAS is element specific, so one can focus on one element without interference from other elements present in the sample. Another advantage of XAS is the fact that it is not limited by the state of the sample, because it is sensitive only to the local element site structure. The sample can be prepared as a powder, a solution or as a frozen solution for biological samples. It is not necessary to obtain single crystals of the material to examine the local structure of the metal. However, having oriented crystals such as membranes and single crystals significantly increases the structural information obtained from the XAS method.

2.2.2 X-ray Emission Spectroscopy

XES is a technique that is complementary to XAS and that provides valuable information with respect to the electronic structure (local charge- and spin-density) as well as the ligand environment of a $3d$ transition metal. XES is actually a consequence of the absorption of a photon and is therefore often referred to as a secondary process. In XES, the electron hole that was created in the X-ray absorption process is filled by an electron from a higher orbital. Therefore an emission spectrum is related to the density of occupied states. In XES, the system under study is excited with X-rays of sufficient energy to remove an inner-shell (core) electron of the element of interest. This leaves the absorbing atom in an excited state with a core hole, which is then immediately filled ($\tau \sim 10^{-15}$s) by an electron from an outer shell. In the de-excitation either an electron or a fluorescence X-ray photon is emitted, and in XES the fluorescence photon is measured. The energy scheme in Fig.2.13 simply states the law of energy conservation. Also XES, as XAS, is characterized by a high sensitivity to the local atomic structure.
By means of a synchrotron radiation source it is possible to tune the incident energy in the vicinity of the absorption edge and the fluorescence lines start showing a dependence on the incident energy. This is the phenomenon of resonant x-ray emission spectroscopy (RXES). XES and RXES are powerful, element specific techniques to study the local structure in a wide range of systems including $3d$ transition metal complexes [57].

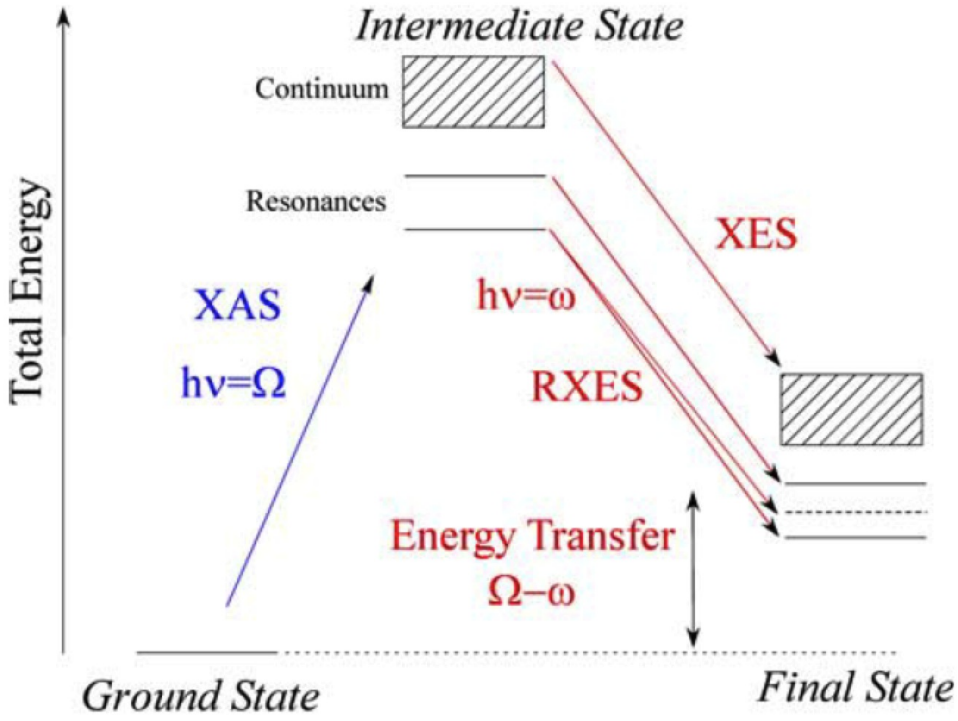


Figure 2.13: Simplified energy scheme for absorption of a photon with energy Ω and emission of a photon with energy ω. The total energy including all electrons of the system is plotted on the vertical axis. The energy transfer is the difference between the energies of the absorbed and the emitted photon. The dashed line in the final state denotes an electronic states that arises from the interaction of the core hole with the valence electrons. In XAS the incident energy Ω is scanned while XES analyzes the emitted energy ω. The difference energy Ω-ω is the energy transfer or final state energy [56].

Chapter 3

Experimental tools

In this chapter I will present the X-ray spectroscopic techniques (RXES, XAS and time resolved XAS), that have been used as tools in order to investigate the electronic properties of the systems under study. Then I will describe the three endstations of BACH beamline, the regenerative amplifier laser system at T-ReX laboratory and, in more details, the time resolved XAS experimental apparatus. The last section is dedicated to the photoinduced surface semiconductor-metal transition in crystalline germanium, used as a proof of principle for the time resolved XAS apparatus.

3.1 Resonant X-ray Emission Spectroscopy

In the x-ray emission process, a core hole is created in a core level c by incident x-ray beam and a valence electron or a core electron in the core level higher than c makes a radiative transition to the core level c by emitting an x-ray photon [57]. When the incident x-ray energy resonates with the excitation threshold of the core electron, the process is called resonant x-ray emission (RXES). Differently from XAS and XPS processes, this spectroscopy is a coherent second-order optical process, thus the intensity of the signal is lower. By means of RXES spectroscopy, it is possible to obtain bulk-sensitive, element-specific and site-selective information. The polarization dependence in RXES gives important information on the symmetry of the electronic state. Formally the spectroscopy can be described by means of an x-ray photon with energy $\hbar\Omega$ (wavevector $k1$) and polarization $\lambda 1$ incident on a material and, then, an x-ray photon with energy $\hbar\Omega$ (wavevector $k2$) and polarization $\lambda 2$ emitted as a result of the electron-photon interaction in the material. Taking into account the interaction up to the second-order perturbation term, the differential scattering cross section can be written as:

$$\frac{d^2\sigma}{d\Omega_{K_2} d\hbar\Omega} = \frac{(\hbar\omega)^2}{c^4}\Big(\frac{1}{2\pi}\Big)^3 W_{12} \tag{3.1}$$

where $d\Omega_{K_2}$ is the solid angle of the scattered light and W_{12} is the transition rate given by:

$$W_{12} = \frac{2\pi}{\hbar}\sum_j \frac{(2\pi)^2}{\Omega\omega}\Big(\frac{e^2\hbar}{mV_s}\Big)^2\delta(E_g+\hbar\Omega-E_j-\hbar\omega)$$
$$\times|\Big[< j|\rho_{k_1-k_2}|g > (e_1\cdot e_2)+\frac{1}{m}\sum_i\Big(\frac{< j|p(k_2)\cdot e_2|i >< i|p(-k_1)\cdot e_1|g >}{E_i-E_g-\hbar\Omega}+$$
$$\frac{< j|p(k_1)\cdot e_1|i >< i|p(-k_2)\cdot e_2|g >}{E_i-E_g+\hbar\omega}\Big)\Big]|^2. \tag{3.2}$$

Here |g>, |i> and |j> are initial, intermediate and final states of the material system, respectively E_g, E_i and E_j are their energies , and e_1 and e_2 are polarization directions (unit vectors) of incident and emitted photons. p(k) and ρ_k are defined by:

$$p(k) = \sum_n p_n exp(-ik\cdot r_n),$$
$$\rho_k = \sum_n exp(-ik\cdot r_n). \tag{3.3}$$

A schematic representation of the three terms in the square bracket of W_{12} is shown in figure 3.1.

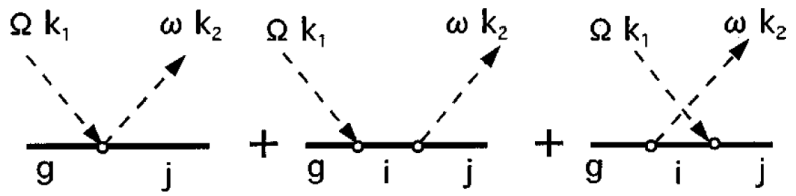


Figure 3.1: Schematic representation of three scattering terms [57].

The first term is the elastic Thomson scattering, which comes from the first order perturbation of the A^2-type interaction. The second and the third term

come from the second order perturbation. When the incident photon energy is close to or above the core electron excitation threshold, the contribution of the second term becomes dominant. In particular in the case of RXES, above the threshold, the denominator $E_i - E_g - \hbar\Omega$ vanishes and, thus, in order to remove this divergence, we take into account the finite lifetime of the intermediate-state core hole ($\tau_i = \hbar/\Gamma_i$). We can describe the most essential part of the RXES spectrum in the form:

$$F(\Omega,\omega) = \sum_j |\sum_i \frac{< j|T_2|i >< i|T_1|g >}{E_g + \hbar\Omega - E_i + i\Gamma_i}|^2 \delta(E_g + \hbar\Omega - E_j - \hbar\omega), \qquad (3.4)$$

where the operators T_1 and T_2 represent the radiative transitions by incident and emitted photons, respectively, and Γ_i represents the spectral broadening due to the core-hole lifetime in the intermediate state. If we consider the optical dipole transition, T_i (i=1,2) is given by:

$$T_i = p(0) \cdot e_i. \qquad (3.5)$$

3.2 Soft X-ray Absorption Spectroscopy

X-ray absorption is a synchrotron-based characterization technique since it requires the measurement of the X-ray absorption coefficient as a function of photon energy. During the x-ray absorption process a core- electron is excited into an empty state, so this technique allows to probe the unoccupied part of the electronic structure of the system (as sketched in Fig.3.2). An important aspect of the usefulness of this experimental technique is that it allows to obtain element-selective information [58]. The outcome of such XAS experiment delivers the characteristic x-ray absorption spectrum (Fig.3.3), where the variation of the absorption coefficient shows several general features [59] with a sharp rise at discrete energies, called *absorption edges*. The energetic positions of these features are unique for a given absorbing element. They occur near the ionization energy of inner shell electrons and contain spectral features due to bound-bound and bound-continuum transitions. The absorption edges are related to the transitions from a particular atomic core-orbital to the free continuum (ionization of core orbitals, Fig.3.4), but also include transitions to unoccupied bond levels just below the ionization limit. The nomenclature for x-ray absorption features reflects the core orbital, from which the absorption originates. In Fig.3.4, the two innermost core orbitals are shown namely the K and L shells and the characteristic transitions to the continuum states are indicated. For example, K edges refer to transitions from the innermost $n = 1$ electron orbital (thus the K edge involves $1s$ electron), whereas L edges refer to the $n = 2$ absorbing electrons (L_1 to $2s$, L_2 to $2p_{1/2}$, and L_3 to $2p_{3/2}$ orbitals), to the corresponding higher-lying bound core shells and continuum states. The transitions are always referred to unoccupied states, i.e., to states with an electron above the Fermi energy E_f, leaving behind a core hole, and absorption

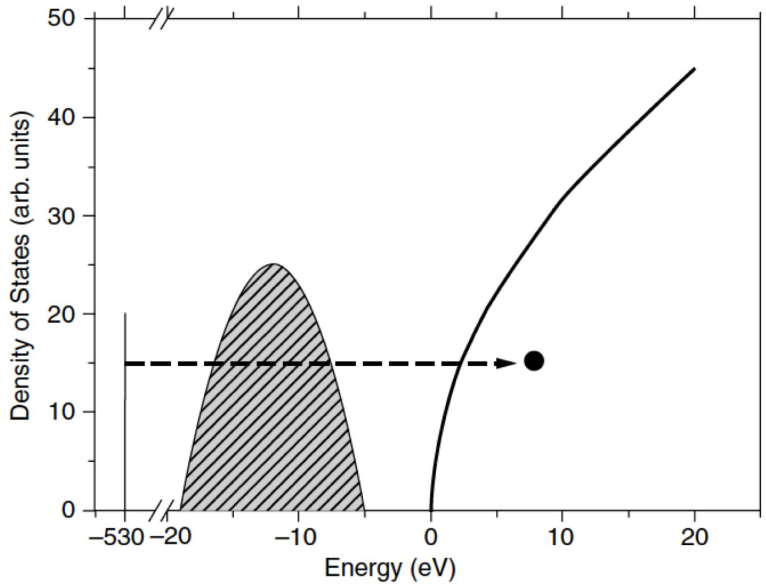


Figure 3.2: Schematic density of states of an oxide [57]. The 1s core electron at 530 eV binding energy is excited to an empty state: the oxygen projected density of states.

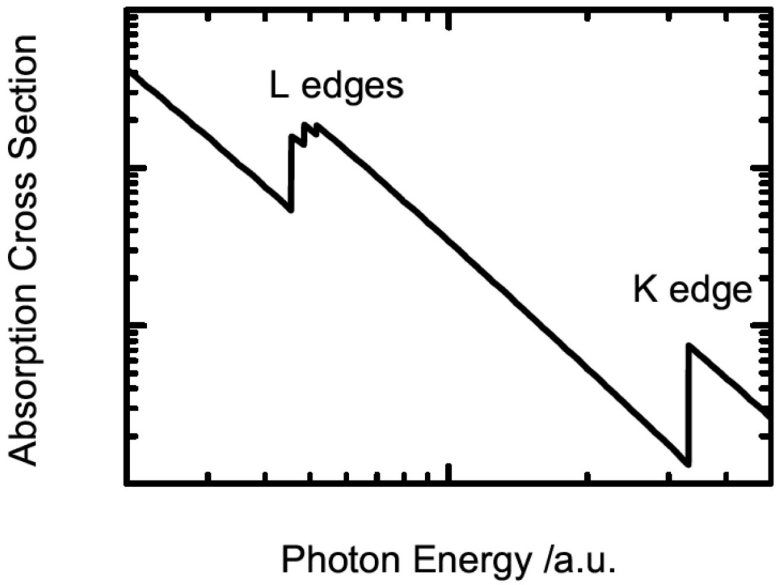


Figure 3.3: Variation of the atomic x-ray absorption coefficient as a function of the photon energy. The characteristic saw-tooth-like features with a sudden increase of the absorption at certain energies represent the absorption edges.

features may appear just below the edge, which correspond to transitions to bound unoccupied levels just below the ionization limit. Above the ionization limit, the excited electron is considered as a photoelectron, and depending on its kinetic energy, it can propagate more or less freely through the material.

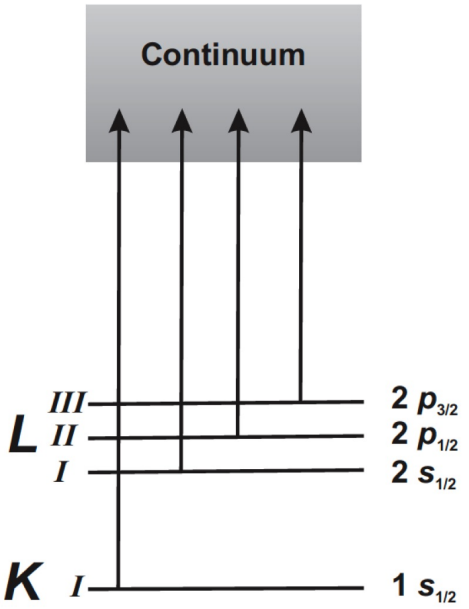


Figure 3.4: Transitions resulting from the absorption of an x-ray photon by the deep-core electron. The ionized photoelectron can be excited to either higher-lying unoccupied state or into the continuum. Here the transitions are shown for all possible $1s$ and $2p$ core excitations, i.e. K and L absorption edges.

The photoelectron propagation can be approximated by a spherical wave with a kinetic energy E_{kin} given by $E_{kin} = \hbar\omega - E_B$, where $\hbar\omega$ defines the incident x-ray photon energy and E_B refers to the binding energy. The photoelectron wave vector can be calculated via [60]:

$$k = \frac{2\pi}{\hbar}\sqrt{2m_e(\hbar\omega - E_B)} \tag{3.6}$$

The x-ray spectra, that will be shown later, have been collected by means of the total electron yield method, according to which all electrons that emerge from the sample surface are detected, independent of their energy.
The X-ray absorption spectral shape reproduces the unoccupied density of states (DOS) $\rho_{empty}(E)$ (where E indicates the binding energy inside the sample) projected into the excited atomic site via the dipole selection rules[1]. The x-ray absorption probability is described via the Fermi Golden rule by:

$$W_{fi}^{XAS}(\hbar\omega) \propto |M_{fi}|^2 \rho_{empty}(E)\delta(E_f - E_i - \hbar\omega) \tag{3.7}$$

where $\hbar\omega$ is the photon energy, M_{fi} is the dipole matrix element and the delta function takes care of the conservation of energy. The dipole matrix element is defined as

$$M_{fi} = < \phi_f | H_{int} | \phi_i >, \tag{3.8}$$

[1]The dipole selection rules $l \longrightarrow (l \pm 1)$ account for the momentum conservation in the photon absorption process.

where ϕ_i and ϕ_f are the wavefunctions of the initial and final state respectively, and H_{int} is the perturbation Hamiltonian due to the interaction with the photon given by:

$$H_{int} = \frac{e}{2mc}(\vec{A}\cdot\vec{p} + \vec{p}\cdot\vec{A}) = \frac{e}{mc}\vec{A}\cdot\vec{p}, \tag{3.9}$$

where $\vec{p}$ is the electronic momentum operator and $\vec{A}$ the electromagnetic vector potential. By means of the commutation relation $\hbar\vec{p}/m = -i[\vec{x}, H]$, the matrix element can be rewritten as:

$$M_{fi} \propto < \phi_f|\hat{e}\cdot\vec{p}|\phi_i > \tag{3.10}$$

where $\hat{e}$ is the unit vector along the polarization direction of the vector potential $\vec{A}$.
Rewriting the operator $\vec{p}$ in terms of $\vec{r}$, the matrix element can be written as:

$$M_{fi} \propto e_q < \phi_f|\hat{e}\cdot\vec{r}|\phi_i > \tag{3.11}$$

where e_q is the electron charge.
A great asset of XAS spectroscopy is its polarization dependence. Linearly polarized x-rays are best suited for covalent systems like low-Z molecules, macromolecules and polymers, which possess directional bonds. In this case the directional electric field vector of the x-rays can be viewed as a "*searchlight*" that can look for the direction of chemical bonds of the atom selected by its absorption edge. The X-ray Linear Dichroism (XLD) effect is that discussed in conjunction with Fig.3.5 (see details in the caption). In a more general formulation, the x-ray absorption intensity of linear polarized x-rays directly probes the quadrupole moment of the local charge around the absorbing atom through a *search-light-like* effect. A quadrupole moment exists in all cases where the local charge has lower than cubic symmetry. The absorption intensity is at a maximum if the x-ray electric field vector is aligned along the direction of maximum charge (hole) density in the atomic volume surrounding the absorbing atom, e.g. along an empty molecular orbital. The XLD effect provides the basis for the determination of the orientation of chemisorbed molecules on surfaces and the orientational order in polymers or liquid crystals. Here one determines the average orientation of a selected molecular orbital. The measured angular dependence determines the quadrupole moment or order parameter of the charge distribution of the selected orbital [61].
XLD is defined as the difference between XAS spectra taken with the electric field E vector of photons perpendicular and parallel to an orientation axis, for example the z-axis, i.e.:

$$XLD = XAS_{E\|z} - XAS_{E\perp z}. \tag{3.12}$$

XLD is a powerful experimental tool, as anticipated in the introduction, in determining the nature of orbital ordering in $3d$ transition-metal oxides. Experimentally, this type of measurement can be realized in different ways, each

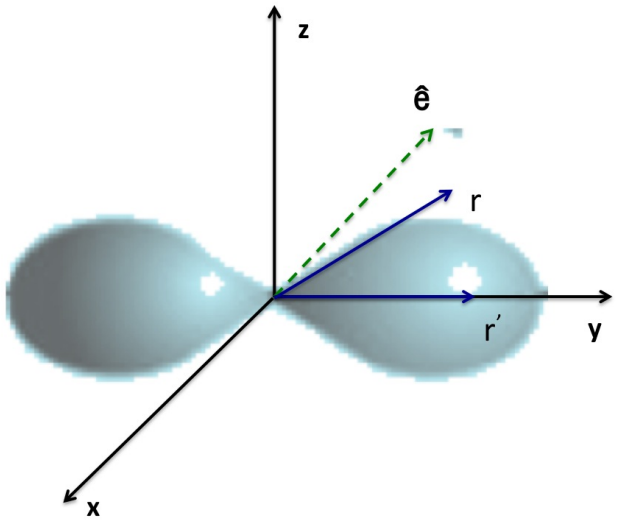


Figure 3.5: The p_y molecular orbital plotted in the Cartesian reference system. The blue line r represent the chemical bonding direction. The dashed green line is the ê versor, which indicates the light polarization direction.

with its own advantages and disadvantages. The two most commonly XAS detection modes, that will be discussed below, are the total electron and fluorescence yield modes. The total electron and fluorescence modes have been used to deliver the static XAS measurements and the time-resolved XAS measurements on hd-PCMO, respectively.

3.2.1 Total Electron Yield Mode

With the total electron yield method (TEY), all electrons that emerge from the sample surface are detected, independent of their energy, so the TEY signal contains contributions from primary, Auger and secondary electrons[2]. No device to select the electrons of a particular energy is needed and the current is easily measured and represents the XAS signal. A number of detection devices can be used such as the pico-ampere meter for detecting the current flowing to the sample, and the channeltron for amplifying the emitted electrons to a detectable signal.
The interaction of electrons with solids is much larger than the interaction of x-rays, which implies that the electrons that escape from the surface must

[2]Secondary electrons are due almost entirely to inelastic scattering of Auger electrons.

originate close to the surface.
The probing depth of TEY lies in the range of approximately 3-10 nm, depending on the material studied.
The TEY x-ray absorption cross section (I_{TEY}) is given by the following formula:

$$I_{TEY}(\Omega) \propto \frac{\lambda_e}{\lambda_e + \lambda_p(\Omega)\sin\alpha} \tag{3.13}$$

where λ_e is the electron escape depth, $\lambda_p(\Omega)$ is the frequency-dependent x-ray penetration depth and α is the angle of incidence. This formula implies that if $\lambda_e \ll \lambda_p \sin\alpha$, the TEY is inversely proportional to λ_p, and hence, proportional to the absorption coefficient. At the maximum absorption and/or at grazing incidence, saturation effects can occur.

3.2.2 Fluorescence Yield Mode

In the x-ray fluorescence process, a high-energy photon is emitted due to the recombination process between the core hole created upon the x-ray photo absorption and the electrons occupying the (nearest) higher lying shells, which have the largest orbitals overlap and are dipole-allowed. The possible transitions are labeled according to the nomenclature as illustrated in Fig.3.6. In this picture, a K-shell excitation is followed by spontaneous emissions from the $n \geq 2$ shells to n=1, as well as subsequent emissions from $n \geq 3$ to n=2, which occur in a cascade. An L-shell excitation induces transitions from $n \geq 3$ to $n = 2$, and from $n \geq 4$ to $n = 3$, and so on.

3.3 Time-resolved XAS

Extending XAS to the time domain implies that we can obtain dynamical informations on the transient and metastable states and on the orbital and spin momenta.
It is straightforward to mention that in XAS the processes of ejection, backscattering and interference are extremely fast. For inner shell electrons with ionization energies above 1 keV, these processes are completed within 1 fs, as can be seen from the measured homogeneous line widths of the absorption edges. This means that XAS takes an instantaneous snapshots of immobile atoms and, therefore, underlines the importance of time-resolved XAS technique [40].
The time-resolved XAS technique provide a powerful mean for obtaining new data and knowledge on the structure of short-lived excited states. By combining ultrafast optical electron and x-ray pulses, it is possible to study in deep the ultrafast phenomena, processes and transients that determine the course and affect the final product of an excitation process in solids and liquids [62–69].
The elemental specificity and penetration power of x-rays can allow for *in-situ* measurements of systems in complex or disordered environments. There are a

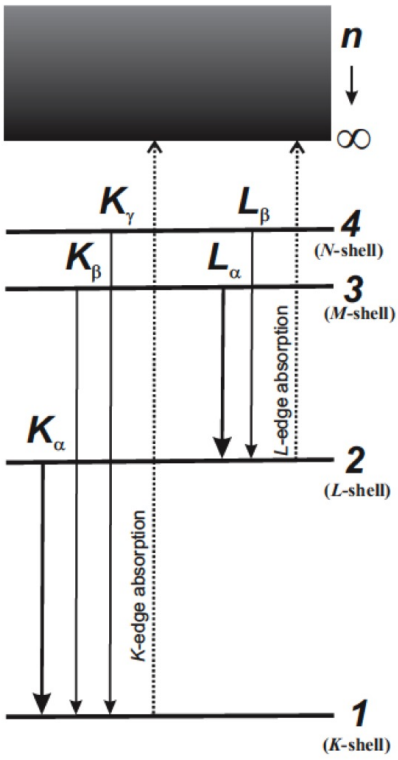


Figure 3.6: X-ray emission lines (solid arrows) originating from the K- and L-shell electron excitation (dashed arrows). The standard nomenclature used for labeling the consecutive emission lines is shown.

large variety of short pulse x-ray sources available for these studies, including table-top sources based on high harmonic generation or laser-induced plasmas and large accelerator based facilities such as x-ray free electron lasers (XFEL), third generation synchrotron sources such as Elettra, provide a unique combination of x-ray properties that are particularly well suited for time-resolved measurements. These include tunability over a large x-ray energy range, stability, defined polarization, high flux and high pulse repetition rate.
The time resolution needed depends on the process studied. Time programmed and catalytic reactions can use milliseconds to minutes as time-scale, while optical excitations need nanoseconds to femtoseconds time resolution. In order to explore the latter categories of physical processes, free electron lasers and synchrotron slicing sources are suitable for time-resolved experiments. Two key parameters drive the time resolution to obtain a correct signal-to-noise ratio: the number of x-ray photons (exposure time) and the time resolution of the detector (limited for example by the readout time).
The feasibility of time resolved XAS depends on the number of available x-ray photons per data points. These depends on the x-ray pulse intensity and on the repetition rate of the measurement, which is typically in the 1kHz range, when using femtosecond amplified lasers. On the other hand, synchrotrons op-

erate at much higher repetition rate of usually 100-500 MHz, which means that after synchronization of both sources the available x-ray photon flux is reduced by more than 5 orders of magnitude. Therefore, these experiments require a very sensitive detection scheme and a carefully designed sample (accounting for the optical and x-ray cross sections, the available laser pulse energy and the concentration and thickness of the sample).
The time resolved XAS technique is based on the laser-pump x-ray-probe scheme. A laser (pump) pulse excites the system, whose excitation evolution is recorded by an x-ray (probe) pulse at a fixed time delay Δt with respect to the pump pulse. A sketch of this scheme is given in Fig.3.7. The differential

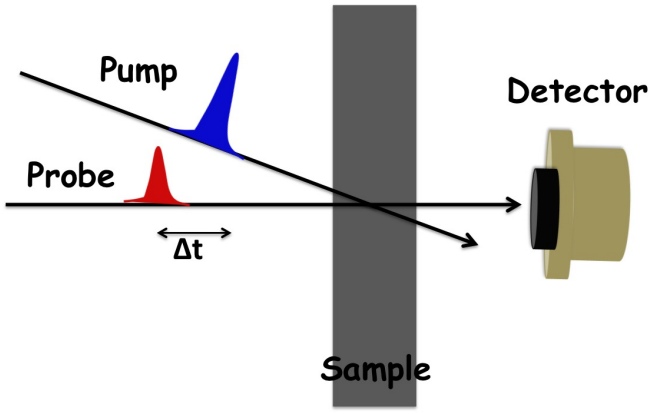


Figure 3.7: Sketch of the pump-probe scheme.

quantity extrapolated by a pump-probe measurement at a generic time t is:

$$\Delta XAS(t) = XAS_{pumped}(E,t) - XAS_{no-pumped}(E,t_0), \tag{3.14}$$

where $XAS_{pumped}(E,t)$ is the absorption signal measured at a generic time t after that the laser-pump pulse has photoexcited the system and $XAS_{no-pumped}$ is the absorption signal taken at a time t_0 before the laser pulse. In order to have the sequence at several time delays of the differential XAS signal, a set of equations is solved:

$$\begin{aligned} \Delta XAS(t_1) &= XAS_{pumped}(E,t_1) - XAS_{no-pumped}(E,t_0) \\ \Delta XAS(t_2) &= XAS_{pumped}(E,t_2) - XAS_{no-pumped}(E,t_0) \\ \Delta XAS(t_n) &= XAS_{pumped}(E,t_n) - XAS_{no-pumped}(E,t_0). \end{aligned} \tag{3.15}$$

3.4 Time-resolved XAS apparatus at BACH beamline and T-ReX lab

3.4.1 The BACH beamline

The BACH (Beamline for Advanced diCHroism) beamline is operating at the Elettra synchrotron radiation facility [70, 71]. A schematic drawing of a modern synchrotron storage ring is depicted in Fig.3.8. The electrons are produced

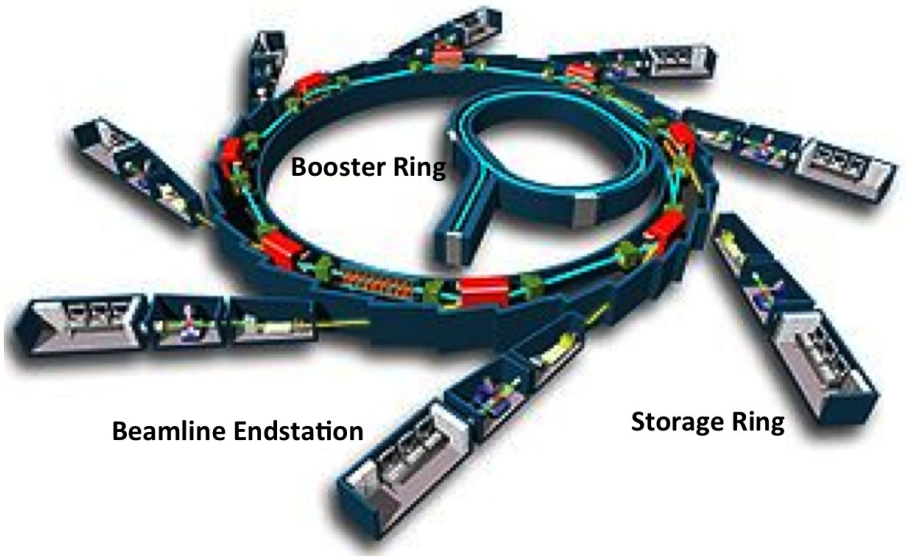


Figure 3.8: Generic scheme of a modern synchrotron storage ring. The key elements of the machine are shown, including the booster and storage rings and the experimental beamline endstations.

in the electron gun, which injects them into a linear accelerator (the so called linac), which is located inside of the actual storage ring. The pre-accelerated electrons enter a booster ring, which is circular in shape with a small linear acceleration section, capable of increasing the electron energy up to the final value. Finally, the GeV electron beam is injected into the storage ring, where it can circulate for many hours, generating the desired SR, which in turn is used at several beamline endstations simultaneously.

The Elettra storage ring, in its standard operating mode, delivers x-ray pulses with low intensity (e.g. $10^2 - 10^3$ photons/pulse in a monochromatic beam at ID8.1) and a high repetition rate. Typically, the filling mode is multi-bunch: 432 electron bunches with ∼60 ps full-width-half-maximum (FWHM)

rotating in the storage ring with ∼2ns inter-bunch period and a resulting 1.157 MHz revolution frequency. A dark gap is present, consisting of about 30 electron bunches with a very reduced amplitude. The main timing parameters of the Elettra synchrotron are reported in table 3.1.

Table 3.1: Timing parameters of the Elettra storage ring

Parameter	Value
Accelerating Frequency (RF)	499.65 MHz
Number of electron bunches	432
Revolution Frequency	1.157 MHz
Typical bunch width	$\sim$ 60 ps

The beamline was designed and built to give high flux ($\sim 10^{12}$ photons/s) and high brillance in a wide photon energy range (46-1600 eV) with control over light polarization (linear horizontal, linear vertical, circular clockwise and counterclockwise). The top view scheme of the beamline is visible in Fig.3.9.

The beamline consists of four sections: the pre-focusing section, the monochromator, the refocusing section and the experimental endstations.

Radiation source

The radiation source of BACH is a double APPLE-II undulator put in series in the right section number 8.2 of the Elettra storage ring. They are capable of providing full tunability of the polarization of the light from linear to circular on the axis of the electron orbit. The undulator for low energies (LE) has a period of 77.36 mm for 27 periods. The photon energy ranges from 22 to 300 eV using the first harmonic. The high energies undulator (HE), made by 44 periods of 48.36 mm length, produces radiation with energy between 185 and 700 eV in the first harmonic while higher energies are covered by higher harmonics. Such characteristics make the flux to be optimized in two different energy ranges: 50-150 eV for the LE undulator, and 600-1000 eV for the HE undulator.

Beamline optics and monochromator

The pre-focusing section includes a Kirkpatrick-Baez system of focusing with two spherical mirrors SM1 and SM2, which deflect the beam horizontally and vertically respectively. Both of these optical elements focus the radiation onto the entrance slit of the monochromator.

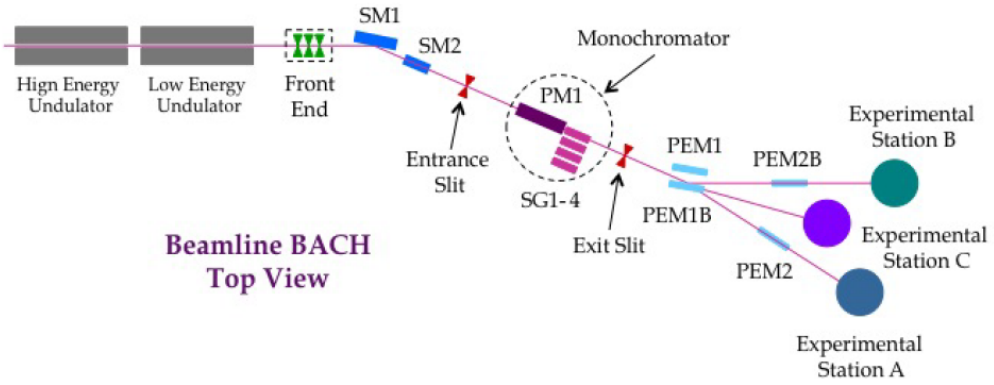


Figure 3.9: Top view scheme of the beamline BACH. SM1 and SM2 are the horizontal and vertical pre-focusing mirrors. PM1 is the plane mirror of the monochromator, while SG1-4 is the set of four interchangeable gratings. PEM1 and PEM1B are the horizontal and vertical postfocusing mirrors and are used alternatively to direct the photon beam in the experimental chambers A, B or C. PEM2 and PEM2B are the vertical post-focusing mirrors of branch A and B, respectively.

The monochromator scheme follows the Padmore variable angle spherical grating monochromator design. The incoming photon beam, focused onto the entrance slit in both directions (tangential and sagittal), impinges on the plane mirror PM1 and then is diffracted and focused tangentially by the spherical grating(s) SG1(-4) onto the exit slit. In order to change the photon energy PM1 and SG1-4 must be rotated simultaneously. This assures the tangential monochromatic focus onto the exit slit to be kept fixed. SG1-3 spherical gratings cover 35-200 eV, 200-500 eV and 500-1600 eV ranges with estimated resolving powers of 20000-6000, 20000-6000, and 15000-5000, respectively. The fourth grating SG4 provides a monochromatic beam in the 400-1600 eV range with resolving power smaller (10000-2000) with respect to SG1-3 but allowing a major flux. The first element of the refocusing section is a plane elliptical mirror PEM1 (PEM1B for branch B), which focuses the beam horizontally in the experimental chamber. The vertical refocusing is provided by a second plane elliptical mirror PEM2 (PEM2B for branch B). The mirrors are interchangeable in vacuum in order to deflect the beam in branch A, B and C. Spot dimensions of the beam in correspondence of the sample position are 250x20

μm^2 for branch A, 250x30 μm^2 for branch B and 10x10 μm^2 for branch C.

Experimental end-stations

The end-station A is constituted by a preparation chamber and a main experimental chamber. The first is equipped by a manipulator for sample annealing and some evaporators. The main experimental chamber is equipped, in order to perform a multi-spectroscopy investigation with PES (including ARPES), XAS, and x-ray magnetic circular dichroism (XMCD), with an hemispherical electron analyzer, a four-degrees-of-freedom manipulator with the possibility to measure the drain current from the samples. The chamber allows, also, to carry out normal XES and RXES measurements by means of a ComIXS fluorescence spectrometer [72] (see Fig. 3.10).

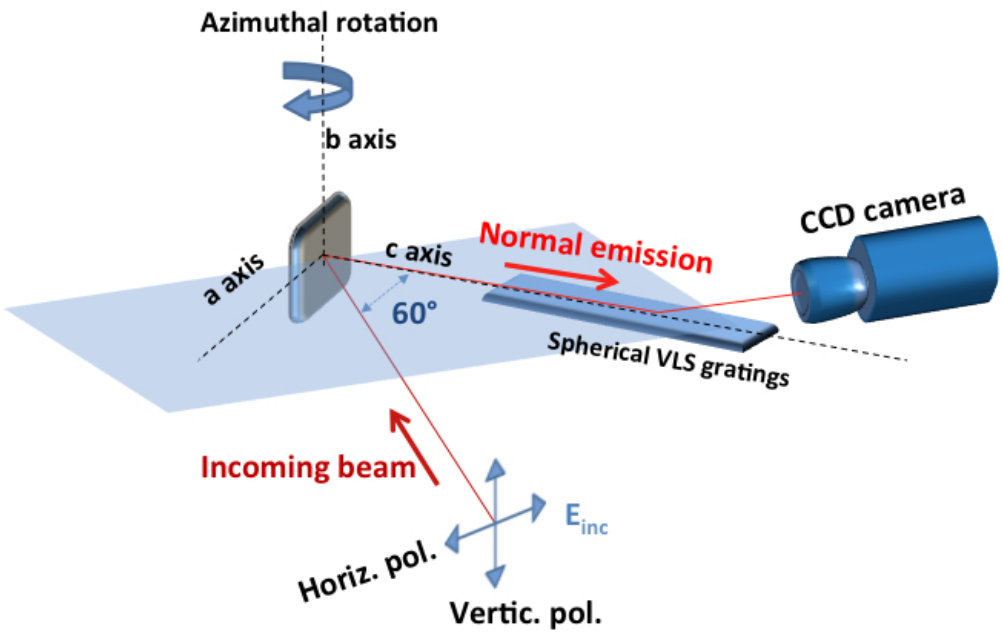


Figure 3.10: Experimental geometry of the end-station A of beamline BACH [73].

The spectrometer is equipped with two variable-line-spacing spherical gratings and a charge-coupled device (CCD) with 20x20μm^2 pixel. It is located in the horizontal plane with a take-off angle of 60° with respect to the incident beam direction. The electric filed E_{inc} of the incident beam could be set either horizontal or vertical, with respect to the experimental geometry.

The end-station B, equipped with a new Ultra High Vacuum UHV cryomagnet, hosts a setup dedicated to (XMCD) in high magnetic fields (±6.5 Tesla) and variable temperature from 1.4 K to 340 K on the sample in base

pressure of 4x10^{-11} mbar.

The end-station C hosts the time-resolved XAS setup, which will be described below.

3.4.2 Laser system at T-ReX lab

The scheme of the set-up for the generation of the laser pulses is shown in Fig.3.11. A description of the pulse generation process is given here and

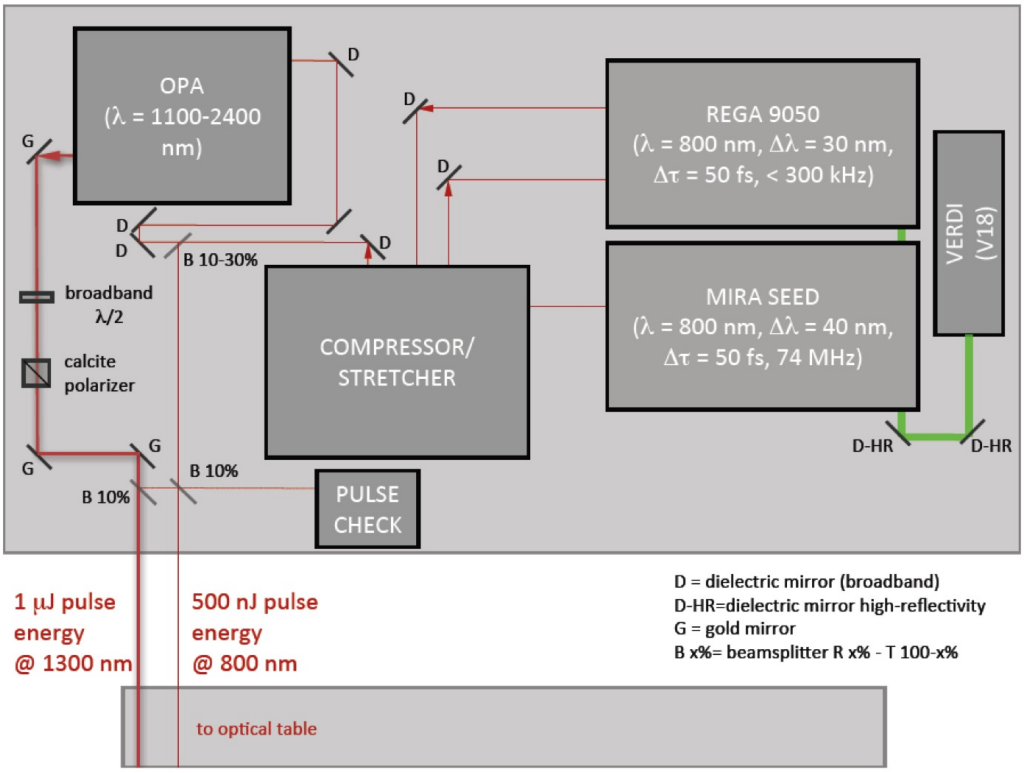


Figure 3.11: Set-up for generation of tunable IR pulses. See text for the description of the generation process [74].

more details can be found elsewhere [75, 76]. A solid-state diode-pumped Nd:vanadate (Nd:YVO4) laser (Coherent Verdi V18) generates continuous light at a wavelength of 532 nm and power of 18 W. This laser constitutes the pump for both an optical Ti:sapphire oscillator (Coherent Mira Seed), using about 8 W of the Verdi power, and a Regenerative Amplifier (Coherent RegA Model 9050), using the remaining 10 W. The 40 nm broad and 50 fs short laser pulse produced by Mira Seed is temporally broadened up to 30 ps by the Stretcher in order to minimize peak intensity before amplification and thus increase the efficiency of the process. The seed pulse enters the RegA system and it is amplified in a Ti:Al2O3 crystal by coupling with the 532 nm pump laser. After several trips in the cavity, the amplified pulse is switched out by a RF-controlled SiO2

Bragg-cell (Cavity Dumper). The 800 nm amplified pulse is then compressed down to of 50 fs by the Compressor. The repetition rate of the RegA system is tunable, with $f_{rep.rate} < 300$ kHz. The maximum energy per pulse is reached at 100 kHz and it is about 5 μJ.

3.4.3 Time resolved XAS setup

The time-resolved XAS setup is a novel experimental apparatus for performing time-resolved soft x-ray absorption spectroscopy in the sub-ns non-hybrid multi-bunch mode synchrotron radiation [77]. As sketched in Fig.3.12, conventional laser-pump x-ray-probe experiments require the storage ring operating with dedicated filling modes (e.g. single bunch, few-bunches and hybrid modes)[38, 40, 78–96]. To overcome this limitation and to operate at variable repetition rates, the use of the multi-bunch filling pattern must be implemented with novel and effective acquisition concepts and ideas to perform time-resolved experiments in the sub-ns time domain [97].

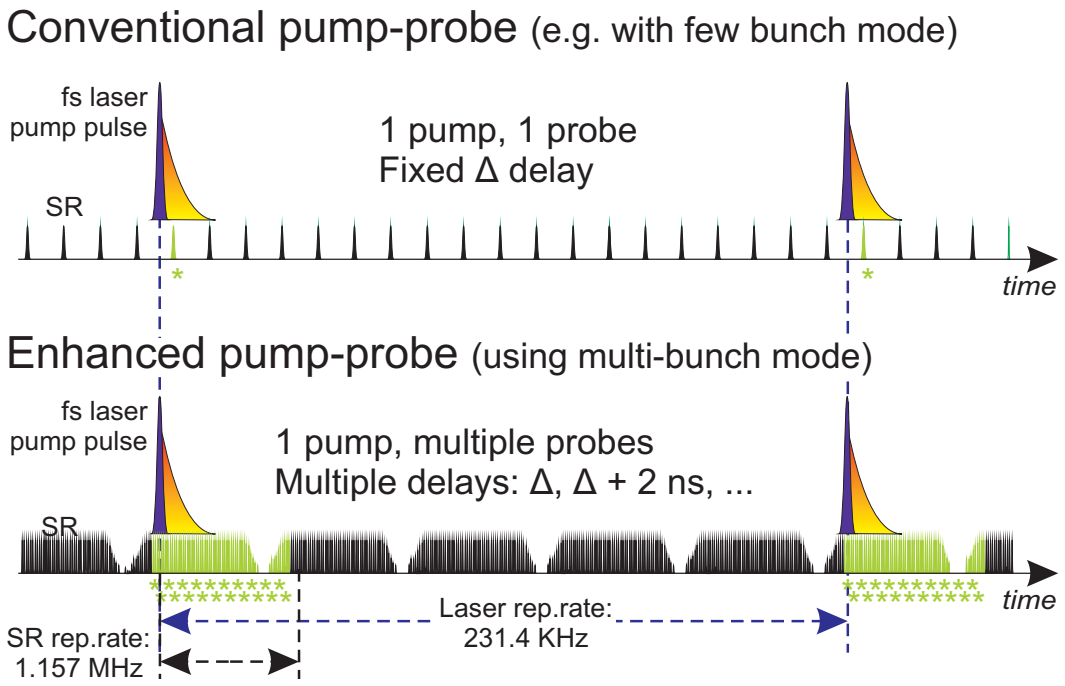


Figure 3.12: Comparison between conventional pump-probe and the present enhanced pump-probe scheme, which exploits the high repetition rate of the multi-bunch filling mode of the synchrotron source. In the conventional pump-probe experiment (top), a single x-ray pulse cyclically probes the transient state at the laser repetition rate (∼250 kHz) and at fixed delay time relative to the laser pulse. In the enhanced pump multiple-probe scheme (bottom), a train of consecutive x-ray pulses at ∼ 500 MHz repetition rate and synchronized with the laser pulse, probes the transient state at multiple delays (Δns, $\Delta + 2ns$, ...) for its entire lifetime [77].

In a conventional laser-pump x-ray-probe experiment, as already outlined in the previous section, a laser pulse excites a transient state while a x-ray pulse,

at a fixed delay time Δt relative to the laser pulse, probes the non-equilibrium states. In the present experimental setup a train of consecutive synchrotron x-ray pulses, following in time the laser excitation, probe the relaxation process of the excited states at multiple delay times allowing to observe the complete dynamical evolution at once. The photon counting approach, adopted to measure the x-ray fluorescence emission fully exploits the available x-ray photon flux at ∼500 MHz repetition rate as a stroboscopic probing sequence in order to provide continuous snapshots of the transient state spectra. In figure 3.13 a scheme of the acquisition flow is shown.

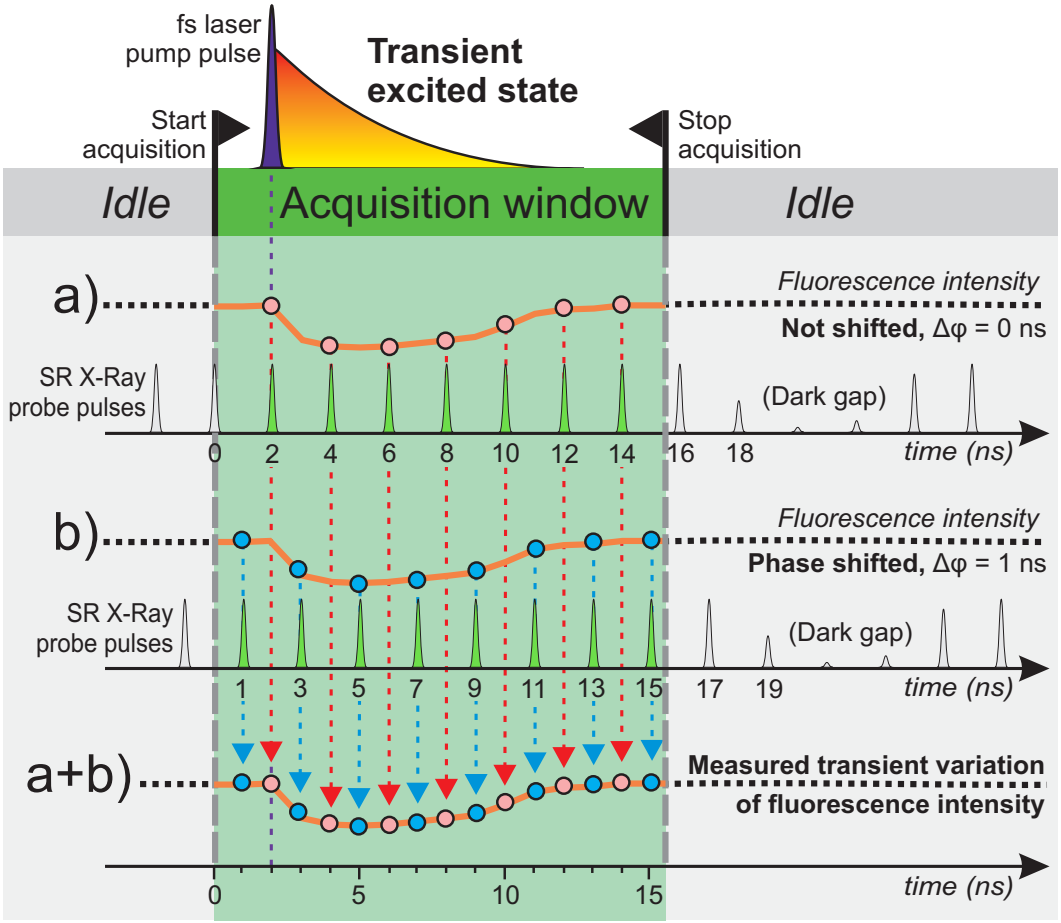


Figure 3.13: (a) The transient state is sampled during a well defined acquisition window(green interval) that is repeated iteratively at the repetition rate of the laser source. The acquisition window selects a number of consecutive x-ray probing pulses. Usually, the photon dark gap is used as a reference to check the acquisition status and to measure the noise signal from the x-ray photon detector. (b) In order to map out the temporal behavior of the transient state with a time sampling step lower than 2 ns, phase shifted acquisitions with different pump-probe time alignment are performed. The photon bunches before the laser pulse arrival (t = 0), probing the XAS spectrum of the non-excited state, are used as a reference [77].

A schematic layout of the present setup is reported in figure 3.14. It is based on a variable repetition rate Ti:sapphire laser (pump pulse) synchro-

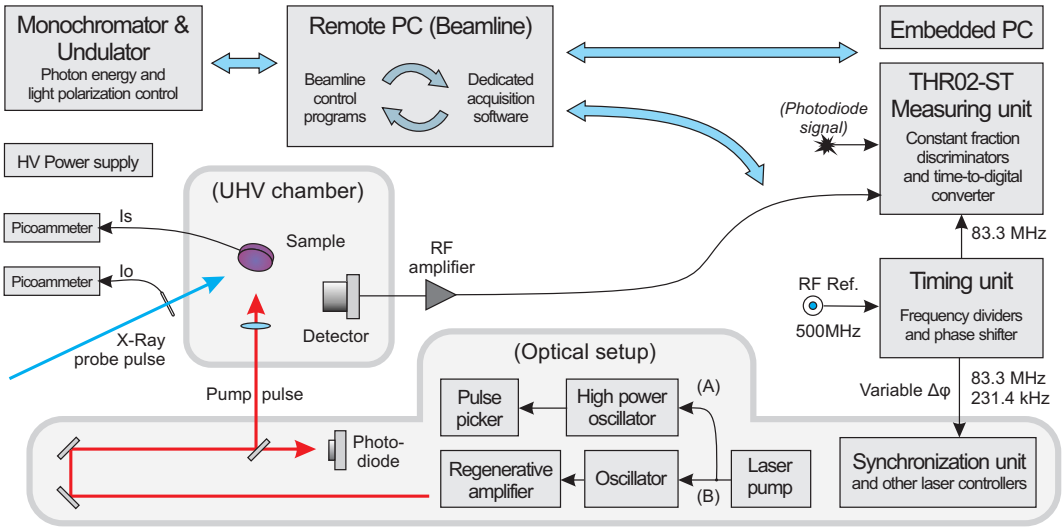


Figure 3.14: Schematic layout of the experimental setup for a pump-probe XAS measurement, with its three main sections: the beamline environment (UHV chamber, picoammeters, power supplies, undulator, monochromator, and remote PC), the optical setup (laser sources and controllers), and the measuring setup (THR02-ST measuring unit, timing unit and embedded PC) [77].

nized with the $\sim$ 500 MHz x-ray synchrotron radiation bunches. The samples are positioned in an ultrahigh vacuum chamber and mounted on a suitable motor-controlled manipulator. The laser beam enters the experimental chamber through a quartz window at an angle of 30 degrees with respect to the x-ray photon beam. The x-ray fluorescence emission is detected by an ultrafast micro-channel plate (MCP) x-ray detector [98] set at 60 degrees off the incoming x-ray photon beam. The MCP (see Fig.3.15) is a detector consisting

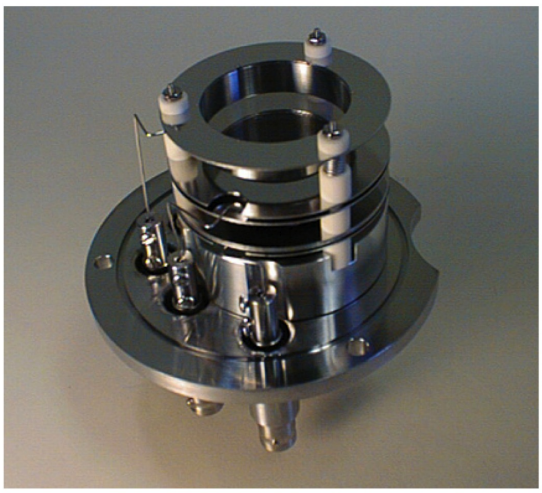


Figure 3.15: Picture of a micro-channel plate (MCP) detector.

of millions of very-thin, conductive glass capillaries (4 to 25 μm in diameter) fused together and sliced into a thin plate. Each capillary or channel works as an independent secondary-electron multiplier to form a two-dimensional secondary-electron multiplier. The MCP shows a high detection efficiency to electrons and ions. It is sensitive to a wide range of radiation including UV, VUV, soft X-ray photons and neutrons. The MCP offers many advantages over conventional detectors: compact, light weight, good timing properties due to short length, high gain, excellent pulse height distribution.
The amplified laser source operates at a variable repetition rate (230 kHz - 83.3 MHz) and delivers $\sim$ 5 μJ to $\sim$ 25 nJ, $\sim$ 100 fs, 800 nm laser pulses (see table 3.2).

Table 3.2: Timing parameters of the Ti:Sa laser source

	RegA9000	Mira HP
Wavelenght	800 nm; SHG: 400 nm	800 nm; SHG: 400 nm
Pulse width	100 fs	100 fs
Pulse energy	5 μJ/pulse	25 nJ/pulse
Repetition rate	200-250 kHz	variable [5-0.01 MHz] 83.3 MHz

The pump (laser)- probe (x-ray) sources synchronization is achieved by exploiting the radio frequency (RF) master clock of Elettra that provides the time structure of the generated radiation. The RF is divided by a timing unit that also allows for the remote control of the relative time delay by phase shifting the oscillator frequency with respect to the master RF. The phase stabilization of the laser source is achieved via a synchronization unit, which locks the laser oscillators to the Elettra master RF with a time jitter <2 ps. Typical acquisition time histograms as a function of photon bunches and photon energy are shown in the main panel of figure 3.16.

The timing unit can be used to perform phase shifted TR-XAS spectra, with 100 ps or even smaller steps, i.e. with a timebase comparable to the overall time resolution, as illustrated in figures 3.17a and 3.17b. Time-resolved XAS can be used as a novel spectroscopy in the time domain for studying transient states of high temperature materials and photoinduced phase transitions produced by intense optical pulses.
As a proof of principle for the present TR-XAS setup, herewith below I report on time-resolved XAS spectra of the laser induced solid-liquid-solid transitions of crystalline Ge [99].

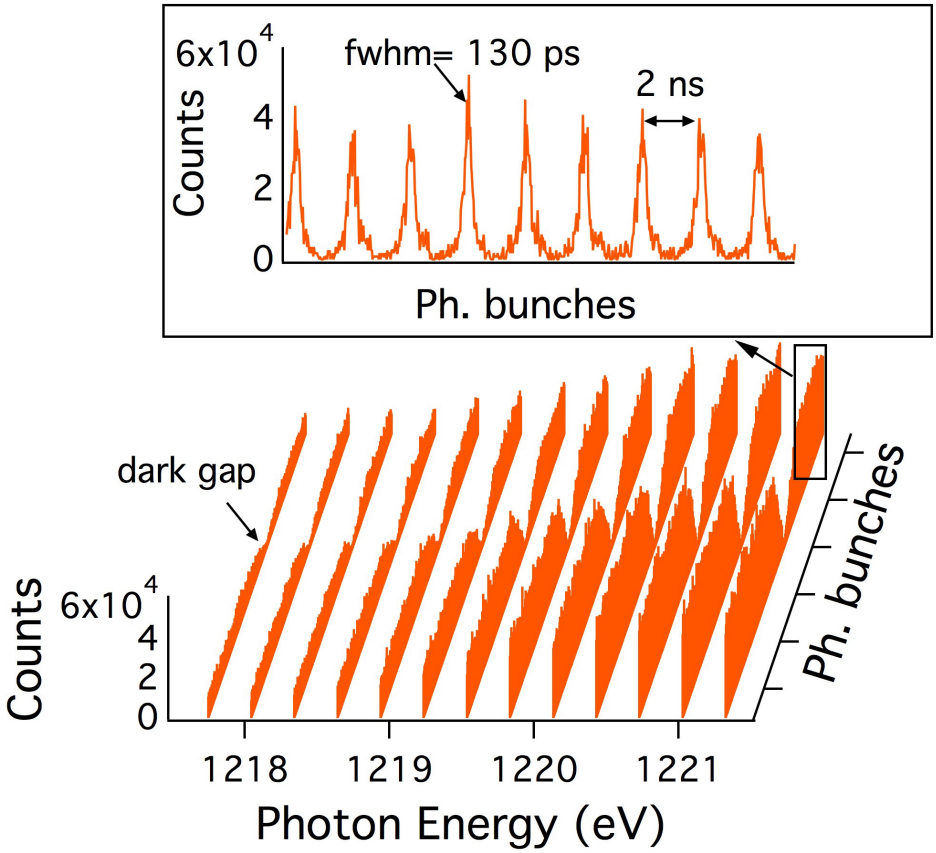


Figure 3.16: Typical acquisition time histograms (counts vs consecutive photon bunches), taken at different x-ray photon energies through an absorption threshold (in this example, the Ge L_3 threshold). The constant time position of the dark gap indicates the overall stability of the synchronization between the probe and pump sources. Inset: pulse height distribution of consecutive x-ray photon bunches recorded at fixed energy and without laser. The x-ray fluorescence signal clearly inherits the time structure of the storage ring filling pattern (2 ns time separation between two consecutive photon pulses), while the standard deviation (FWHM = 130 ps) of each measured pulse is wider than the typical width of electron bunches (60 ps) [77].

3.5 Photoinduced surface semiconductor-metal transition in crystalline germanium

3.5.1 Introduction

Structural investigations on condensed phases of Ge have been of fundamental interest due to the interplay between the covalent and metallic characters of the bonding [100, 101]. Ge manifests a large degree of polymorphism in its solid phases. The stable crystalline phase at ambient pressure is the diamond structure where each Ge atom is surrounded by four covalently bonded first neighbors in a tetrahedral symmetry. This form of Ge is semiconducting with an indirect gap of 0.67 eV. At standard pressure the melting-point temperature

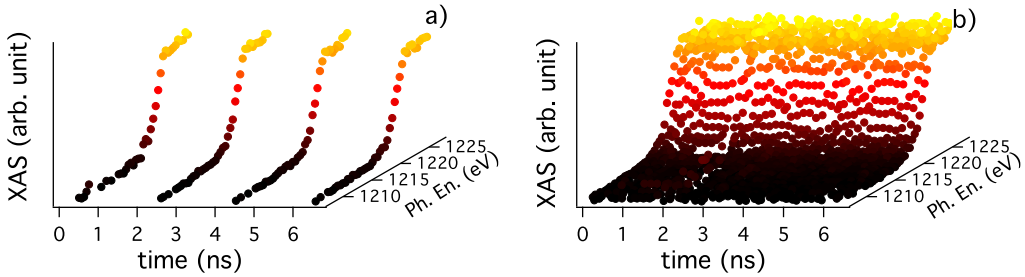


Figure 3.17: Comparison between a standard multi-probe TR-XAS spectra (a) and a denser phase scan spectra (b). Figure 3.17a shows four consecutive Ge L_3 TR-XAS spectra separated by 2 ns inter-bunch delay. The intensity of each XAS point is obtained by integrating a single photon bunch (i.e. histogram peaks, see inset of Fig.3.16) per time and per energy step. Figure 3.17b shows a phase scan, i.e. consecutive XAS spectra obtained in the same operating conditions of figure 3.17a but with incremental 100 ps laser-SR delay shifts [77].

for c-Ge is T_m=1210.4 K, a value that decreases on increasing pressure. At the melting transition the covalent bond is destroyed and a semiconductor-metal transition occurs. The electrical resistivity decreases by a factor of about 11 and, at the same time, the density increases by about 5%, while the average coordination number increases from 4 to about 7, which is however less than 10-12 found in normal liquid metals [102].

This semiconductor is of particular interest for testing the TR-XAS setup for its absorption edges in the liquid phase are shifted of about 0.7 eV towards lower photon energies (cf. Ge K_α [103] reported in Fig.3.18 and $M_{2,3}$ [101, 104] edges), while the liquid-solid phase transition is expected to take place on a time scale of few ns (see Fig.3.19) [105].

3.5.2 Experimental procedure

A bulk of Germanium of sizes 1cm x 1cm has been used. The TR-XAS measurements have been carried out by means of the time-resolved setup described above. The synchrotron storage ring operated in multi-bunch mode with energy $\sim$ 2.4 GeV and current $\sim$ 150 mA. The XAS spectra have been taken at the Ge L_3 edge. The selected grating of the beamline monochromator has been SG4 with entrance and exit slit equal to 50. The acquisition lasts 20 s per energy point and 30 min for completing a suitable time-resolved spectra. The XAS spectra of the Ge have been recorded under pump-probe conditions at several laser fluences between 110 mJ/cm^2 and 150 mJ/cm^2.

3.5.3 Results and discussion

The XAS spectra of the Ge, recorded under pump-probe conditions at a laser fluence below the Ge surface-melting critical fluence, i.e. 110 mJ/cm^2, are shown in figure 3.17 for a fixed pump-to-probe delay time (figure 3.17a) and for

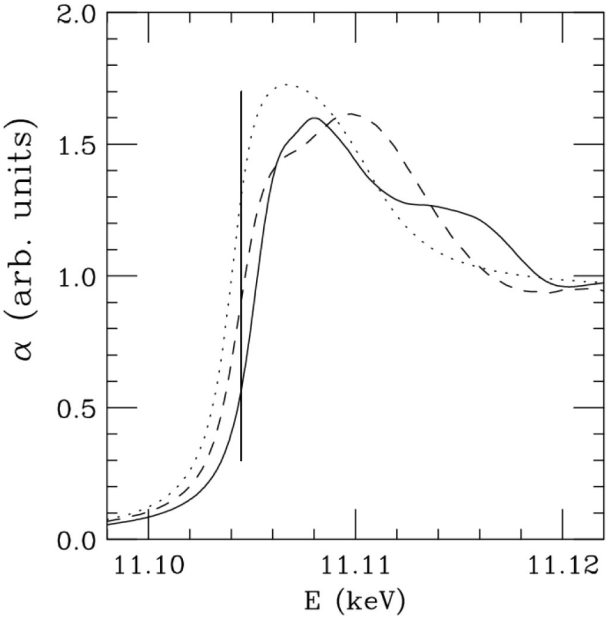


Figure 3.18: High-resolution X-ray absorption K-edges of solid Ge at RT (solid line), liquid Ge at 1250 K (dotted line), and AgGe f.c.c. alloy with 1.5% Ge measured in fluorescence [106] (dashed line) [103].

a varied delay time (figure 3.17b). As expected these spectra exhibit the typical solid Ge L_3 lineshape [107] for each temporal snapshot after the absorption of the laser pulse. In figure 3.20 the complete set of data shows the dynamics of the melting from the Ge L_3 absorption edge for a photon energy range between 1213 eV and 1229 eV and for time delays between 0 ns and 300 ns at different laser fluences. In figure 3.20(a), where the TR-XAS spectra have been acquired with a laser fluence=110 mJ/cm^2, the uniformity of the colors indicate that all the spectra are identical, reflecting the fact that the surface is still a solid. Increasing the laser fluence at 114.7 mJ/cm^2 as in figure 3.20(b), the sample undergoes a solid-liquid phase transition and the spectra present dramatic changes of the lineshape and absorption edge energy position as a function of the pump-probe delay time. In figure 3.20(c),(d),(e) and (f) the laser fluence has been increased until a value of 150 mJ/cm^2, that is the limit above which the sample is damaged. It is evident that the increase of the laser fluence corresponds, as it is expected, to an increase of the time duration of the melted phase of Ge and so the recovery to the solid initial phase is longer. In order to study in more detail the dynamics of this solid-liquid-solid phase transition, the spectra recorded below and above the threshold (110 mJ/cm^2) are plotted together. Figure 3.21a and b reports, respectively, the spectra of a not-melted and melted Ge sample. The spectra reported in 3.21b-d have been obtained using a laser fluence of 120 mJ/cm^2. This set of data shows, in false colors, the dynamics of the melting as measured from the Ge L_3 absorption edge for a photon energy range between 1216 eV and 1224 eV and for pump-probe delay

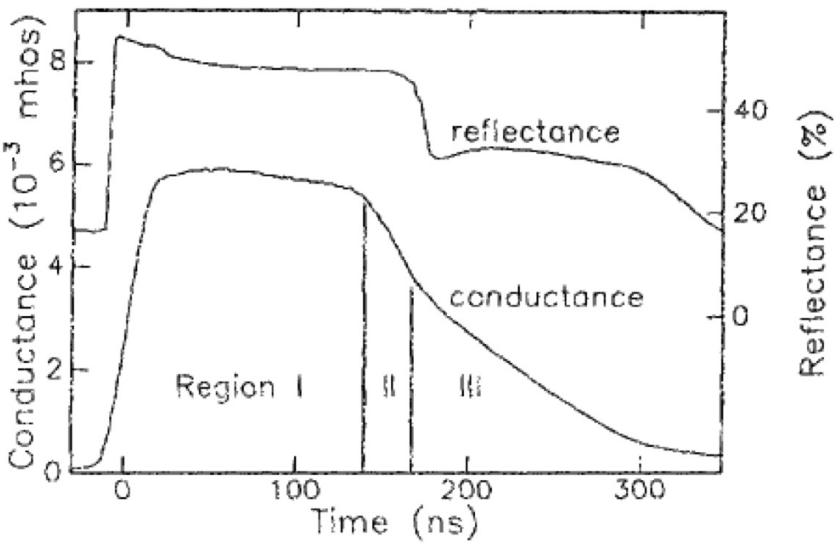


Figure 3.19: Transient conductance and approximate reflectance for a sample irradiated at 0.76 J/cm^2. The Gaussian laser pulse is centered about the temporal origin [105].

times between 0 ns and 300 ns. Figure 3.21d reports the TR-XAS spectra at constant delay times ($t < 0$, $t = 40$ ns and $t = 200$ ns), quite representative of the solid-liquid-solid phase transition dynamics of a Ge crystal. The TR-XAS spectra present dramatic changes of the lineshapes and absorption edge energy position as a function of the pump-probe delay time. The onset of the Ge L_3 absorption edge at a delay time of about 10 ns is shifted by approximately 0.7 ± 0.1 eV with respect to the solid Ge edge, as shown in figure 3.21c. The magnitude of the absorption edge is increased by approximately 30% and the small fine structure at 1229 eV disappears [103]. Indeed, the relative XAS intensity variation reported in figure 3.22 as a function of time can be divided into four regions. In region a, the solid Ge underneath the area illuminated by the laser starts melting and, consequently, the solid-liquid front propagates into the probed volume. In region b, the liquid cools down by conduction into the surrounding solid. The nucleation of the supercooled liquid is in part c, while in region d the solidification process occurs at constant rate. Notably, the laser induced solid-liquid-solid dynamic melting of Ge, as resulting from the present experiment, is fully consistent with that obtained by Stiffler et al. [105] using time-resolved conductivity measurements, reported in Fig.3.19.

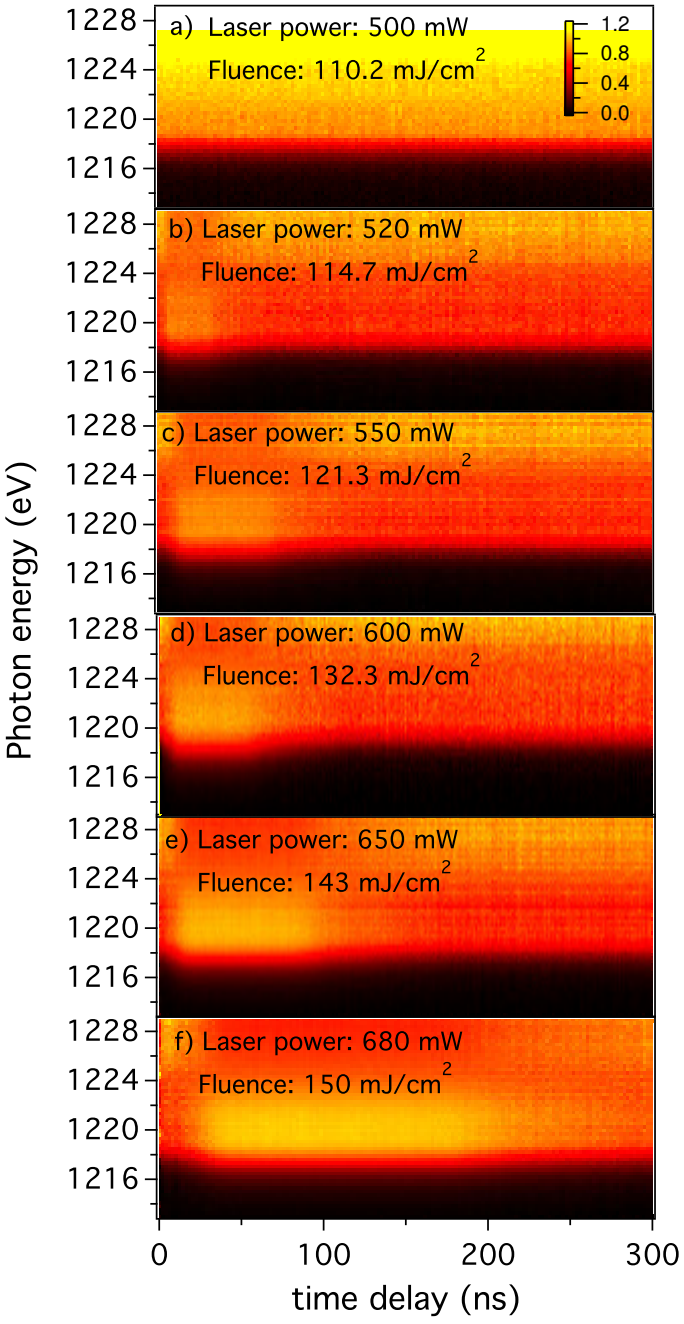


Figure 3.20: Intensity plots of L_3 TR-XAS spectra plotted versus the time delay (ns) and versus the x-ray photon energy (eV) at different laser powers: a) laser power equal to 500 mW which corresponds to a fluence on the sample of 110.2 mJ/cm^2; b) laser power equal to 520 mW which corresponds to a fluence on the sample of 114.7 mJ/cm^2; c) laser power equal to 550 mW which corresponds to a fluence on the sample of 121.3 mJ/cm^2; d) laser power equal to 600 mW which corresponds to a fluence on the sample of 132.3 mJ/cm^2; e) laser power equal to 650 mW which corresponds to a fluence on the sample of 143 mJ/cm^2; f) laser power equal to 680 mW which corresponds to a fluence on the sample of 150 mJ/cm^2.

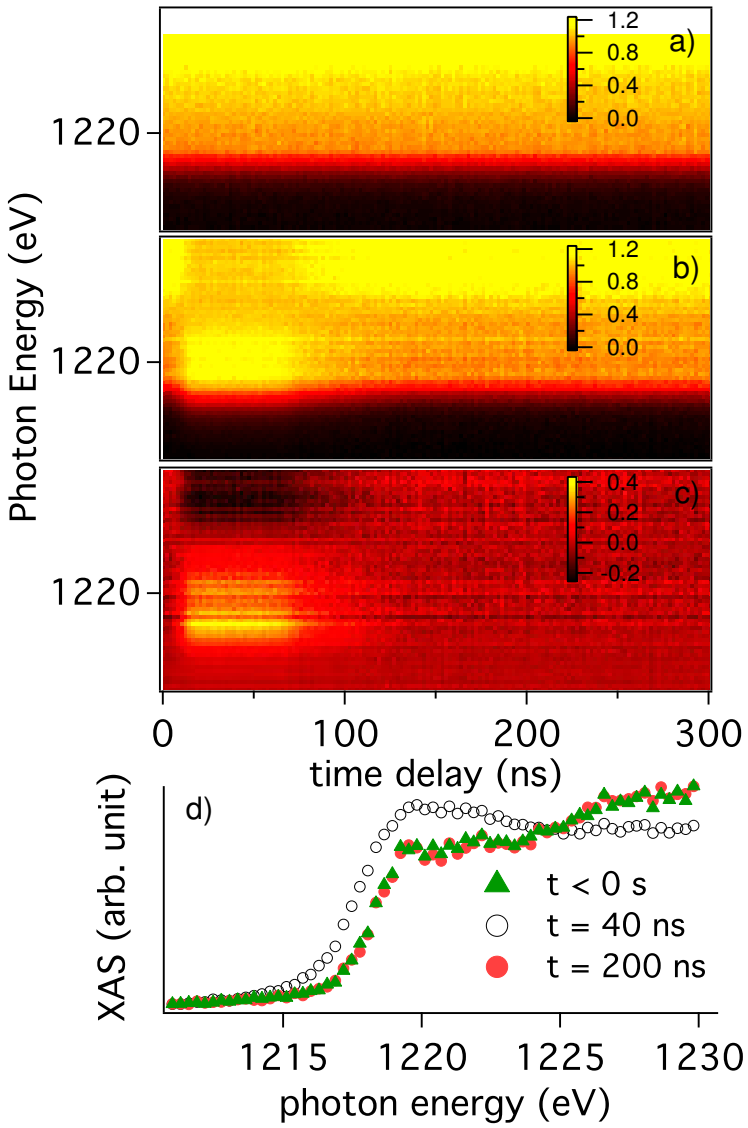


Figure 3.21: Intensity plots of L_3 TR-XAS spectra of a not-melted (a) and melted (b) Ge sample. The XAS spectra intensities are plotted versus the photon bunch arrival time (the laser pulse: t=0) and versus the x-ray photon energy. Figure 3.21c: difference map obtained as the difference between the TR-XAS spectra in figure 3.21b and a ground state XAS spectrum measured at $t < 0$. Figure 3.21d: Ge L_3 TR-XAS lineshapes sliced from the intensity plot in (b) and taken at different time delays with respect to the laser pulse [77].

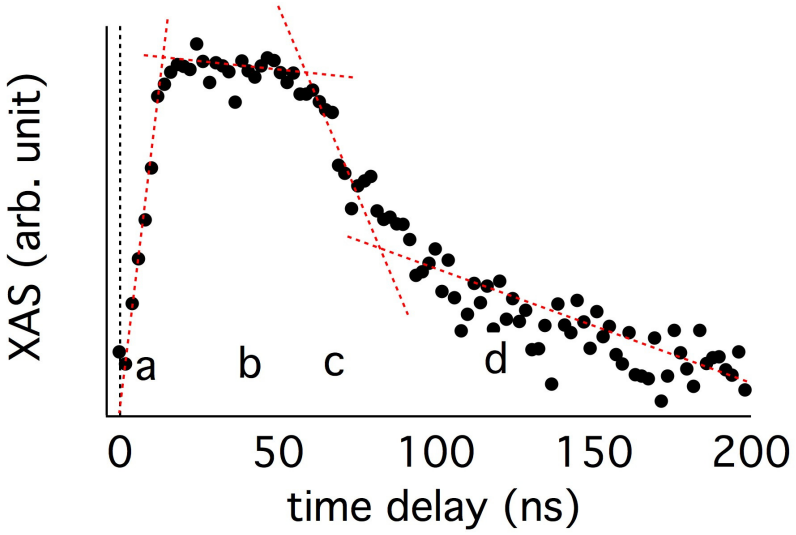


Figure 3.22: This figure shows a slice at constant photon energy (1219.0 eV) of the intensity plot shown in figure 3.21b. This TR-XAS relative intensity variation as a function of time can be divided into four regions (a, b, c and d) according to its slope (see text) [77].

Chapter 4

Theory and Modeling

This chapter is dedicated to the Density Functional Theory (DFT) and Local Density Approximation plus U (LDA+U) theories and to the details of the modeling of the single layered hd-PCMO system.

4.1 Introduction

A universal approach to calculate the electronic properties of solids is the density functional theory (DFT). The quantum mechanical many-body problem is solved transforming the system of interacting electrons into a non-interacting system with the same total density. The electron density ρ uniquely defines the total density of the system E_{TOT} and is a functional E_{TOT} (ρ) of the density:

$$E_{TOT}(\rho) = T_S(\rho) + E_{ee}(\rho) + E_{Ne}(\rho) + E_{xc}(\rho) + E_{NN} \tag{4.1}$$

where $T_S(\rho)$ is the kinetic energy (of the non-interacting particles), $E_{ee}(\rho)$ is the electron-electron repulsion, $E_{Ne}(\rho)$ is the nuclear-electron attraction, $E_{xc}(\rho)$ are the exchange-correlation energies and the last term E_{NN} corresponds to the repulsive Coulomb energy of the fixed nuclei. E_{TOT} is minimized by means of the variational principle, introducing the orbitals χ_{ik}:

$$\rho(r) = \sum_{i,k} \rho_{ik} |\chi_{ik}(r)|^2 \tag{4.2}$$

From the variation of E_c a set of effective one-particle Shroedinger equations, called the Kohn-Sham (K-S) equations, is obtained:

$$(-\nabla^2 + V_{Ne} + V_{ee} + V_{xc})\chi_{ik}(r) = \epsilon_{ik}\chi_{ik}(r) \tag{4.3}$$

In order to solve the K-S equations it is necessary to go through an iterative process till self-consistency is reached. It is necessary to make approximations of the exact functional form of the exchange potential, which is not known. Regarding the choice of the potential I will go through the details in the next

section. A very high accuracy is necessary also in the choice of the basis set. The most accurate scheme used to solve the K-S equations is the full-potential linearized-augmented-plane-wave (FP-LAPW) method, on which the WIEN2k code is based. In order to construct the basis set, the muffin-tin approximation (MTA) is applied. As sketched in figure 4.1, the space of the unit cell is divided into two regions:
i) around each atom a sphere called muffin-tin sphere is constructed and the basis set used is a linear combination of radial functions times spherical harmonics $Y_{lm}(r)$:

$$\Phi_{k_n} = \sum_{lm} [A_{lm,k_n} u_l(r, E_l) + B_{lm,k_n} \dot{u}_l(r, E_l)] Y_{l,m}(\hat{r}) \tag{4.4}$$

where $u_l(r, E_l)$ is the solution of the Schroedinger equation for energy E_l (chosen usually at the center of the corresponding band with l-like character) and the spherical part of the potential inside sphere t; $\dot{u}_l(r, E_l)$ is the energy derivative of u_l evaluated at the same energy E_l. A linear combination of these two functions constitute the linearization of the radial function; the coefficients A_{lm} and B_{lm} are functions of k_n determined by requiring that this basis function matches (in value and slope) each plane wave (PW) the corresponding basis function of the interstitial region; u_l and $\dot{u}_l$ are obtained by numerical integration of the radial Schroedinger equation on a radial mesh inside the sphere.
ii) the interstitial region between the spheres, where the electrons can be considered as "free", is described by a set of plane waves:

$$\Phi_{k_n} = (1/\sqrt{\omega}) e^{ik_n \cdot r} \tag{4.5}$$

where $k_n = k + K_n$ [1]. Each plane wave is augmented by an atomic-like function in every atomic sphere.

The muffin tin radius is a crucial parameter and it should be set as large as possible to save computer time but overlapping spheres must not occur. The solutions to the K-S equations are expanded in this combined basis set of LAPWs according to the linear variation method

$$\Psi_k = \sum_n c_n \Phi_{k_n}, \tag{4.6}$$

where the coefficients c_n are determined by means of the Rayleigh-Ritz variational principle. An important parameter that controls the convergence of the basis set is the cutoff parameter $R_{mt}K_{max}$=5-9, where R_{mt} is the smallest atomic sphere radius in the unit cell and K_{max} is the magnitude of the largest K_n vector. In order to improve upon the linearization and to allow a consistent treatment of semicore and valence states, additional (k_n independent) basis functions, called local orbitals (LO) can be added. They consist of a

[1] K_n are the reciprocal lattice vectors and k is the wave vector inside the first Brillouin zone.

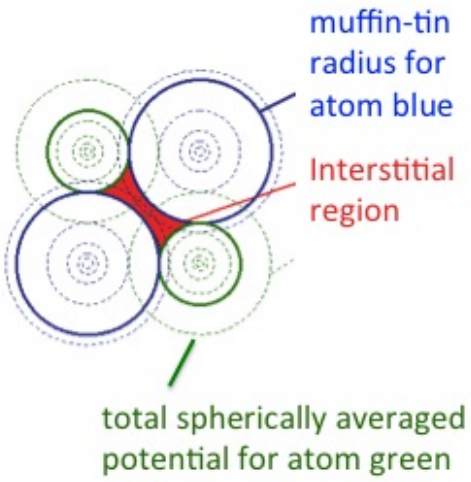


Figure 4.1: Sketch of the muffin-tin approximation (MTA).

linear combination of 2 radial functions at 2 different energies and one energy derivative (at one of these energies):

$$\phi_{lm}^{LO} = [A_{lm}u_l(r, E_{1,l}) + B_{lm}\dot{u}_l(r, E_{1,l}) + C_{lm}u_l(r, E_{2,l})]Y_{l,m}(\hat{r}). \tag{4.7}$$

The coefficients A_{lm}, B_{lm} and C_{lm} are determined by the requirements that ϕ^{LO} should be normalized with zero value and slope at the sphere boundary. In order to make the standard LAPW method more efficient, the energy dependence is covered by using a k_n-independent local orbital. Thus in this new method, called the APW+lo method, a local orbital *lo* is added to have enough variational flexibility in the radial basis functions:

$$\Phi_{k_n} = \sum_{lm}[A_{lm,k_n}u_l(r, E_l)]Y_{l,m}(\hat{r}) \tag{4.8}$$

$$\phi_{lm}^{lo} = [A_{lm}u_l(r, E_{1,l}) + B_{lm}\dot{u}_l(r, E_{1,l})]Y_{l,m}(\hat{r}) \tag{4.9}$$

where the coefficients A_{lm} and B_{lm} do not depend on k_n and they are determined by the requirement that the *lo* is zero at the sphere boundary and normalized. In its general form the LAPW (APW+lo) method expands the potential in the following form:

$$V(\hat{r}) = \begin{cases} \sum_{LM} V_{LM}(\hat{r})Y_{l,m}(\hat{r}) & \text{inside sphere} \\ \sum_K V_K \exp iK \cdot r & \text{outside sphere} \end{cases}$$

and the charge densities analogously.

4.2 LDA and LDA +U

In the previous section I mentioned the importance of the choice of the exchange-correlation potential. A widely used approximation is the Local Density Approximation (LDA), that postulates the following form for the exchange-correlation

functional:

$$E_{xc} = \int \rho(r)\epsilon_{xc}(\rho(r))dr \tag{4.10}$$

The exchange-correlation energy due to a particular density ρ(r) could be found by dividing the material in infinitesimally small volumes with a constant density. Each such volume contributes to the total exchange correlation energy by an amount equal to the exchange correlation energy of an identical volume filled with a homogeneous electron gas, that has the same overall density as the original material has in this volume, see Fig.4.2.

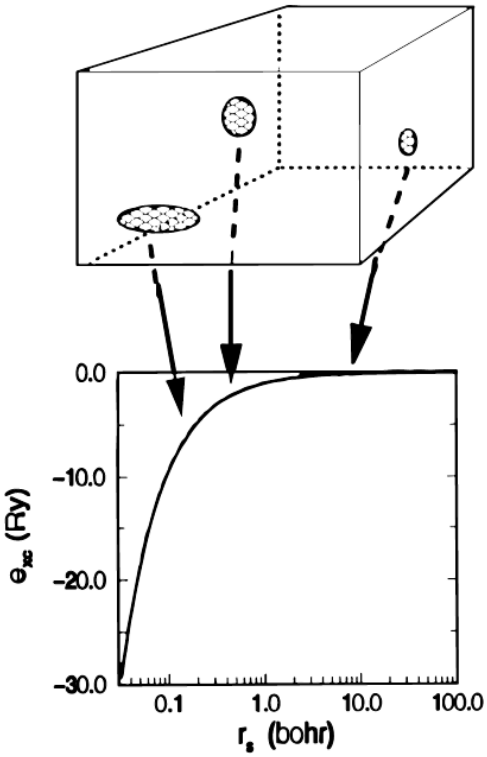


Figure 4.2: Illustration of the idea behind the LDA postulate. Every infinitesimally small volume of the material contributes to the exchange-correlation energy with an amount equal to the contribution of a homogenous electron gas that occupies the same infinitesimally small volume, and that has the same (overall) charge density as the charge density of the original material in that volume. The horizontal axis is proportional to the density of the homogeneous electron gas. The vertical axis displays the exchange-correlation energy of the homogeneous electron gas [108].

The LDA method is not accurate enough for a proper description of TMOs with partially filled $3d$-orbitals. The most pronounced failure is that LDA predicts these systems to be metals whereas experimentally they are insulators. The root of the problem is the unscreened on-site Coulomb interaction, as it is described by the Hubbard model (see Chapter 2). In a single-band system on the mean-field level if Hubbard repulsion U is larger than the bandwidth W, it splits the band into two Hubbard sub-bands with a gap $\propto$ U. The spectral

weight of a quasiparticle is redistributed between these sub-bands. At a half-filling, the Fermi level is inside the gap and the system is an insulator. Thus it is necessary to implement the LDA method adding the 'extra' term U, which includes or simulates the effects of on-site interactions [109].

4.3 WIEN2k: a tool for ab-initio electronic structure calculations and XAS spectra simulation

WIEN2k is a full-potential LAPW-code for crystalline solids. It is written in FORTRAN 90 and requires a UNIX operating system since the programs are linked together via C-shell scripts. The code has been implemented with a graphical web user interface, called w2web, in which an automatic choice of default options is present in order, for example, to initialize a calculation or to run a self-consistency cycle (SCF). There are several utility programs, like band structure, electron density, density of states, etc. The flow and usage of different programs is sketched in the following diagram (Fig.4.3):

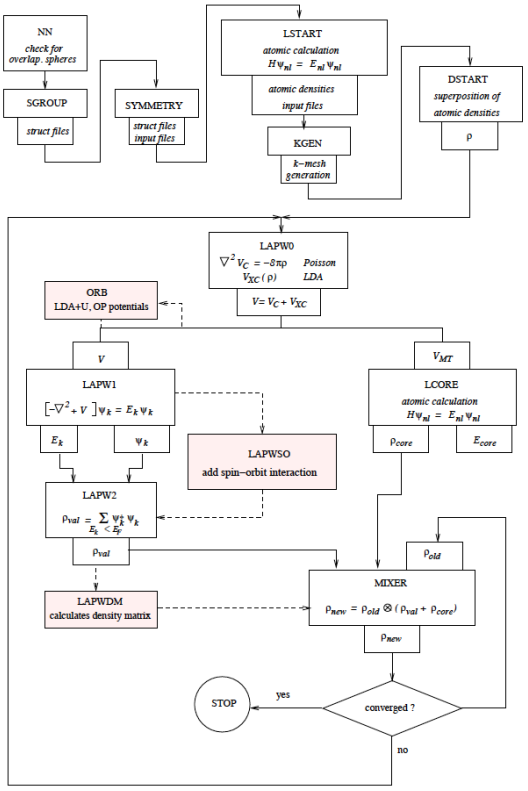


Figure 4.3: Flow chart of programs in WIEN2k [110].

The part of the initialization consists of the following programs:

- NN checks the nearest neighbor distances up to a specified limit and it helps to determine the atomic sphere radii R_{MT};
- SGROUP determines the space group of the structure defined in the input file;
- SYMMETRY generates the space group symmetry operations and the LM expansion for the lattice harmonics, and determines the point group of the individual atomic sites and the local rotation matrices.
- LSTART generates free atomic densities and determines how to treat the different orbitals in the band structure calculations.
- KGEN generates a k-mesh in the irreducible part of the BZ;
- DSTART, starting from the atomic densities created in LSTART, generates an initial density for the SCF cycle.

Then, the SCF consists of the following steps:

- LAPW0 create the potential from the density
- LAPW1 calculates valence bands (eigenvalues and eigenvectors)
- LAPW2, starting from the eigenvectors computed in LAPW1, calculates valence densities;
- LCORE calculates core states and densities;
- MIXER mixes input and output densities.

Once the SCF cycle has converged, one can calculate various properties like Density of State (DOS), band structure, Optical properties or X-ray spectra.

4.3.1 Calculation of the Density of States

The program used for calculating total and partial density of states (DOS) by means of the modified tetrahedron method[2] is called TETRA. It uses the partial charges generated by LAPW2 and generates the DOS in states/Ry and in states/eV (with respect to the Fermi energy). In the partial (lm-like) DOS the multiplicity is not considered and one obtains the total-atomic DOS as a sum over all partial DOS times the multiplicity. The m-decomposed DOS (e.g. p_x, p_y, p_z) is given with respect to the local coordinate system for each

[2]According to the tetrahedron method, which is equally applicable to insulators and metals, the irreducible part of the first Brillouin zone is divided into tetrahedra, within which matrix elements and band energies are linearized in $\vec{k}$. The improvements applied to this method by Bloch et al. allows an efficient use of this method also in plane-wave-based electronic structure methods [111].

atom as defined by the local rotation matrix[3]. In order to use a specified coordinate system (as in our case), it is necessary to modify properly the input file (file.inq) for switching QTL program, which creates the input for calculating total and projected density of states of selected atoms and selected l-subshells in a rotated coordinate system.

4.3.2 Calculation of the X-ray Spectra

The XSPEC program calculates near edge structure of x-ray absorption or emission spectra according to the formalism described by Neckel et al. [112] and Schwarz et al. [113, 114]. It uses the partial charges in file.qtl. Spectra are calculated for the dipole allowed transitions, generating matrix elements, which are multiplied with a radial transition probability, and the partial densities of states. The calculations is done with several individual programs (initxspec, tetra, txspec, and lorentz) which are linked together with the c-shell script xspec. In our case the calculations have been done step by step:

- INITXSPEC generates the appropriate input file.int, according to the dipole selection rule, for the subsequent execution of the tetra program.
- TETRA generates the appropriate densities of states for (L+1) and (L-1) states respectively.
- TXSPEC calculates energy dependent dipole matrix elements. Theoretical X-ray spectra are generated using the partial densities of states and multiplying them with the corresponding dipole matrix elements.
- LORENTZ uses a Lorentzian convolutes the calculated spectra to account for lifetime broadening and for a finite resolution of the spectrometer.

4.3.3 Electron density plots

The LAPW5 program generates the charge density (or the potential) in a specified plane of the crystal on a two dimensional grid which can be used for plotting with an external contour line program (XCrysden). Depending on the input files one can generate valence or difference densities (i.e. crystalline minus superposed atomic densities).

[3]Local rotation matrices are used to rotate the global coordinate system (given by the definition of the Bravais matrix) to a local coordinate system for each atomic site. The local rotation matrix R, which transforms the global coordinates r to the rotated ones r', is defined by $Rr = r'$.

4.4 Modeling PCMO

We applied the $ab-initio$ LDA model to the room temperature crystal structure of PCMO, which is orthorhombic with space group $Pnma$ and lattice constants $a = 5.4071(3)$ Å, $b = 5.3409(7)$ Å, and $c = 11.7018(11)$ Å[115]. Since Pr and Ca atoms are located in the same crystallographic positions with an half-integer occupation and the WIEN2k code does not recognize two atoms in the same site, we adopted the *virtual crystal approximation*. This approximation consists in replacing the Pr atoms with Ca atoms with occupation equal to one[4]. In Fig.4.4 the input file.cif used for initializing the calculation is reported. In Fig.4.5 a picture of the PCMO crystal structure, obtained by

```
# CRYSTAL DATA
_symmetry_cell_setting              orthorhombic
_symmetry_space_group_name_H-M      'P n m a'
_symmetry_space_group_name_Hall     '-P 2ac 2n'
_symmetry_Int_Tables_number         62
loop_
_symmetry_equiv_pos_site_id
_symmetry_equiv_pos_as_xyz
1  '+X,+Y,+Z'
2  '1/2-X,1/2+Y,1/2+Z'
3  '+X,1/2-Y,+Z'
4  '1/2-X,-Y,1/2+Z'
5  '-X,-Y,-Z'
6  '1/2+X,1/2-Y,1/2-Z'
7  '-X,1/2+Y,-Z'
8  '1/2+X,+Y,1/2-Z'
_cell_length_a                      5.4071(3)
_cell_length_b                      10.6819(7)
_cell_length_c                      11.7018(11)
_cell_angle_alpha                   90.0000
_cell_angle_beta                    90.0000
_cell_angle_gamma                   90.0000
_cell_volume                        675.87(9)
```

```
                                    x          y          z
Ca(1) Ca -0.016400(10) -0.250000(10) 0.859300(10)
0.0035(2) 1.00 2 d SP . .
Ca(2) Ca 0.01430(3) -0.50084(3) 0.64445(3) 0.0106
(3) 1.00 1 d P . .
Ca(3) Ca 0.530700(10) -0.250000(10) 0.358300(10)
0.00528(14) 1.00 2 d SP . .
Mn(1) Mn 0.5000 0.0000 0.5000 0.00448(18) 1.00 2
d S . .
Mn(2) Mn 0.00604(5) -0.2500 0.50074(10) 0.00435
(19) 1.00 2 d S . .
O(1) O 0.2610(5) -0.1247(3) 0.4866(2) 0.0115(2)
1.00 1 d . . .
O(2) O -0.2421(7) -0.3741(4) 0.5126(2) 0.0129(3
1.00 1 d . . .
O(3) O 0.0503(10) -0.2500 0.6641(3) 0.0129(5) 1.00
2 d S . .
O(4) O -0.0401(13) -0.2500 0.3363(3) 0.0136(5) 1.00
2 d S . .
O(5) O 0.5337(13) 0.0008(2) 0.3322(4) 0.0205(7)
1.00 1 d . . .
                                    occupation
```

Figure 4.4: Input $file.cif$ containing the crystal structure data for initializing the calculation. In detail, the file contains: the cell symmetry, which is orthorhombic; the space group, which is *Pnma*; the 8 symmetry operations; the length of the crystal axes and the angle between them; the crystallographic position and occupation of the equivalent atoms.

means of a three- dimensional visualization system for electronic and structural analysis called VESTA, is shown. The *muffin-tin* sphere radii are set, according to the ionic radii, to 2.08, 1.85 and 1.64 Bohrs for Ca (Pr), Mn and O atoms, respectively, as shown in Fig.4.6. In the starting phases of the

[4]This approximation is reasonable since Pr and Ca atoms have the same nominal valency 2^+ and they have ionic radii quite similar (1.13 Å for Pr and 1.14 Å for Ca). This affinity makes these two atoms totally equivalent respect to the $muffin\ tin\ approximation$ that has been applied to the system.

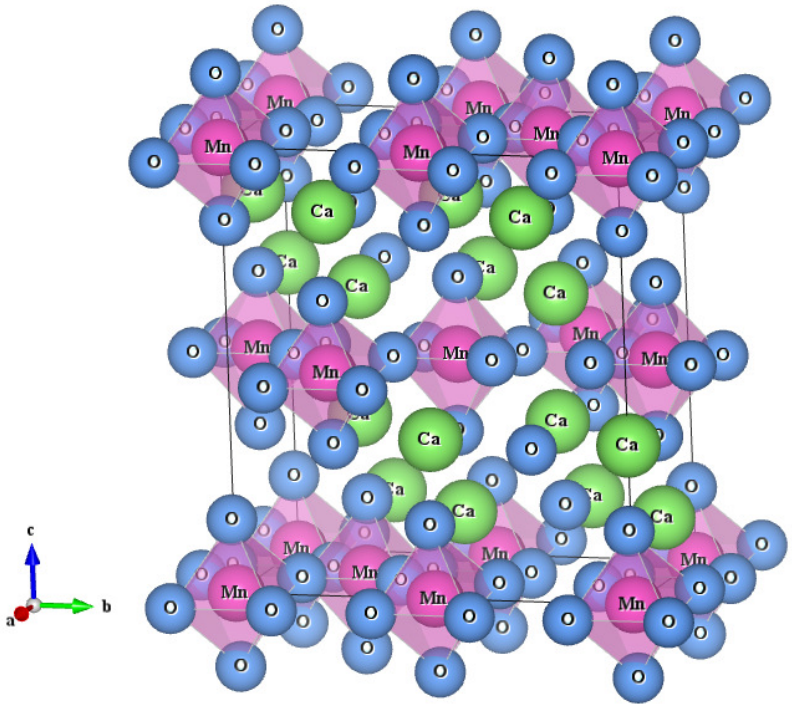


Figure 4.5: Crystal structure of PCMO at T=300K by means of the three-dimensional visualization system VESTA. The Mn, Ca and O atoms are colored in pink, in green and in blue, respectively.

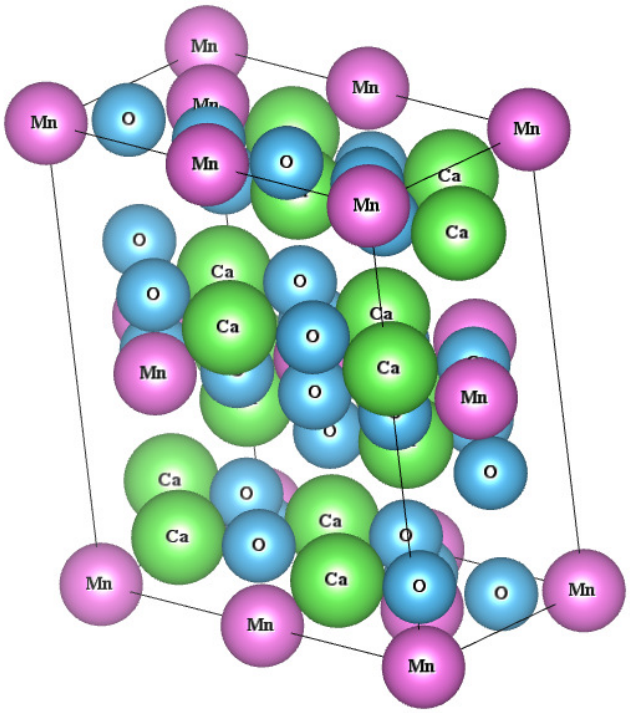


Figure 4.6: Representation of PCMO according to the *muffin-tin* approximation, where the atoms are represented by colored spheres and outside from these the potential is considered constant (see details in the text).

initialization of the calculation a new structure file is created (see Fig.4.7), in which the space group and the local rotation matrices for each atomic site are determined, and 8 space group symmetry operations are generated. The next

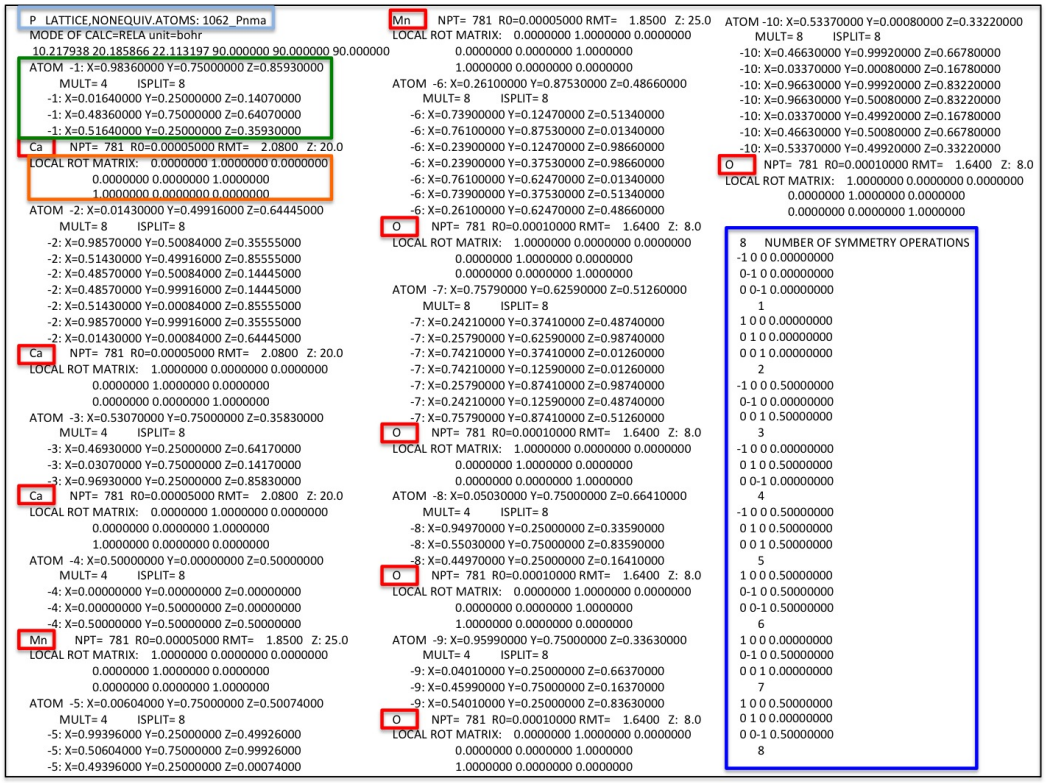
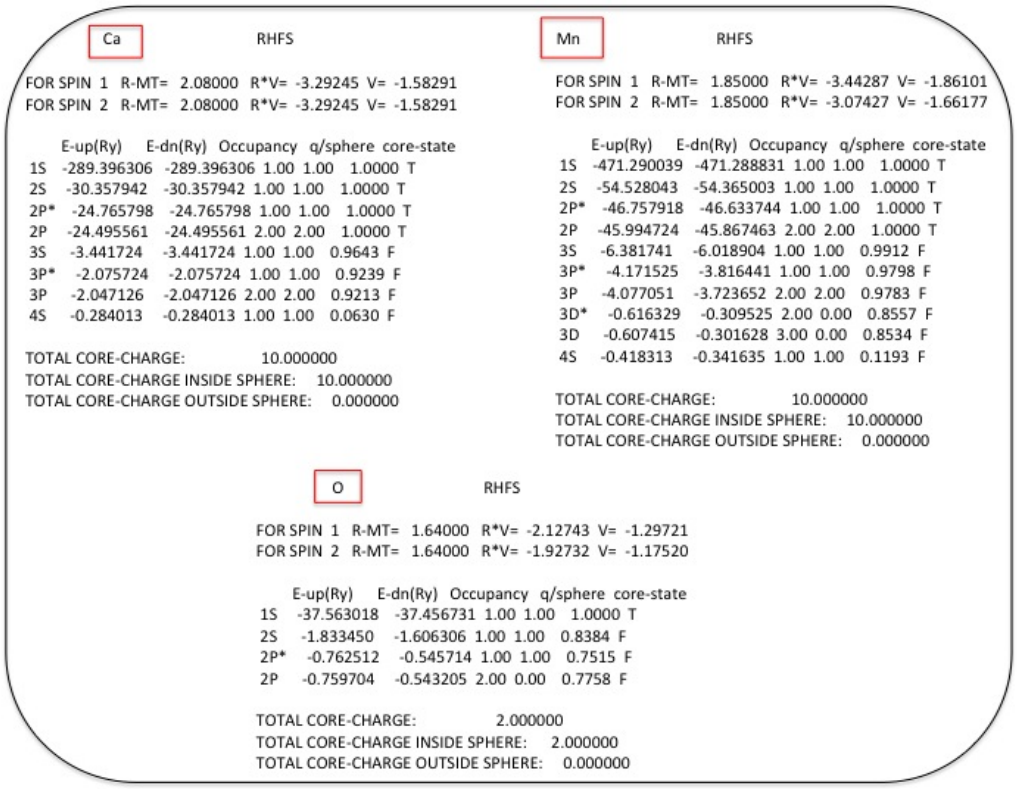


Figure 4.7: File.struct generated during the calculation initialization by the WIEN2k code. The file reports: the crystal space group (light blue square); the coordinates for each site symmetry (green square); the local rotation matrices (orange square); the symmetry operations (blue square).

step consists of choosing the cutoff-energy E_{cutoff} to separate core and valence states. After several attempts checking how much core charge leaks out of MT-spheres, I found the best value to be E_{cutoff}=-6.5 Ry. The Ca 3s and 4s, the Mn 4s, and the O 2s and 2p states have been treated as valence states (see Fig.4.8).

I put the cutoff parameter $R_{mt}K_{max}$=5 in order to reduce the time consumption for the calculation. I set 100 k points for integration over the Brillouin zone, which ensure a sufficient accuracy of the results. Once the calculation has been initialized, I run the SCF using as a constraint that the energy difference between successive iterations has converged below 0.001 Ry. I carried out a spin polarized calculation by means of the LDA exchange potential. In order to open the band gap and to take into account the fact that the system is strongly correlated, I applied to Mn $3d$ electrons an on-site Coulomb contribution U. After several attempts with different values of U, as it is shown in Fig.4.9, I found that the minimum value which opens the band gap is U=0.6



Ca RHFS

FOR SPIN 1 R-MT= 2.08000 R*V= -3.29245 V= -1.58291
FOR SPIN 2 R-MT= 2.08000 R*V= -3.29245 V= -1.58291

	E-up(Ry)	E-dn(Ry)	Occupancy	q/sphere	core-state
1S	-289.396306	-289.396306	1.00	1.00	1.0000 T
2S	-30.357942	-30.357942	1.00	1.00	1.0000 T
2P*	-24.765798	-24.765798	1.00	1.00	1.0000 T
2P	-24.495561	-24.495561	2.00	2.00	1.0000 T
3S	-3.441724	-3.441724	1.00	1.00	0.9643 F
3P*	-2.075724	-2.075724	1.00	1.00	0.9239 F
3P	-2.047126	-2.047126	2.00	2.00	0.9213 F
4S	-0.284013	-0.284013	1.00	1.00	0.0630 F

TOTAL CORE-CHARGE: 10.000000
TOTAL CORE-CHARGE INSIDE SPHERE: 10.000000
TOTAL CORE-CHARGE OUTSIDE SPHERE: 0.000000

Mn RHFS

FOR SPIN 1 R-MT= 1.85000 R*V= -3.44287 V= -1.86101
FOR SPIN 2 R-MT= 1.85000 R*V= -3.07427 V= -1.66177

	E-up(Ry)	E-dn(Ry)	Occupancy	q/sphere	core-state
1S	-471.290039	-471.288831	1.00	1.00	1.0000 T
2S	-54.528043	-54.365003	1.00	1.00	1.0000 T
2P*	-46.757918	-46.633744	1.00	1.00	1.0000 T
2P	-45.994724	-45.867463	2.00	2.00	1.0000 T
3S	-6.381741	-6.018904	1.00	1.00	0.9912 F
3P*	-4.171525	-3.816441	1.00	1.00	0.9798 F
3P	-4.077051	-3.723652	2.00	2.00	0.9783 F
3D*	-0.616329	-0.309525	2.00	0.00	0.8557 F
3D	-0.607415	-0.301628	3.00	0.00	0.8534 F
4S	-0.418313	-0.341635	1.00	1.00	0.1193 F

TOTAL CORE-CHARGE: 10.000000
TOTAL CORE-CHARGE INSIDE SPHERE: 10.000000
TOTAL CORE-CHARGE OUTSIDE SPHERE: 0.000000

O RHFS

FOR SPIN 1 R-MT= 1.64000 R*V= -2.12743 V= -1.29721
FOR SPIN 2 R-MT= 1.64000 R*V= -1.92732 V= -1.17520

	E-up(Ry)	E-dn(Ry)	Occupancy	q/sphere	core-state
1S	-37.563018	-37.456731	1.00	1.00	1.0000 T
2S	-1.833450	-1.606306	1.00	1.00	0.8384 F
2P*	-0.762512	-0.545714	1.00	1.00	0.7515 F
2P	-0.759704	-0.543205	2.00	0.00	0.7758 F

TOTAL CORE-CHARGE: 2.000000
TOTAL CORE-CHARGE INSIDE SPHERE: 2.000000
TOTAL CORE-CHARGE OUTSIDE SPHERE: 0.000000

Figure 4.8: File.outputst generated during the initialization of the calculation in which the separation between core and valence states for the different atoms (Ca, Mn and O) is applied. In particular, for each electron state the following informations are reported: the energy (expressed in Ry) for -up and -down states, the occupancy, the charge on the sphere (q/sphere) and if it is true (T) or not (F) that it is a core state.

Ry=8.16 eV. This value is in accordance with DOS calculations made for similar systems [3, 116]. These p-DOS with respect to x-, y- and z- directions have

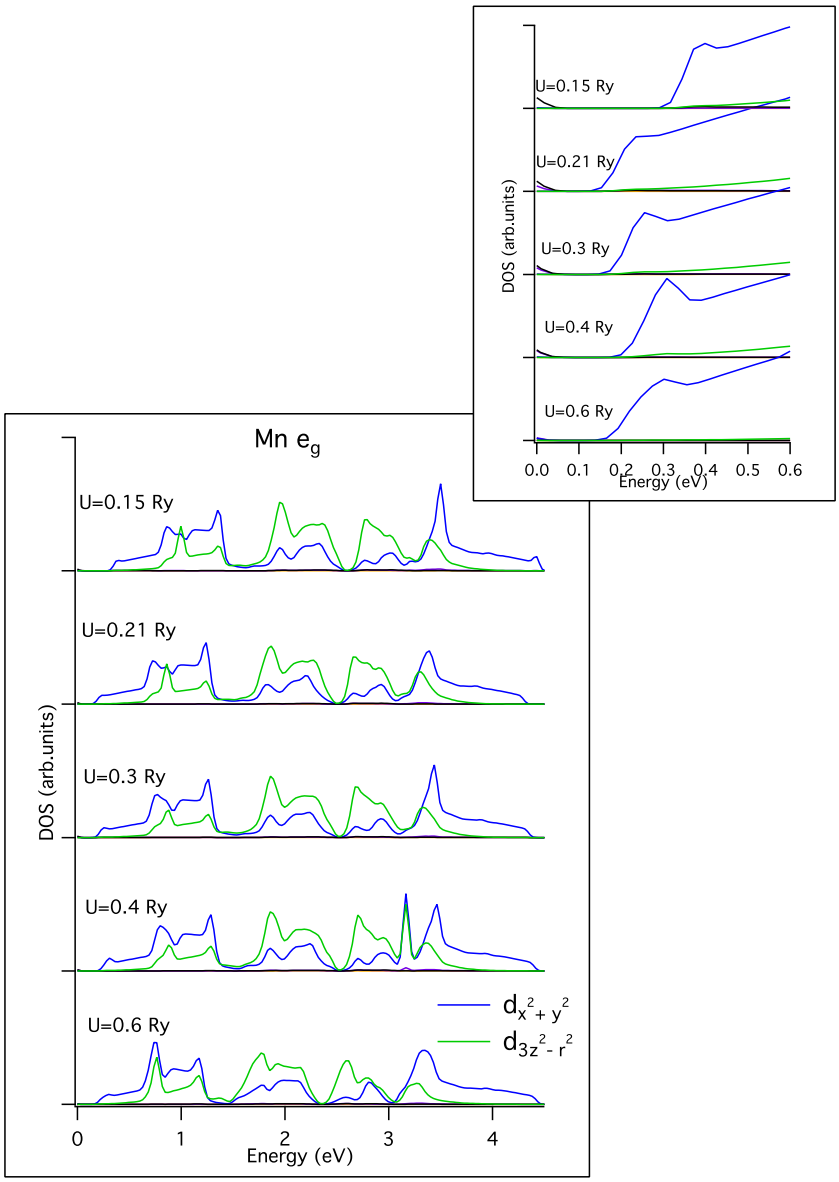


Figure 4.9: LDA+U Mn 3d p-DOS-up resolved with respect to the $d_{3z^2-r^2}$ (green curve) and $d_{x^2+y^2}$ (blue curve) symmetries for different values of U (0 eV corresponds to the Fermi energy). In the inset the energy region between 0-0.6 eV is pointed out.

been generated applying a rotation to the reference system. As it is sketched in Fig.4.10, the Mn-O bonding is not parallel to the crystallographic axis directions, but it is displayed on the diagonal. The rotation, which is 0 0 1 for c-axis and 2 1 0 for a-axis, has been applied to the Mn atoms and to the apical O atoms. In Fig.4.11 the input file with the applied rotation is reported.

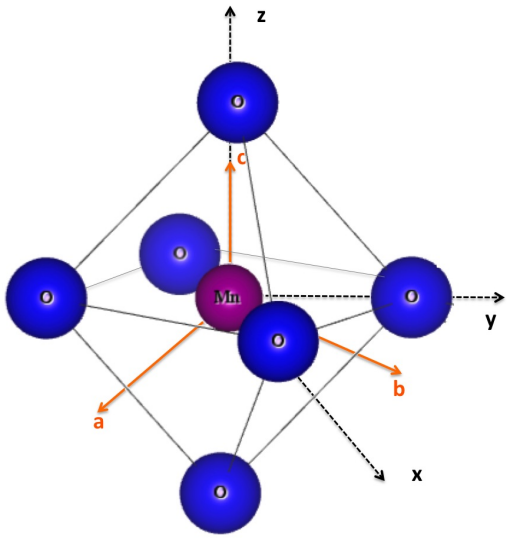


Figure 4.10: Sketch of the rotation of the reference system applied to the PCMO system. The a-, b- and c- axes (solid orange lines) have been rotated respect to the cartesian x-, y- and z- axes (dashed black lines).

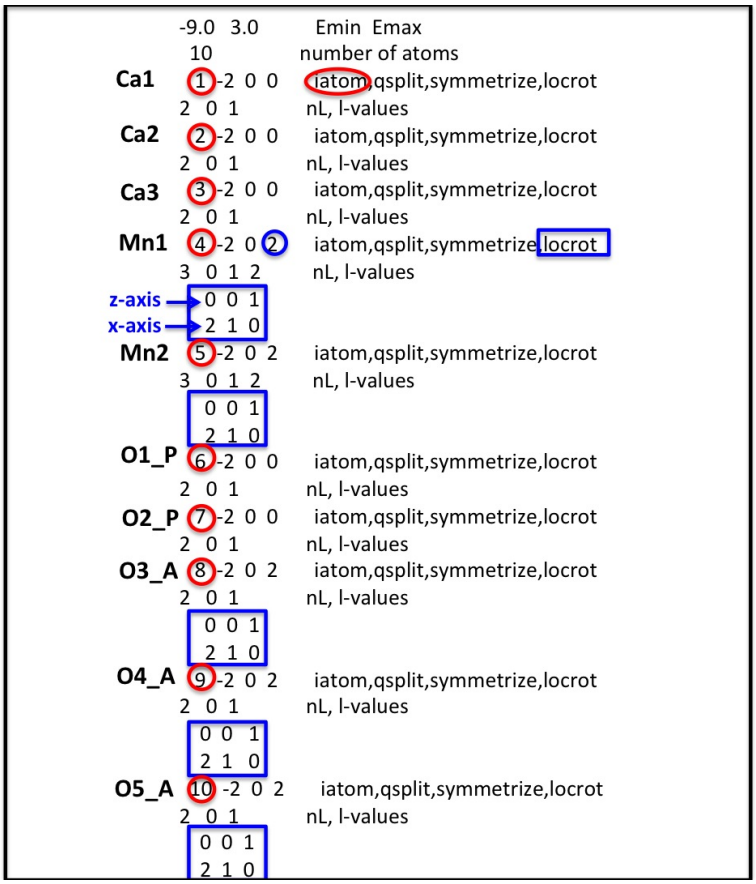


Figure 4.11: File.inq (input file for QTL program, see text for details). The number outlined in red indicate which atom is considered; in blue the applied rotation is outlined: the first line corresponds to the rotation of the *z-axis*, the second line to the rotation of the *x-axis*. The rotation is applied only to the Mn atoms (atom number 4 and 5) and to the apical O atoms (atom number 8, 9 and 10).

Chapter 5

Cases studied

This chapter presents the cases studied and it is divided into two sections: the case of hd-PCMO, including static and time resolved XAS measurements, and the case of the Ruddlesden-Popper series of Sr Ruthenates, investigated by means of RXES.

5.1 PCMO

5.1.1 Adiabatic phase transition in PCMO

Understanding the orbital physics of the rare earth manganates of the Ruddlesden-Popper single layered structure, having the general composition $RE_{1-x}A_xMnO_4$ (RE=rare earth; A=alkaline earth), is a complex and challenging question for its intimate correlation with the general problem of charge and magnetic ordering [117][118]. In many layered or pseudo-cubic manganite systems, orbital ordering is found to be at the origin of the anisotropy of the electron-transfer interaction, which may favor or disfavor the double-exchange interaction or super-exchange interaction that depends on orbital direction determined by a complex spin-orbital coupled state.

The mechanism that determines the ordering phenomena leading to these orbital effects is still matter of significant disagreement although, the orbital lattice coupling and the electron hopping (along with on-site Coulomb interaction) are generally believed to be the main mechanisms to be considered [118]. In this context, the single layered hd-PCMO is a case study for layered systems displaying charge, orbital and magnetic orderings. Interestingly though, hd-PCMO also displays a peculiar low temperature (orbitally induced) spin-lattice coupling that is missing in other rare-earth doped layered manganites. Furthermore, hd-PCMO exhibits a charge-orbital ordering (CO-O) transition at a remarkably high T_{CO} [119], slightly above room temperature, accompanied by an orthorhombic structural distortion [120], where the strongly correlated Mn e_g charge carriers order onto separate crystallographic sub-lattices (charge

ordered state) with a specific orbital character (symmetry) (orbital ordered state). Clear evidences of the CO-O transition come from the T dependence of the electrical resistivity ρ(T), which shows an inflection close to T_{CO} [19, 120] (see Fig.5.1). The sharp peak observed in the ac susceptibility χ(T)[19] at T_{CO}

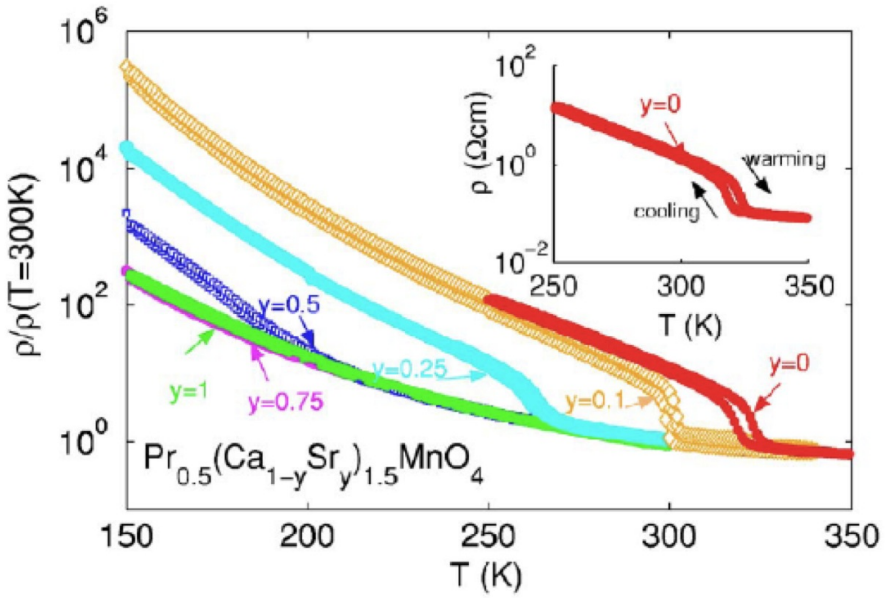


Figure 5.1: Temperature dependence of the normalized in-plane resistivity $\rho|\rho_{(T=300K)}$ for $Pr_{0.5}(Ca_{1-y}Sr_y)_{1.5}MnO_4$. The inset shows the resistivity ρ of the crystal with y=0 (PCMO) in absolute units [19].

and from neutron scattering results [121] showing: *i)* the appearance of the CO and antiferromagnetic (AFM) orders at two distinct temperatures; *ii)* an anomalous lattice response at temperatures 20K above the Neél temperature T_N[121, 122] which is associated to an unexpected spin-lattice coupling, as shown in Fig.5.2.

To elucidate the role of the Mn $3d$ - O $2p$ orbital topology, we measured the temperature dependence of the PCMO by XLD at the O-K and Mn-L thresholds, therefore achieving element and orbital selectivity [123]. In layered manganite systems, the XLD spectra at the O K- and Mn $L_{2,3}$-edges were extensively studied [3, 124–130] to assess the topology of the orbital states close to the Fermi level where the O $2p$ orbitals, σ-bonded to the Mn $3d_{3z^2-r^2}$ and $3d_{x^2-y^2}$ orbitals, are dominant [131–133]. While a number of XLD studies have been reported on layered manganites across the AFM transitions, experimental data across the CO-O transition are very limited. Furthermore, a study of the PCMO unoccupied electronic states is lacking.

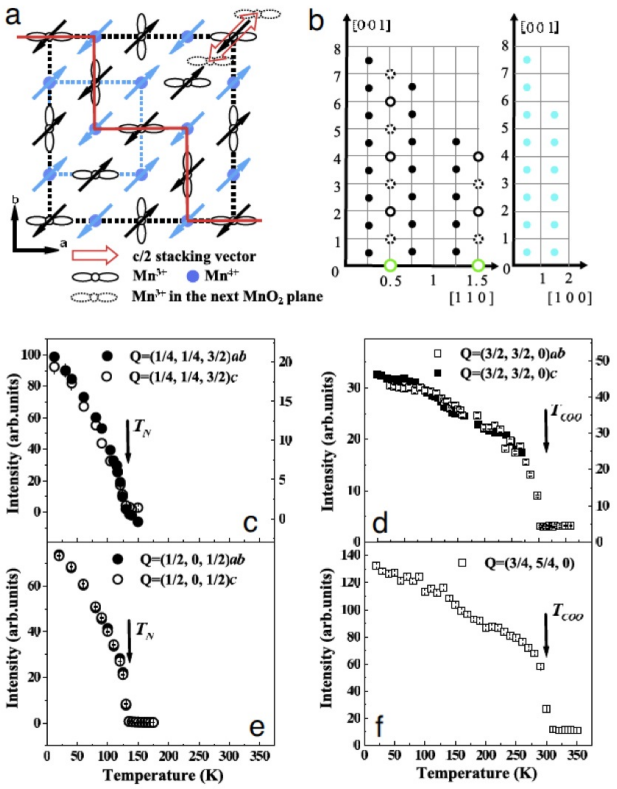


Figure 5.2: Structural scatterings and their temperature dependence. (a) Schematic view of the CE-type AF ordering in the MnO_2 plane. The black dashed line represents the periodicity of the unit cell for the Mn^{3+} sublattice, and the blue dashed line shows that of the Mn^{4+} sublattice. Possible spin arrangements in the c/2 stacking layers are marked by red arrows. The directions of Mn^{3+} orbitals form zigzag ferromagnetic chains (red line) that order antiferromagnetically. (b) The observed nuclear peaks (black open circles), CO/OO-induced superlattice peaks (green open circles) and magnetic ordering (solid circles) in reciprocal space. The dotted open circles represent the observed weak nuclear peaks that are disallowed by orthorhombic symmetry, indicating that the symmetry is lower than orthorhombic. Temperature dependence of the AF peak intensity from (1/4, 1/4, 3/2) (c) and (1/2, 0, 1/2) (e) and temperature dependence of CO/OO peak intensity from (3/2, 3/2, 0) (d) and (3/4, 5/4, 0) (f) are shown [121].

Here we investigate the temperature dependent XLD [134–136] at the O K threshold. The reported investigation assesses the nature of the unoccupied DOS by means of a detailed study supported by *ab-initio* calculations of the O K threshold and the relative XLD signal measured at three distinct phases of the PCMO [121]. The analysis of the LD at the O K edge allows to map and disentangle the partial density of empty O $2p$ states at the oxygen site and the local symmetry of the Mn empty states at once, since the O $2p$ states are hybridised with the metal states [137]. The oxygen data are completed and corroborated by the XLD data taken at the Mn $L_{2,3}$. The spectra are qualitatively discussed and compared with experimental and calculated data found in the literature in order to assess the orbital and magnetic state of the sample. Finally, we report important information about the intra-layer redis-

tribution of the ligand holes, that is associated to an increasing of the energy difference between $d_{3z^2-r^2}$ and $d_{x^2-y^2}$ orbitals and a dramatic change of the Mn L_3 linear dichroic signal below T_{CO}. We interpret the former two effects as the out-of-plane charge carriers localization resulting from the competing orbital-lattice coupling and the electron hopping charge dynamics, being the latter a signature of the onset of the e_g orbital order.

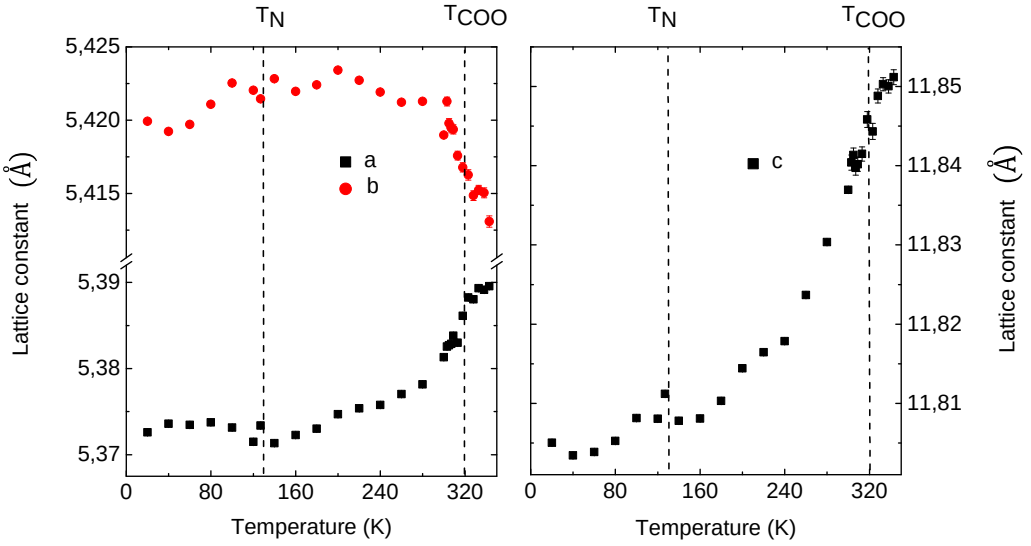


Figure 5.3: Temperature dependence of the a, b and c lattice parameters. The dashed lines near 320 K and near 130 K marks T_{COO} and T_N. Whereas the in-plane a and b lattice parameters show clear anomalies around T_{COO} and T_N, the c-axis lattice parameter changes smoothly across both transitions [138].

5.1.1.1 Experimental procedure

This work was carried out on beamline BACH [70, 71] at the Elettra radiation synchrotron facility. Single crystal PCMO was grown using a floating zone technique. For the experiments, crystal platelets of the desired orientation were cut from a single grown rod. The lattice structure and high sample quality was confirmed by X-ray diffraction experiments. The sample was mounted with the c-axis of the crystal perpendicular to the beam direction as sketched in Fig.5.4. The scattering angle was set at 0° in order to avoid spurious matrix element and geometrical effects. The sample temperature during the experiment was monitored by a thermocouple attached to the sample. The crystal was broken in UHV condition (5×10^{-10} mbar) and the presence of surface contaminants was checked measuring the C *1s* spectra by x ray photoemission. The high quality of the single crystal and the structural characterization of the ordered non-ordered phases have been tested by X-ray diffraction on the same single crystal (see Fig.5.3, panel a).

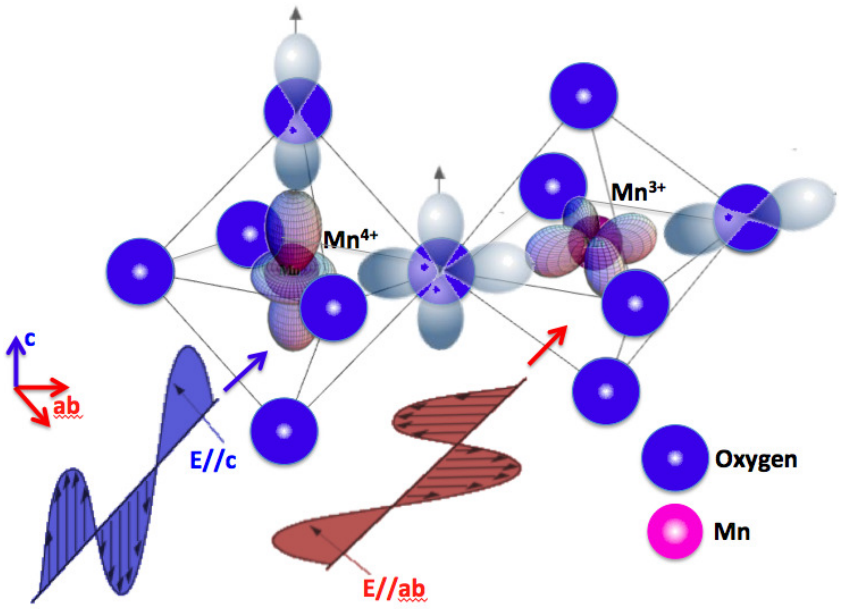


Figure 5.4: Scheme of the light electric field components with respect to the orientation of the Mn e_g and O $2p$ orbitals in the Mn-O octahedra of the PCMO single crystal. The vertical light ($E \parallel c$) polarization (blue) probes the out of plane states and the horizontal ($E \parallel ab$) one (red) probes the in plane states[123].

Table 5.1: The energy difference $\Delta E = \epsilon(d_{3z^2-r^2}) - \epsilon(d_{x^2-y^2})$, $\Delta = \Delta E + \delta$ (see Fig. 5.5 panel b) and the core-hole energy difference δ (see Fig. 5.5 panel e) at the in- and out-of-plane oxygen sites.

T (K)	ΔE (eV)	Δ (eV)	δ (eV)
100	0.58	1.21	0.63
300	0.57	1.2	0.63
350	0.46	1.09	0.63

The endstation is fitted with a variable temperature sample holder for total electron yield (TEY) measurements. The XAS spectra were taken at the Mn $2p$ and O $1s$ edges varying the x ray beam linear polarization in order to measure XAS linear dichroism, from $E \parallel c$ (vertical polarization) to $E \parallel ab$ (horizontal polarization) (Fig.5.4). The XAS spectra were measured in TEY mode in order to minimize the strong self-absorption effects present at the Mn L_3 edge. Finally, XAS spectra were normalized to the beam flux and aligned on the photon energy scale using Fermi edges recorded from an Au foil.

5.1.1.2 Results and Discussion

O K edge The polarization dependent O K XAS (O $1s \rightarrow 2p$) spectra taken at three different temperatures (above the CO-O transition ($T_{340K} > T_{CO(=320K)}$), below T_{CO} ($T_N < T_{300K} < T_{CO(=320K)}$), and below the AFM transition ($T_{100K} < T_{N(=120K)}$) are shown in Fig.5.5, panels b, c and d respec-

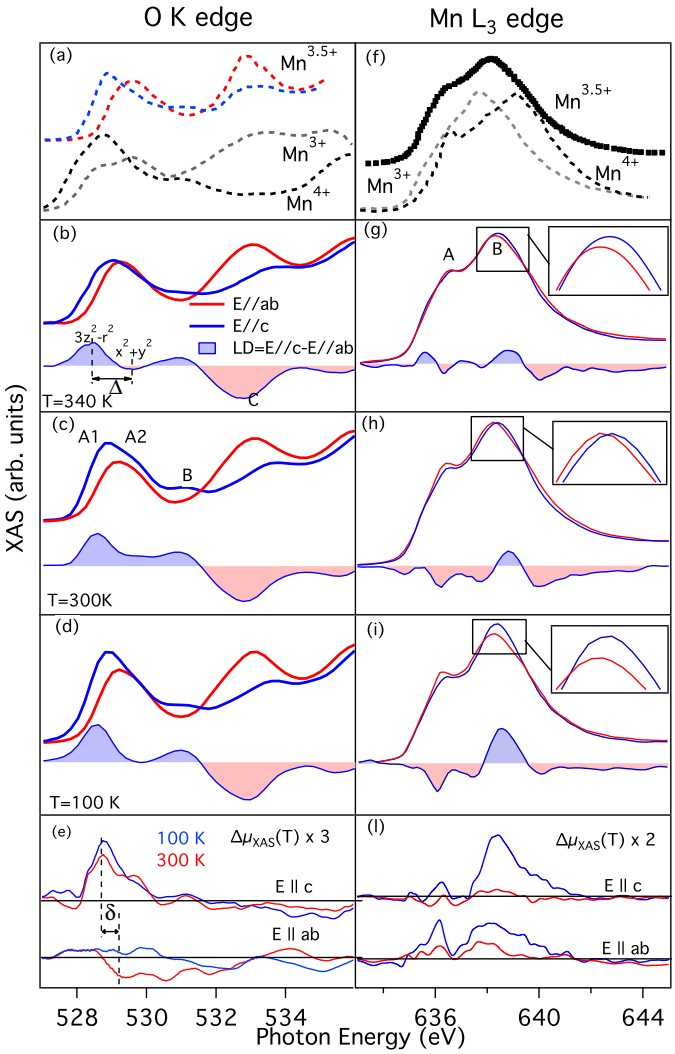


Figure 5.5: Polarization dependent O K (on the left) and Mn $L_{2,3}$ (on the right) XANES spectra of $Pr_{0.5}Ca_{1.5}MnO_4$, measured with the electric field E along the ab-axis (red curve) and along the c-axis (blue curve), taken at three different temperatures corresponding to the charge-orbital disordered (panel b and g), ordered (panel c and h) and AFM (panel d and i) states. For each pair of spectra the XAS linear dichroism (LD=$XAS_{E\|c}$ - $XAS_{E\|ab}$) is reported. The top panels show O K (panel a) and Mn $L_{2,3}$ (panel f) XAS spectra of different reference compounds: (a) LSMO[124] measured with $E \parallel ab$ (dotted red curve) and $E \parallel c$ (dotted blue curve), $CaMnO_3$[139] (dotted black curve) and $LaMnO_3$[139] (dotted gray curve); (f) MnO_2[140] (dotted black curve), $LaMnO_3$[140] (dotted gray curve) and $La_{0.5}Sr_{1.5}MnO_4$[141] (heavy black curve). The bottom panels show the corresponding spectral variations, $\Delta\mu_{XAS}(T) = \mu_{XAS}(T) - \mu_{XAS}(350K)$, as a function of temperature (see text) [123].

tively. The corresponding linear dichroic (LD) spectra, defined as the difference between the out-of-plane and the in-plane polarizations, i.e. LD=$XAS_{E\|c}$-$XAS_{E\|ab}$, are also reported. In addition, we calculated $\Delta\mu_{XAS}(T) = \mu_{XAS}(T) - \mu_{XAS}(350K)$ (Fig.5.5 panel e) which directly represents the spectral variations

versus temperature. In a configuration approach, the strength of O $1s \rightarrow 2p$ transition is determined by the weight of the $3d^5\underline{L}$ ground state. Therefore, the absorption strength for the E‖c and E‖ab incoming photon polarizations reflects the symmetry of the unoccupied Mn $3d$ orbitals and selectively probes the Mn-O_{Apical} and Mn-O_{planar} bonds, respectively, allowing to probe the 3D oxygen orbital topology.

The O K XAS spectra of hd-PCMO display four prominent features in the [527.5-536] eV range, which are marked as A_1, A_2, B and C (see Fig.5.5 panel c) showing a notable dichroism between E-field parallel to the c axis or the ab plane. The lineshape of the O K edge is similar to the O K edge measured in other layered manganites - and other perovskites as well. In particular, the first 5-8 eV above the absorption edge are characterized by the strong hybridization between O $2p$ and Mn $3d$ orbitals [127, 133, 142, 143]. For PCMO the first spectral energy region, between 527.5 eV and 530.5 eV, shows a double-peak feature (A_1 and A_2) in the $E \parallel c$ polarization geometry, whereas only a single-peak feature (A_2) is detected in $E \parallel$ab geometry [124, 131].

A comparison between the PCMO spectra and their equivalent measured on the half-doped $La_{0.5}Sr_{1.5}MnO_4$ (hd-LSMO) (Fig.5.5, panel a) allows to assign the feature A_1 to the Mn $3d_{z^2}$-O(A) $2p_z$ bonding, whereas the feature A_2 is ascribed to the planar O $2p_x$ and O $2p_y$ orbitals hybridized with Mn $d_{x^2-y^2}$ states. These states are energetically close to the spatially isotropic Mn t_{2g}-down states [124, 128, 131, 144]. Because of the different orbital geometry and the difference in the absorption energy (Δ) for the in-plane and out-of-plane $3d$ orbitals, the measured LD XAS signals exhibit features that support the above assignments. The calculations corroborate the observed linear dichroism by revealing that the Mn e_g up- and down- states and the t_{2g} states extend for 7 eV. The apical O p_z are found to strongly overlap with the Mn $d_{3z^2-r^2}$ (up and down) and the $3d_{xz,zy}$ down states. Ergo, the different p-DOS distributions of the O p_z (parallel to the c-axis) and O p_{xy} DOS (parallel to the ab-plane) explain the dichroic effect observed in the O K XAS spectra.

The feature B is commonly ascribed to either t_{2g} down states or to an upper Hubbard band [124, 125]. A direct comparison between the measured XAS spectra on PCMO and those taken on Mn^{4+} ($CaMnO_3$) [139] and Mn^{3+} ($LaMnO_3$) [139] can help to clarify this assignment. For E‖c, the PCMO XAS spectrum mirrors that of the Mn^{4+} (strong A_1, B present), while for E‖ab it resembles that of Mn^{3+} (A_1 strongly depleted, A_2 present, B absent). Correspondingly, the B feature can be attributed to the direct hybridization of Mn $3d_{z^2}$-O(A) $2p_z$ and $3d_{xz,yz}$-O(P) $2p_z$. That is confirmed by the calculated oxygen p-DOS for the apical and basal oxygens as shown in Fig.5.7. Finally, the observed affinity reflects the electronic anisotropy in this electronic ground states for the Mn ions. In fact, we observe a Mn^{4+}-like character along the c-axis and a Mn^{3+}-like character in the ab basal plane. This anisotropy reflects the almost complete localization of the e_g charge carriers in the low energy out-of-plane orbitally polarized states, as expected for a layered structure.

The tendency of the charge carriers to localize in the lowest unoccupied energy state can be frustrated by the electron hopping mechanism. This mechanism, as discussed in the following, tends to delocalize the charges in the basal plane.

The energy difference $\Delta E = \epsilon(d_{3z^2-r^2}) - \epsilon(d_{x^2-y^2})$ versus temperature (see table 5.1) has a ground state depending on two competing mechanisms. The local MnO_6 distortion, that removes the Mn $3d$ orbital degeneracy forcing the charge carriers in the out-of-plane $3d_{z^2}$ orbital and the charge dynamics of electron hopping, that tends to delocalize the charges in the basal plane. Considering the core-hole binding energy difference (δ, see Fig.5.5 panel e) at the apical and basal oxygen sites due to the different coordination, it is also possible to estimate the orbital energy difference $\Delta E = \Delta - \delta$.

In order to study how the charge-orbital order-disorder phenomena affect ΔE, the O K XAS spectra, along with the related XLD, and $\Delta\mu_{XAS}(T)$ signals versus T must be considered. For each polarization the XAS edges are conserved, beside some irrelevant variation of the main features intensity. In the charge-orbital disordered phase ($T = 340K$), the intensities of A_1 and A_2 are identical, whereas the intensity of B is less pronounced with respect to the low temperature cases. When the system undergoes the CO-O transition, its unit cell shows a strong enhancement of the orthorhombic strain in the basal Mn-O plane for allowing the orbital ordering to be established [121].

The orthorhombicity of the MnO_6 octahedra reflects in a change of the conduction band DOS, characterized by the appearance of a double peak feature which now appears as a distinct double peak feature in the $E \parallel c$ XAS spectra (Fig.5.5 panel e). Consistently, $\Delta\mu_{XAS}(T = 300K)$, for $E \parallel ab$, is positive and double peaked (A_1 and A_2) proving an increased DOS for the out-of-plane states. Interestingly, the corresponding variation of $\Delta\mu_{XAS}(T = 300K)$ for $E \parallel ab$ is negative.

Therefore, the associated decreasing of the Mn-O_{planar} distance (see top panel of Fig.5.6) and the increasing difference of the basal Mn-O_{planar} distances in the CO-O phase, result in an injection of holes in the out-of-plane states and a reduction of the in-plane oxygen $2p$ DOS, i.e. in a charge transfer from out-of-plane to in-plane states. This mechanism seems to be in contrast with the increasing value of ΔE (from 0.46 eV (disordered phase) to 0.57 eV (ordered phase)). Indeed, this process would favor the transfer of charge carriers in the out-of-plane electronic states. This apparent disagreement can be overtaken by considering the binding energies of the Mn e_g ground state resulting from the Coulomb term of the crystal field (CF) and the kinetic term of electron hopping (eh):

$$\begin{aligned} \Delta E = & (-CF(d_A) + eh(d_A))_{3z^2-r^2} \\ & - (-CF(d_P) + eh(d_P))_{x^2-y^2} \end{aligned} \tag{5.1}$$

where d_A and d_P are the Mn-O_A and Mn-O_P distances, respectively. Since the reduced out-of-plane/in-plane orthorhombicity tends to reduce the CF term,

the competing out-of-plane/in-plane $p-d$ hybridizations (eh term) results in a larger ΔE. Furthermore, the decreased in-plane hopping integral can explain the increased resistivity below T_{CO} [19].

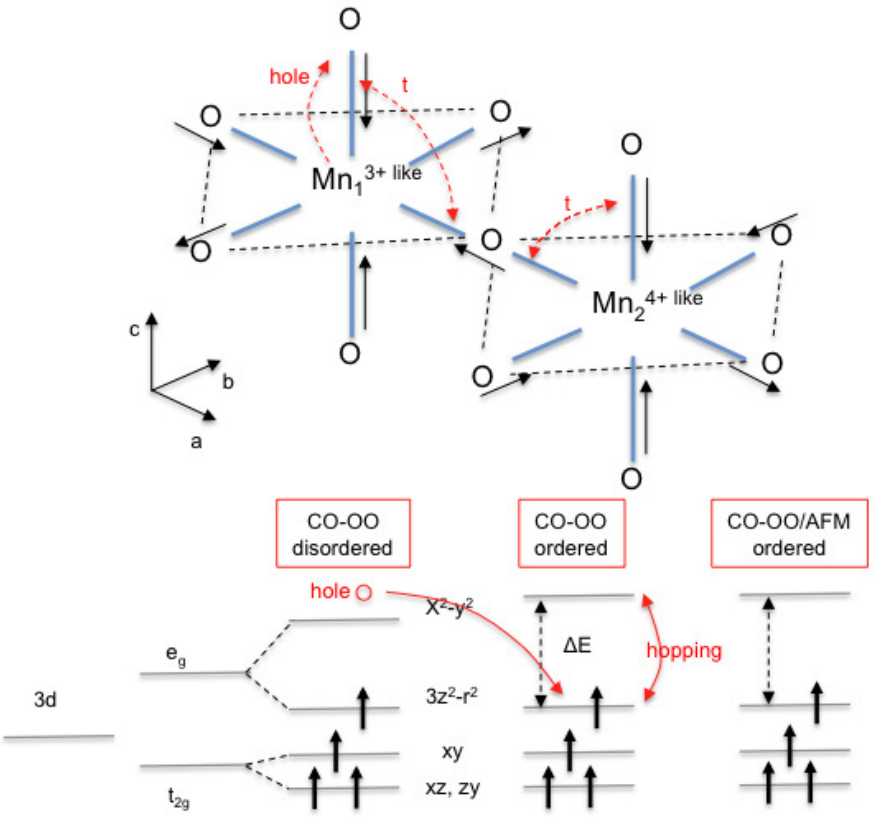


Figure 5.6: Top: sketch of the orthorhombic distortion of the adjacent Mn^{3+}-like and Mn^{4+}-like MO_6 octahedra. Bottom: schematic energy diagram of the Mn $3d$ electronic states in the CO disordered and ordered phases [123].

Interestingly, in the [528-531 eV] energy range the intensity of $\Delta\mu_{XAS}(T = 100K)$ for $E \parallel c$ increases further upon cooling, whereas the A_1/A_2 intensity ratio increases for the lower energy state. This observation can be ascribed to the additional decrease of the Mn-O(a) distance resulting in a rise of the out-of-plane DOS. Conversely, the corresponding variation of $\Delta\mu_{XAS}(T = 100K)$ for $E \parallel ab$ is positive. This finding is consistent with the reduced in-plane orthorhombic distortion. Therefore, the distinct behavior of the spectral variations $\Delta\mu_{XAS}(T)$ at T=300 K and 100 K can be explained by considering the reduced orthorhombicity taking place slightly above T_N.

Notably, the energy difference ΔE (see table 5.1, T=100 K and T=300 K) remains equal to the value above T_N. This proves that the $3d$ e_g splitting and the charge dynamics electron hopping are not affected by the AFM ordering.

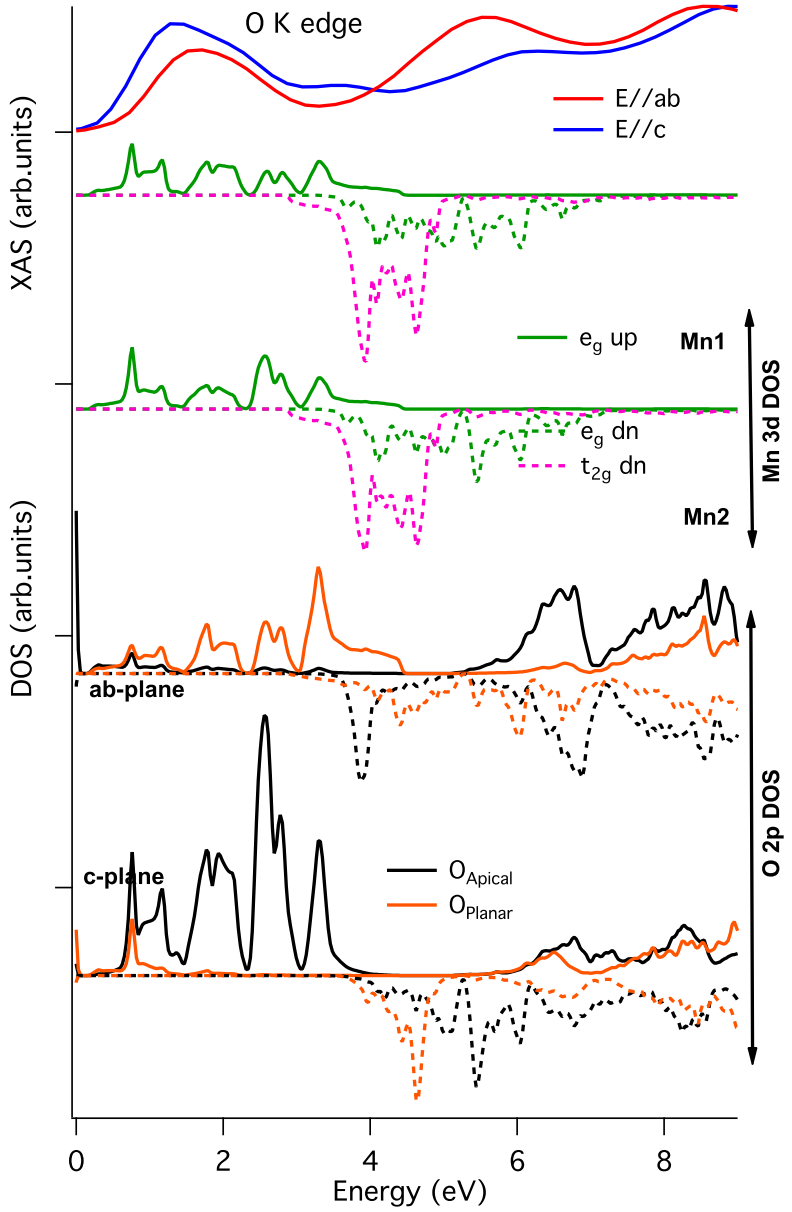


Figure 5.7: Comparison of the experimental O K XAS spectra for $E \parallel ab$ (red curve) and $E \parallel c$ (blue curve), measured at T=300 K, to the calculated O $2p$ and Mn $3d$ p-DOS. The Mn $3d$ p-DOS -up (solid line) and -down (dotted line) are singled out between the two atomic sites Mn_1 and Mn_2 and resolved with respect to the e_g (green curve) and t_{2g} (pink curve) symmetries. The O p-DOS -up and -down are projected along the a-, b- and c-directions and singled out between planar (orange curve) and apical (black curve) oxygen sites [123].

Simulated O K XAS spectra I report here (see Fig.5.8) the calculated O K edge XAS spectra by means of LDA+U for $E \parallel ab$ and $E \parallel c$ compared with the experimental one for the CO-OO phase. The three main features (A1, A2, and C) are quite well reproduced. Anyhow there are some discrepancies between the experimental and the calculated spectra. Among them the most

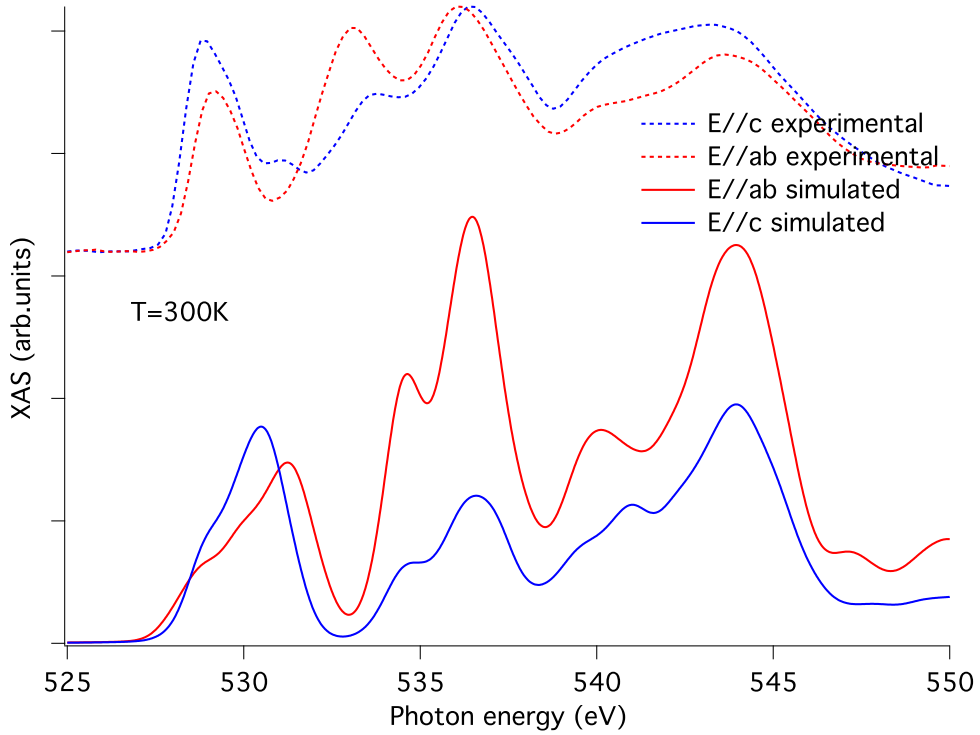


Figure 5.8: Comparison of the experimental (dashed line) and simulated by LDA+U (solid line) O K XAS spectra for $E \parallel ab$ (red curve) and $E \parallel c$ (blue curve) at T=300K.

evident are the high energy part of the spectra and the lacking of the B peak in the $E \parallel c$ spectrum. It is quite reasonable that these discrepancies are due to *core hole effects*[1] that have been not taken into account in the calculation.

Mn L_3 edge The oxygen data are completed and corroborated by the XLD data taken at the Mn $L_{2,3}$. The XLD at the Mn $L_{2,3}$ are qualitatively discussed and compared with experimental and calculated data found in the literature in order to assess the orbital and magnetic state of the PCMO sample. Fig.5.5 shows the polarization dependent Mn $2p$ XAS spectra as measured for the CO/OO disordered (at $T > T_{CO}$ panel g), ordered ($T_N < T < T_{CO}$ panel h), and the CO/OO antiferromagnetic ($T < T_N$ panel i) phases. The Mn L_3 linear dichroic signals and the spectral variations $\Delta\mu_{XAS}(T)$ (Fig.5.5, panel j) are also reported.

The spectra are compared to the corresponding spectra of the formally tetravalent Mn^{4+} (MnO_2[140]), trivalent Mn^{3+} ($LaMnO_3$ [140]) and half doped $Mn^{3.5+}$ (LSMO[3]). This qualitative comparison confirms the $3d^{3.5}$ configuration of the Mn ions in PCMO and the admixture of Mn^{4+}-like and Mn^{3+}-like sites, regardless of the temperature.

The main spectral features (A and B) stem from excitations of core elec-

[1]The presence of an hot screened core hole must be considered in the calculation of the XAS matrix elements.

trons from the $2p$ manifold to unoccupied $3d$ states, i.e., transitions from $2p^6 3d^n$ ground states to different excited multiplet configurations.

Accordingly with *ab-initio* calculations on similar layered manganites [127, 145, 146], the Mn L_3 lineshape is determined by the coexistence of Mn^{4+}-like and Mn^{3+}-like ions, while the structure A reflects the presence of Mn^{4+}-like sites.

The intensity and the energy positions of these features and of the overall L_3 lineshape exhibit a significant linear dichroism upon the change of polarization. Considering the disordered state ($T > T_{CO}$), the observed dichroism reflects the electronic ground state anisotropy induced by the local orthorhombic strain of the MnO_6 octahedra. This distortion significantly affects the LD signal, clearly proved by the direct comparison between the XLD reported in panels (a) and (a') of Fig.5.9, where the LD for hd-PCMO at $T > T_{CO}$ and the calculated hd-LSMO data [147] are compared. The results shown in Fig.5.9 (a') derive from a many body cluster calculation for a tetragonally distorted MnO_6 cluster with a δ=0.05 being δ the difference between apical and basal Mn-O distances.

When T is brought below T_{CO}, the Mn L_3 LD signal displays dramatic variations with respect to the disordered phase, as shown in Fig.5.9. For $T < T_{CO}$, the LD lineshape exhibits a pronounced negative-positive double-peaked contour in the L_3 region with the primary peaks corresponding to the A and B features of $L_{2,3}$. The LD signal for hd-PCMO at T=300K (Fig.5.9 b) can be compared to the measured LD signal for hd-LSMO at T=150K where this compound is orbitally ordered (top spectrum of Fig.5.9 b')[141]. The two LD signals are very similar and both are in agreement with the theoretically calculated Mn^{3+} $3x^2 - r^2/3y^2 - r^2$ (*rod-like*) orbital occupation (bottom spectrum of Fig.5.9 b')[141]. These LD spectra have been simulated using the well-established configuration interaction cluster model including the full atomic multiplet theory.

However, it must consider that the LD signal is a linear combination of both a structural and an orbital ordering contributions. Hence, this argument has only a qualitative relevance.

Finally, the positive variation of $\Delta\mu_{XAS}(T = 300K)$ along the ab-plane is convoyed by a change of the relative intensities of peaks A and B. For the intensity of peak A is related to the relative concentration of Mn^{4+}-like sites[127, 132, 149], the above mentioned variation can be attributed to a disproportion of the different Mn sites induced by the charge ordering. When T is below T_N, in the AFM phase, the overall lineshape of the LD signal remains nearly identical to those detected for higher T, except for the dramatic intensity increase of the LD main spectral features. It is worth noting that the LD signal below T_N is now a linear combination of different contributions originating from the orthorhombic distortion, the orbital ordering and the AFM induced anisotropy. Since the orbital ordering contribution to the LD signal should remain constant versus temperature, the intensity increase of $\Delta\mu_{XAS}(T = 100K)$ is originated by the AFM contribution. The AFM contribution shown

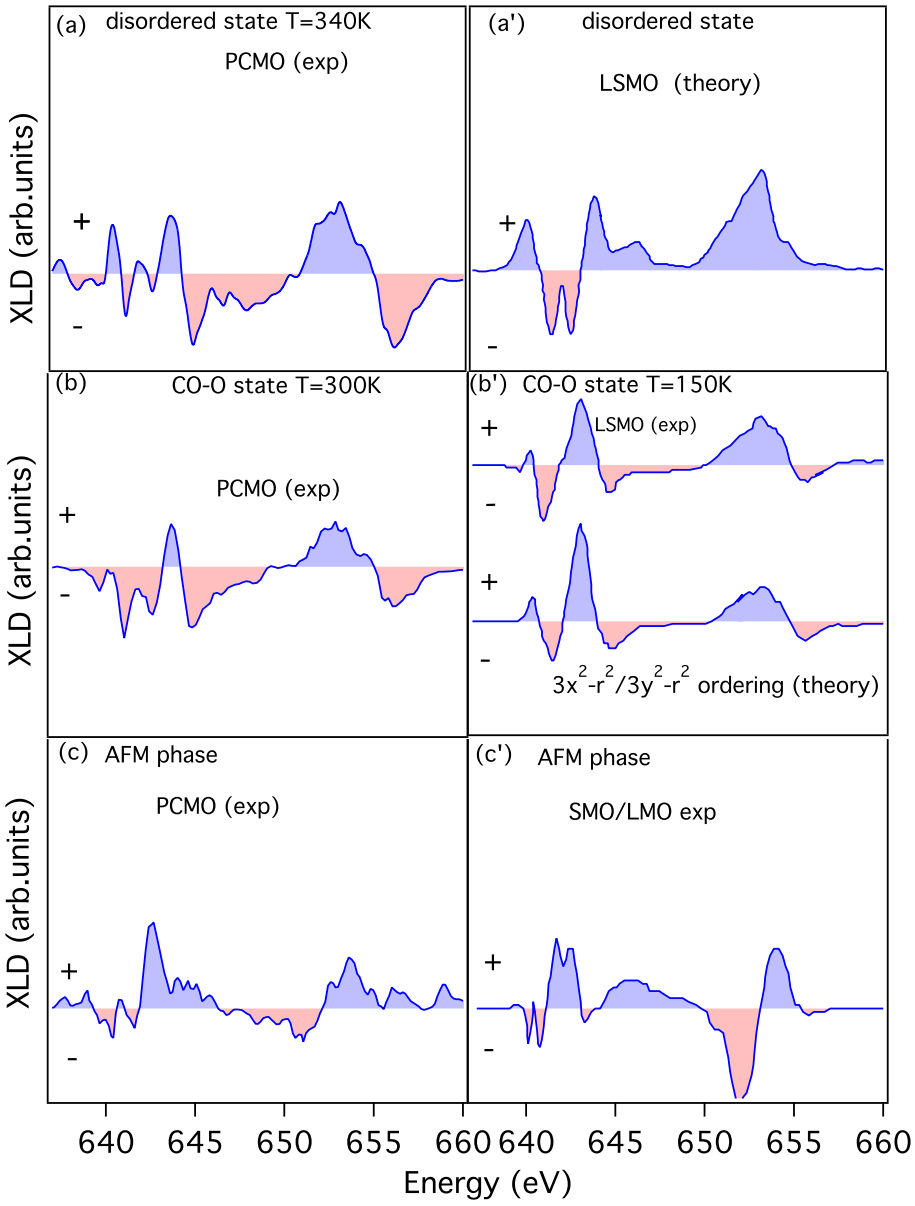


Figure 5.9: (a) Mn L_3 linear dichroism (LD=XAS$_{E\|c}$-XAS$_{E\|ab}$) signal measured at T=340K for hd-PCMO; (b) LD signal at the Mn $L_{2,3}$ edge measured at T=300K for hd-PCMO; (c) LD signal at the Mn $L_{2,3}$ edge for hd-PCMO obtained by the difference between LD at 100K and LD at 300K; (a′) LD signal calculated for hd-LSMO[147]; (b′) LD signal at T=150K for hd-LSMO [141] and theoretically calculated for orbital scenarios with Mn^{3+} $3x^2-r^2/3y^2-r^2$ orbital occupation [141]; (c′) AFM signal for SMO/LMO films [148].

in Fig.5.9 (c) has been obtained by taking the difference between the LD at 100 K and LD at 300 K, and is compared to the AFM signal measured by Aruta et al.[148] on the SMO/LMO films (see Fig. 5.9c').

5.1.1.3 Conclusions

In conclusion, the close inspection of the XLD and of the $\Delta\mu_{XAS}(T)$ signals uncovers crucial clues on the effects of CO ordering on the low energy unoccupied states resulting from the strong anisotropy of the Mn $3d$ - O $2p$ hybridized states. The present results show that the competitive interplay between the local atomic distortion, necessary for accomodating the CO-O ordering and the charge dynamics of the hopping mechanism, regulates the orbital state of the charge carriers. In fact, while the diminished local distortion reduces the tendency of the charge carriers to localize in the lowest energy out-of-plane state, the different in-plane and out-of-plane $d-p$ hybridization frustrates the $d_{3z^2-r^2} \leftrightarrow d_{x^2-y^2}$ hopping disfavoring the in-plane charge transfer interaction between adjacent Mn sites.

5.1.2 Time resolved XAS study of the 'hidden' photoinduced phase transition in PCMO

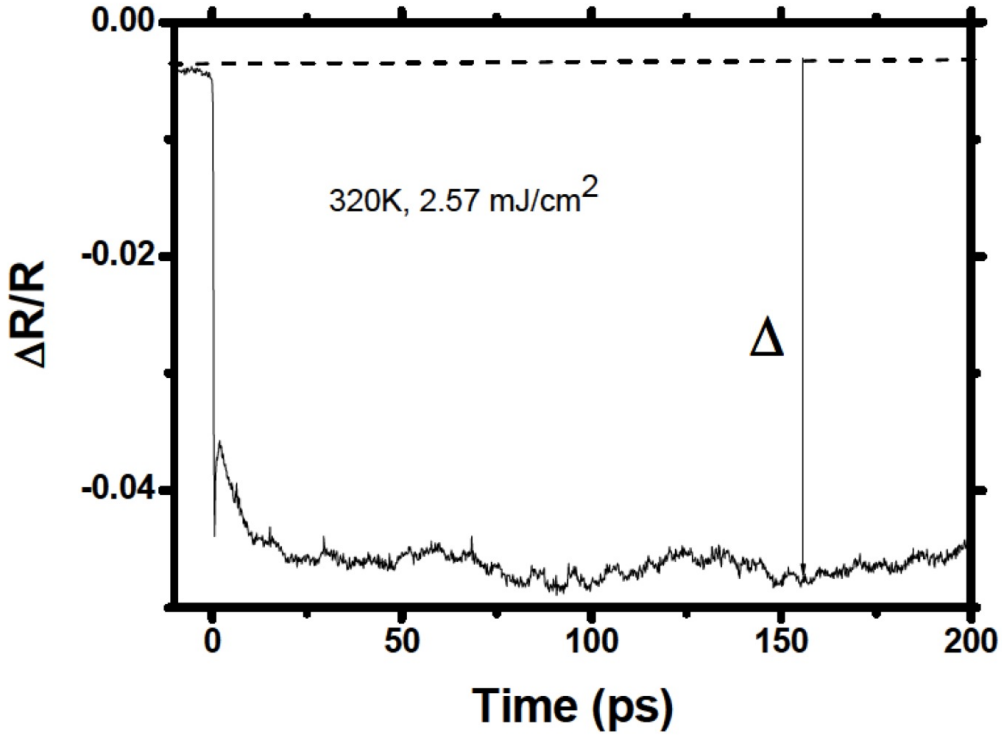


Figure 5.10: The transient reflectivity at 320K and power density of pump 2.57 mJ/cm^2 [138].

Theoretical studies of systems with competing degrees of freedom, as already discussed in Chapter 2, predict the formation of transient *hidden* orbital and structural phases that can be accessed only by optical stimulation in the

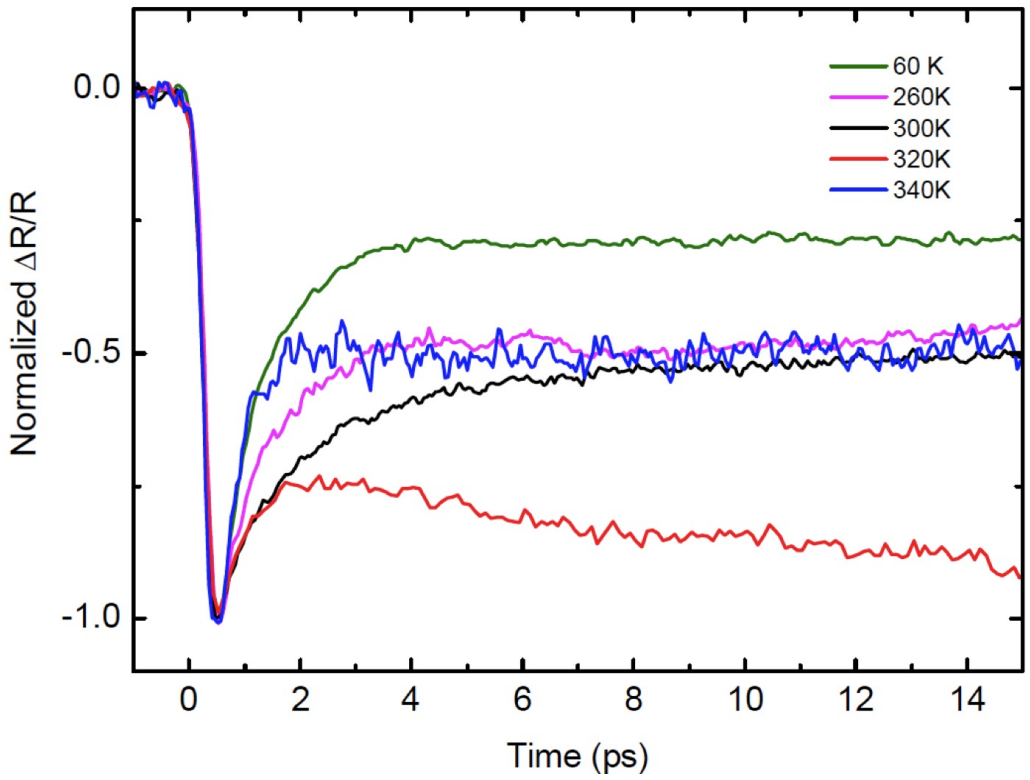


Figure 5.11: The temporal evolution of transient reflectivity at several temperatures representing different phases in PCMO [138].

dynamical processes of photoinduced phase transitions (PIPTs) [41, 150–152]. Recent studies have demonstrated that a new photoinduced state, which can be classified as a *hidden* insulating phase, emerges by relaxation of a precursor metallic state in $Nd_{0.5}Sr_{0.5}MnO_3$ NSMO [96]. In this work the authors reported the photoinduced change in the lattice structure of a charge and orbitally ordered NSMO thin film using picosecond time-resolved X-ray diffraction (XRD). The photoinduced state is structurally ordered, homogeneous, metastable and has crystallographic parameters different from any thermodynamically accessible state.
On the basis of these studies, we decided to carry out the following experiment, whose goal has been to optically photoinduce the CO-O transition in PCMO. Our collaborators performed some optical measurements of the transient reflectivity with 400 nm pump and 800 nm probe. They photoinduced the CO-O transition [138]. The metastable state, characterized by Δ in Fig.5.10, is last more than 200 ps, which is a time sufficiently long to be observed with the time resolution of our setup.

The dynamics of transient reflectivity ($\Delta R/R$) has been measured at several temperatures, as depicted in Fig.5.11.

An anomalous behavior appears conspicuously around T_{CO-O} of 320K marked by longer and a reverse trend of the second growth of transient reflectivity

which takes the system further away from the initial equilibrium state. On the basis of the dynamical information extracted from the above optical measurements, we carried out time-resolved XAS measurements at the O-K edge.

5.1.2.1 Experimental procedure

The measurements have been performed at the branch C of BACH beamline by means of the time-resolved XAS experimental apparatus, described in section 3.4.3. The PCMO sample has been placed in the UHV chamber. The voltage of the MCP detector was set at 1800 V in order to have high counting efficiency. The fluence on the sample was equal to 0.55 mJ/cm^2. Two different light polarizations have been used in order to explore the in plane and out of plane states.

5.1.2.2 Results and Discussion

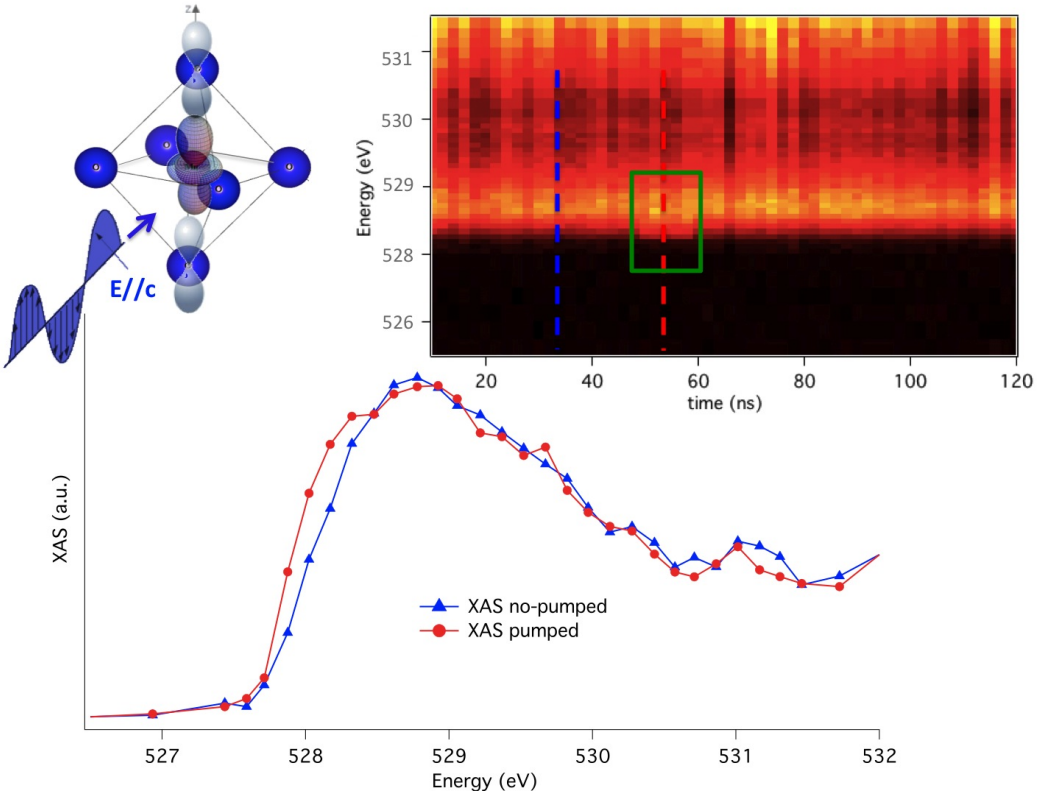


Figure 5.12: (Top) Intensity plots of O K TR-XAS spectra of PCMO for E‖c. The XAS spectra intensities are plotted versus the photon bunch arrival time and versus the x-ray photon energy. The green square indicate the region where the spectra present a change of the lineshape. (Bottom) O K TR-XAS spectra sliced from the intensity plot and taken at two different time delays with respect to the laser pulse: no pumped XAS (blue triangles) and pumped XAS (red circles).

I have studied the unoccupied DOS of the optically induced metastable state in PCMO by means of time resolved XAS, which offers a unique tool to

measure site and symmetry projected DOS of metastable states in matter. By means of vertical and horizontal light polarization the oxygen out of plane and in plane DOS have been probed, respectively.

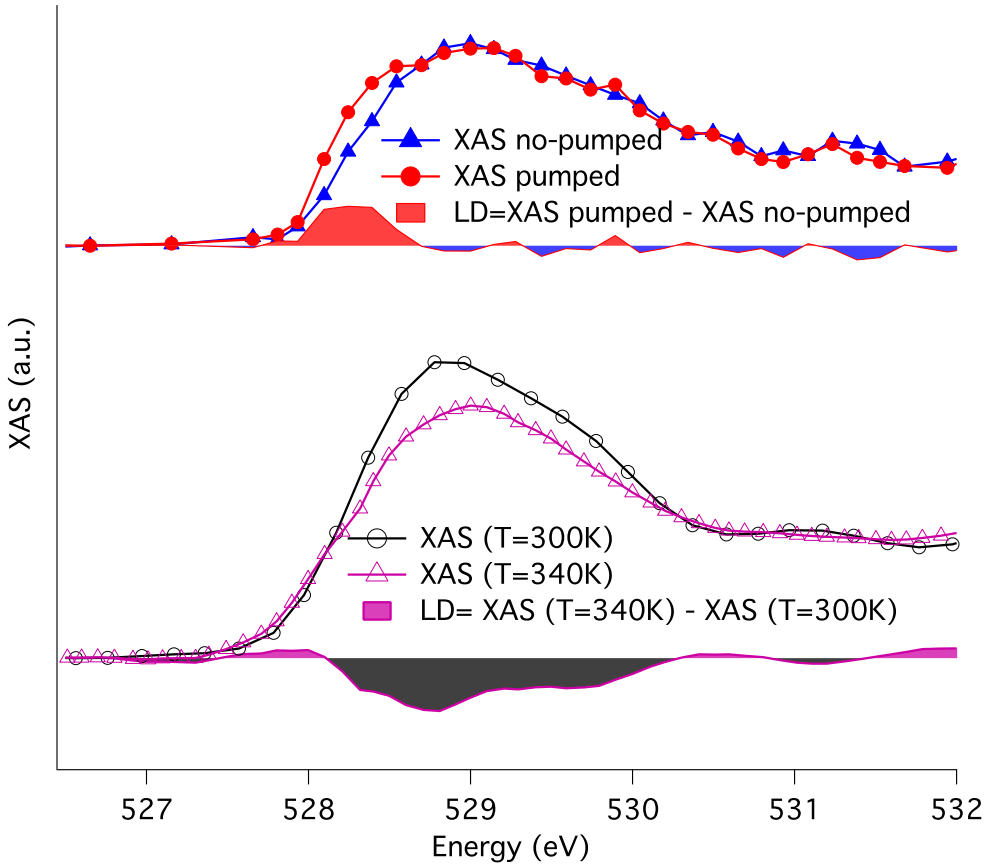


Figure 5.13: (Top) O K TR-XAS spectra taken at two different time delays with respect to the laser pulse: no pumped XAS (blue triangles) and pumped XAS (red circles) (see 5.12. The XLD is also reported (filled line). (Bottom) O K XAS spectra taken at T=300 K (black circles) and T=340K (pink triangles) (see Fig.5.5). The XLD is also reported (filled line).

O K edge out of plane states Fig.5.12 reports the intensity plots of O K TR-XAS spectra for E||c for a photon energy range between 526 eV and 532 eV and for time delays between 0 ns and 120 ns. The uniformity of the colors indicate that all the spectra are identical, except for the temporal region between 50 and 60 ns. In this interval the spectra present a change of the lineshape. This difference is made evident in the graph on the bottom of Fig.5.12, which reports the O K TR-XAS sliced from the intensity plots (on the top) and taken at a time t before and after the laser excitation. In Fig.5.13 the two TR-XAS spectra (reported in the previous picture) with the corresponding XLD are reported.

This dichroich signal is compared with the XLD extrapolated from the adiabatic XAS measurements reported in Fig.5.5. The time evolution of the XAS

lineshapes across the optically photoinduced CO-O transition results different respect to the adiabatic XAS measurements, demonstrating the existence of a photoinduced *hidden phase* in PCMO, whose nature is still unknown.

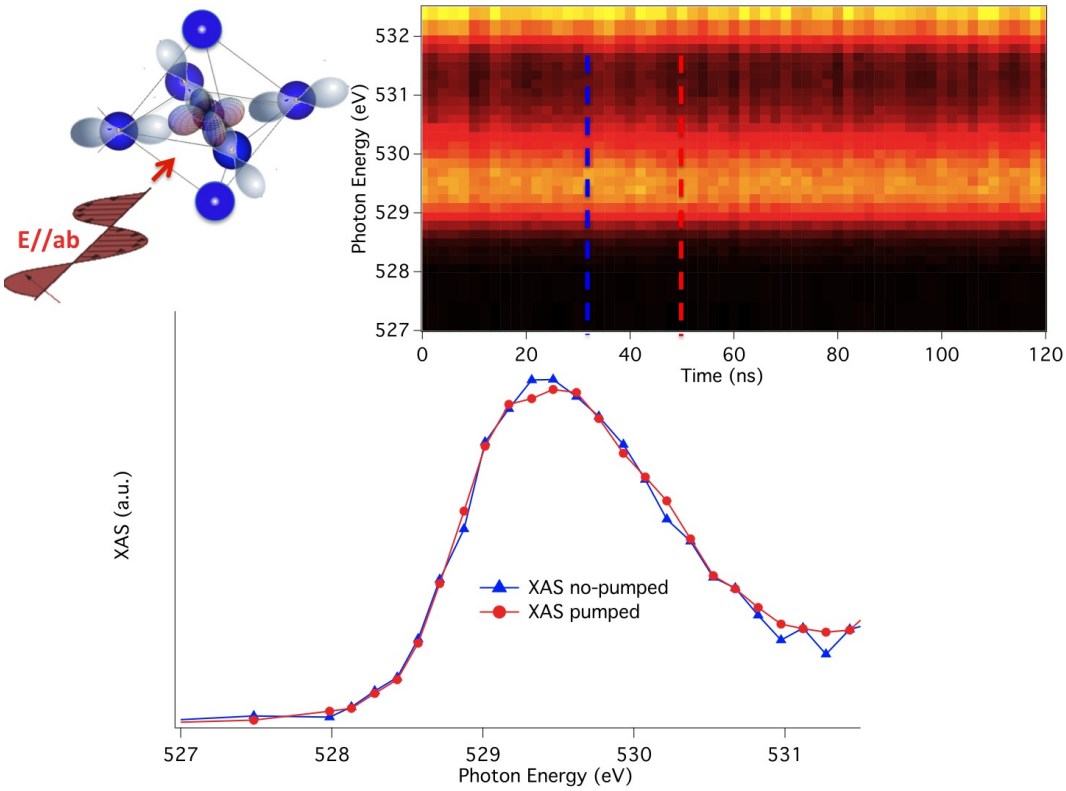


Figure 5.14: (Top) Intensity plots of O K TR-XAS spectra of PCMO for E‖ab. The XAS spectra intensities are plotted versus the photon bunch arrival time and versus the x-ray photon energy. (Bottom) O K TR-XAS spectra lineshapes sliced from the intensity plot and taken at two different time delays with respect to the laser pulse: no pumped XAS lineshape (blue triangles) and pumped XAS lineshape (red circles).

O K edge in plane states Fig.5.14 reports the intensity plots of O K TR-XAS spectra for E‖ab for a photon energy range between 527 eV and 532.5 eV and for time delays between 0 ns and 120 ns. The uniformity of the colors indicate that all the spectra are identical. Furthermore the O K TR-XAS lineshapes sliced from the intensity plot at two different time delays (before and after the laser excitation) are reported. It is evident that in this case, contrary to the out of plane of states, the edge does not change due to the laser excitation. This can be explained taking into account the fact that we are looking at higher energy states.

5.2 Orbital structure evolution in the layered $Sr_{n+1}Ru_nO_{3n+1}$ (n=1,2,3) by means of RXES

5.2.1 The Ruddlesden-Popper series of Sr Ruthenates

The physical properties of low dimensional layered TMOs are determined by the competition between the peculiar local atomic structure of the TMO-hedra and the electronic and magnetic freedom degrees. In this regard, TMOs have proved to be particularly fruitful, especially for those materials with the perovskite structure, where the special characteristics of transition-metal-oxygen orbital hybridization determine their properties. Ruddlesden-Popper Strontium Ruthenates ($Sr_{n+1}Ru_nO_{3n+1}$)(SRO) have emerged as an important family of perovskites because of the unexpected and unprecedented evolution from high-temperature isotropic ferromagnetism in $SrRuO_3$ to anisotropic ferro- or metamagnetic behavior of $Sr_4Ru_3O_{10}$ (n=3) dependent on the direction of the magnetic field, enhanced Pauli paramagnetism close to magnetic order of $Sr_3Ru_2O_7$ (n=2) and, finally, to low-temperature superconductivity in Sr_2RuO_4 (n=1) [4, 5].

Such fascinating phenomena are closely related to a complicated interplay between the crystal lattice, spin, charge, and orbital degrees of freedom, where crystal dimensionality and the special characteristics of metal-oxygen orbital hybridization play a crucial role. It is, however, not clear yet to which extent the dimensionality and the superconductivity are linked.

In the following, I will briefly review the physical properties of the three different members of the SRO family, sketched in Fig.5.15.

Sr_2RuO_4

Sr_2RuO_4 is the first member (n=1) of the Ruddlesden-Popper (R-P) family and it is also the most studied ruthenate, since the discovery of the superconductivity below $T_C \simeq 1.5$ K [5]. The crystal structure of this compound belongs to the I4/mmm body-centered tetragonal space-group symmetry, as sketched in Fig.5.15, with low temperature lattice parameters $a = b = 3.862$ Å and $c = 12.722$ Å. It does not present any phase transitions up to room temperature. This phase presents an unconventional nature of superconductivity with strong experimental evidences of a p-wave spin-triplet pairing[2] and a quasi-2D Fermi-liquid behavior in the *ab* plane, with highly anisotropic electrical conductivity (see Fig.5.16).

A key signature of the p-wave spin triplet pairing is the observation of a strong suppression of T_C by nonmagnetic impurities [158] and lattice defects [159]. A complete review of its physical properties can be found in [160].

[2]The nomenclature refers to the type of symmetry-breaking properties of the condensate, with respect to the gap function as the order parameter. Conventional superconductors can be described with the BCS theory, in which the Copper pairs are in s-wave.

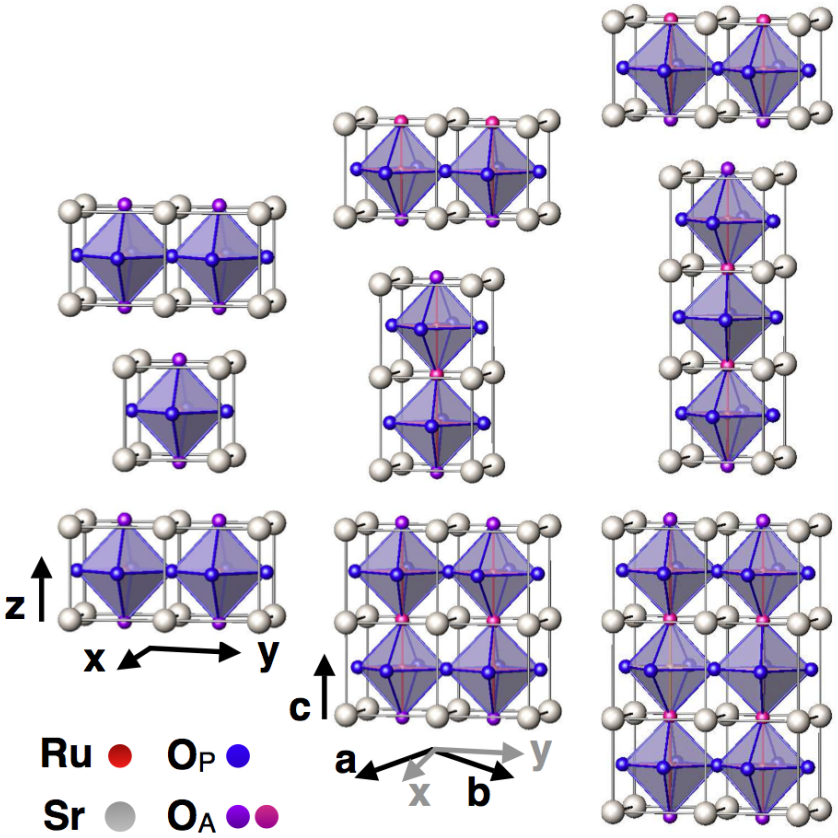


Figure 5.15: Left to right: crystal structure of Sr_2RuO_4, $Sr_3Ru_2O_7$, and $Sr_4Ru_3O_{10}$[153, 154]. The tetragonal (Sr_2RuO_4) and pseudo-tetragonal [155] ($Sr_3Ru_2O_7$, and $Sr_4Ru_3O_{10}$) axes are indicated as x, y, z.

$Sr_3Ru_2O_7$

$Sr_3Ru_2O_7$ is the n=2 member of the R-P type ruthenate series. The RuO_6 octahedra inside the unit cell are rotated by $\sim 7\,^\circ$ along the c axis (see Fig.5.17), due to the double layer structure, which cause compressions in the equatorial plane and cooperative bending of the oxygen bond, shared by the octahedra [157, 161].

Hence the final structure is a distorted rock-salt, belonging to the *Bbcb* space group, with $a \simeq b = 3.8872$ Åand $c = 20.732$ Å. $Sr_3Ru_2O_7$ is a quasi-2D metal, with $\rho_c/\rho_{ab} \simeq 300$ at room temperature, reflecting the layered character of its crystal structure (see Fig.5.16). A remarkable decrease of ρ_c is present below 50 K and a Fermi-liquid state is present up to 10 K, as outlined in the inset. This behavior is caused by the competition in the ground state between a ferromagnetic (FM) ordering and antiferromagnetic (AFM) correlation effects [163, 164]. $Sr_3Ru_2O_7$ is indeed an enhanced paramagnet (or nearly ferromagnet), i.e. it does not present neither a long range FM nor an AFM ordering [157, 165, 166]. In particular, Capogna shows that the change in temperature of magnetic fluctuations is reflected in macroscopic properties,

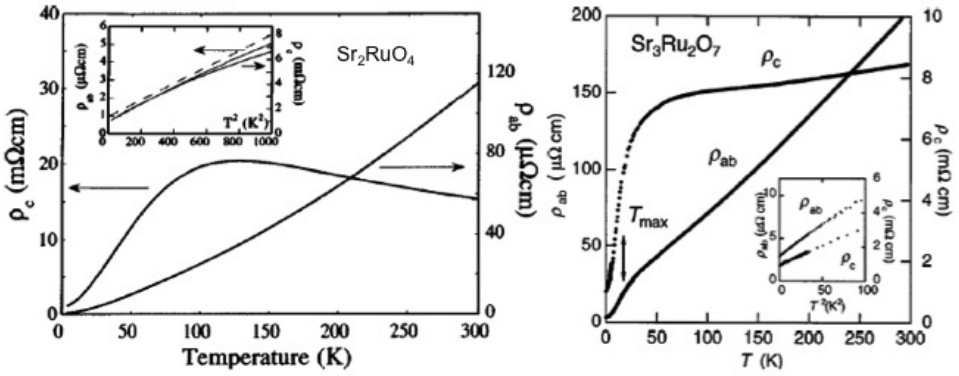


Figure 5.16: On the left: anisotropic resistivity in Sr_2RuO_4 [156]. On the right: the electrical resistivity of $Sr_3Ru_2O_7$ [157]. In both the insets, the low-temperature T^2 dependence of resistivity expected for a Fermi liquid.

such as the magnetic susceptibility [166]. In Fig.5.18(a) the behavior of the resistivity is sketched as a function of temperature and on applied magnetic field H. The transition occurring at $\sim$ 15 K and zero field is accompanied by a change in the resistivity behavior from Fermi-liquid to a more complicated one. The effect of increasing H drives the transition to lower temperatures, eventually terminated in a quantum critical point [167, 168], as sketched in the phase diagram in Fig.5.18(b).

$Sr_4Ru_3O_{10}$

The triple-layer $Sr_4Ru_3O_{10}$ is a structurally distorted ferromagnet, with a Curie temperature of T_C = 105 K. Distortions take place in the *Ru-O-Ru* angle of planar octahedra, as sketched in Fig.5.19.

As the other compounds, resistivity exhibits a Fermi liquid behavior up to 15 K, with a strong, but less marked anisotropy (Fig.5.20(b)). Magnetization measurements versus applied magnetic field show a FM ordering along the c axis and a sharp metamagnetic transition in the ab plane up to 50 K (see Fig.5.21).

First measurements as a function of temperature show that the FM transition at T_C is followed by an additional magnetic transition at $T_m \simeq$ 50 K,

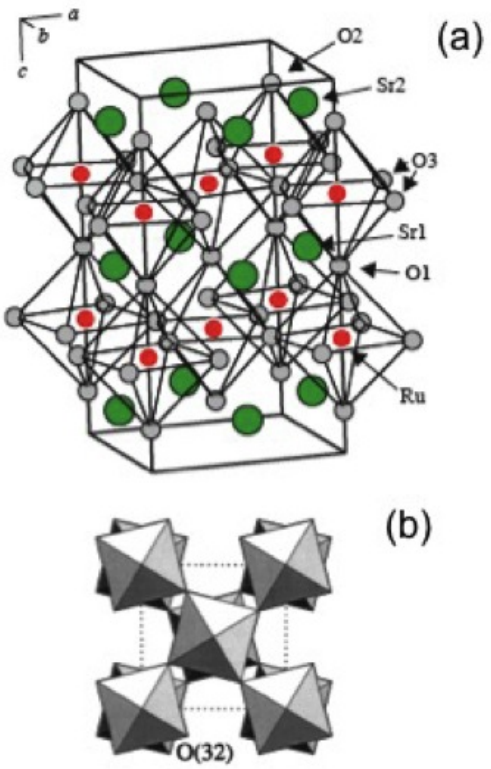


Figure 5.17: Side (a) and top (b) view of the simplified distorted structure of $Sr_3Ru_2O_7$ with unit cell containing one double $Ru-O$ layer (from Ref.[162] and [161], respectively).

that is visible also in the out-of-plane resistivity (see Fig.5.20). Recent neutron scattering measurements [171] show that the magnetic structure must follows the same symmetry of the crystal structure and the spin's easy axes lie in the *ab* plane. The magnetic behavior along the *ab* plane is described in the phase diagram of Fig.5.22.

5.2.2 Aim of this study

Following the wide experimental effort on cuprates and cobaltates, the study of ruthenates focused on the RuO_2 layers motivated by the widely accepted notion that RuO_2 planes are responsible for the physics of these compounds. Accordingly, understanding the low energy, i.e. near the Fermi level (E_F), electronic structure of normal RuO_2 planes may aid in determining the electronic and structural contributions to the mechanisms responsible for the rich electronic and magnetic phase diagram of ruthenates. Although the charge carriers in these SRO family have mainly Ru *4d* character [47], via hybridization electrons delocalize through O *2p* orbitals, so it is important to obtain information on the induced-electron/hole distribution over inequivalent O atoms. Such an identification helps to draw the picture on the hole distribution over different O atoms and can clarify the role of the orbital topology on the electronic and physics

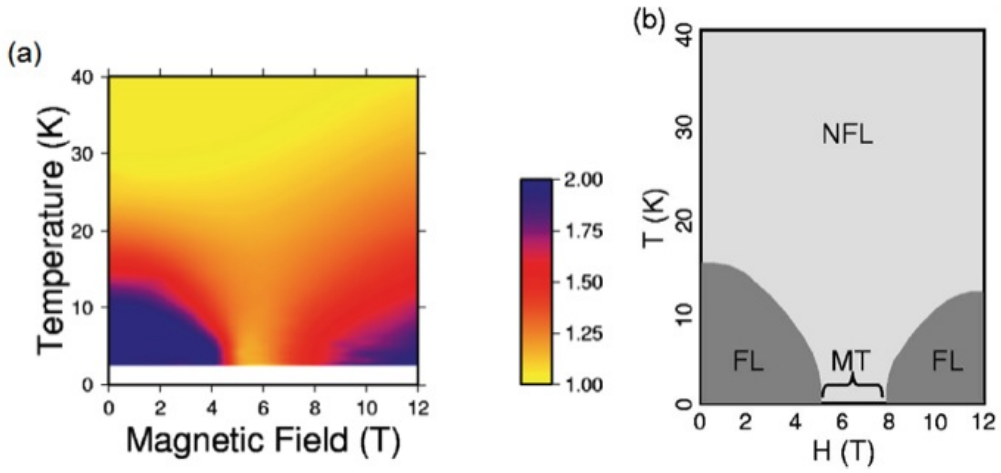


Figure 5.18: a) The evolution of the temperature dependence of the resistivity of $Sr_3Ru_2O_7$ as a function of temperature, with B//I//ab, where I is the current, for different applied magnetic field. The colors represent the value of the coefficient for the proportionality:formula [169]. b): phase diagram showing the temperature and magnetic field dependent crossover between a Fermi-liquid (FL) and non-Fermi liquid (NFL) behavior [165], separated by a low temperature metamagnetic (MT) transition range.

of the layered ruthenates. An orbital interpretation of the O *1s* absorption spectra requires a combined approach of calculation and experimental techniques capable of selectively probing the *p*-DOS contributions of O atoms at different crystal sites. Very recently results of a comprehensive study by means of XANES (x-ray absorption near edge structure) at the O K edge have been published [173]. Besides XANES, the methods of RXES [174–177] provides an element and site specific tool of unique precision for the investigation of the spatial distribution of the electron density. While polarization-dependent x-ray absorption spectroscopy probes symmetry of unoccupied states related to the crystal axes, tunable excitation x-ray fluorescence technique provides information about projections of these states onto inequivalent sites.

RXES spectra, which are obtained by tuning the excitation energy of the incoming photons across a corresponding XAS spectrum often comprise two different components. On one hand the so-called resonant inelastic x-ray scattering (RIXS) features often reflect the local occupied electronic structure as charge transfer excitations in correlated electron systems. In RIXS, an incident photon is inelastically scattered and a photon of lower energy is detected with

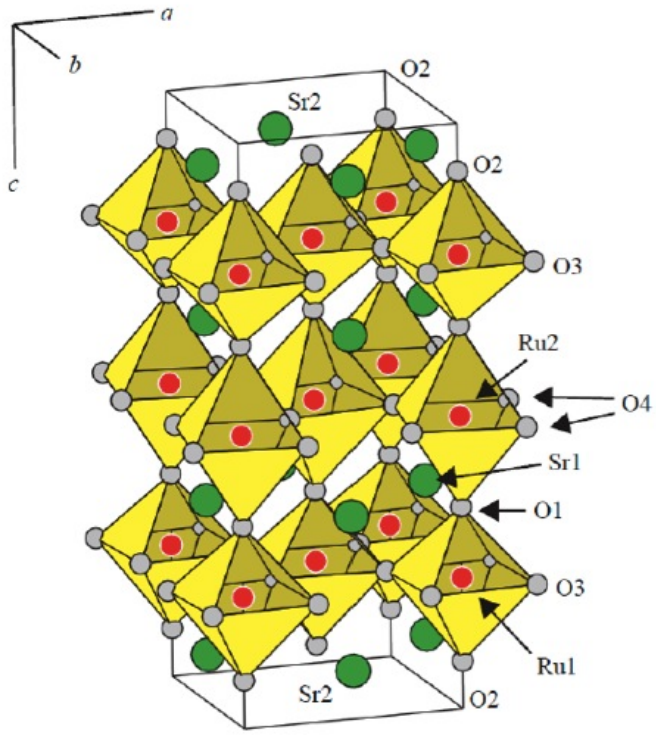


Figure 5.19: Simplified distorted structure of $Sr_4Ru_3O_{10}$ [162]. In the outer layers octahedra are rotated along the c axis of $\sim 5.6°$, in the central layers of $\sim 5.6°$ in the opposite direction. The symmetry group is P4/mbm.

respect to that of elastically scattered photons. On the other hand ordinary fluorescence is also detected at constant photon energies. This process is often normal x-ray emission spectroscopy (NXES) and represents to a large extent the partial densities of states (p-DOS).

Owing to the dipole selection rule, the oxygen K-edge threshold and the K_α x-ray XES are considered as projections of the unoccupied and occupied *2p* *p*-DOS, respectively [176, 178].

Although numerous studies have been reported on the structural and magnetic properties of some members of the SRO family, the evolution of the occupied and unoccupied electronic structures have not been investigated in detail.

In the present case we study the site specific contributions of the two inequivalent in plane (O_p) and out of plane (O_a) oxygen atoms of the RuO_2 octahedra to the O K RXES spectra of the highly anisotropic systems SRO in dependence of the polarization direction ($\vec{E}$) and the excitation energy across the selectively excited O K absorption edge.

Our results provide new insight into the n dependence of the apical and in-plane O $2p$ DOS across E_F for this family, which we discuss based on $ab-initio$ calculation. Taken in conjunction with the previous work on XAS measure-

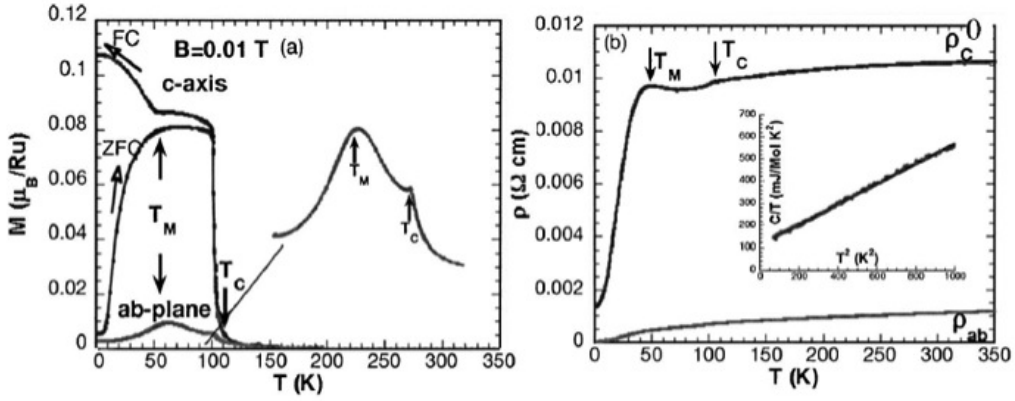


Figure 5.20: a) Magnetization as a function of temperature of $Sr_4Ru_3O_{10}$. In the inset the zoomed behavior for the *ab* plane. (b) Resistivity as a function of temperature. Both are from Ref.[170].

ments on SRO [173], the results presented in this work establish a complete experimental and theoretical picture of the nature of the occupied and unoccupied oxygen *2p* projected DOS of the SRO family.

5.2.3 Experimental procedure

High quality SRO single crystals were synthesized by flux-feeding floating zone technique, with Ru self-flux [179–182]. All sample surfaces were prepared *in-situ* by cleaving in ultra high vacuum conditions (pressure was 10^{-9} mbar during the measurements).

The experimental work was carried out at BACH [70, 71]. The measurements were performed in the bulk sensitive fluorescence yield mode with an energy resolution of 0.15 eV for O 1*s* XAS. The energy scale of the XES was calibrated using the Cu K emission lines of pure copper metal. On- and off-resonance O K_α XES measurements were acquired with a grating fluorescence spectrometer [183] mounted in the horizontal plane at 60° from the incident photon beam and recorded in the second order of diffraction. For this set of measurements the combined resolving power Q of the beamline and the spectrometer monochromator was around 800 at the second diffraction order.

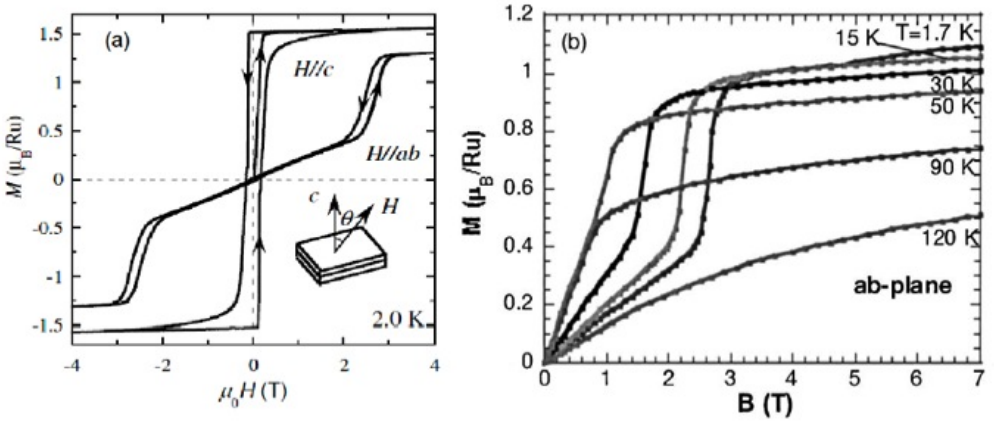


Figure 5.21: a) Isothermal magnetization as a function of B [171]. b) Temperature dependence of the basal plane metamagnetic transition [170].

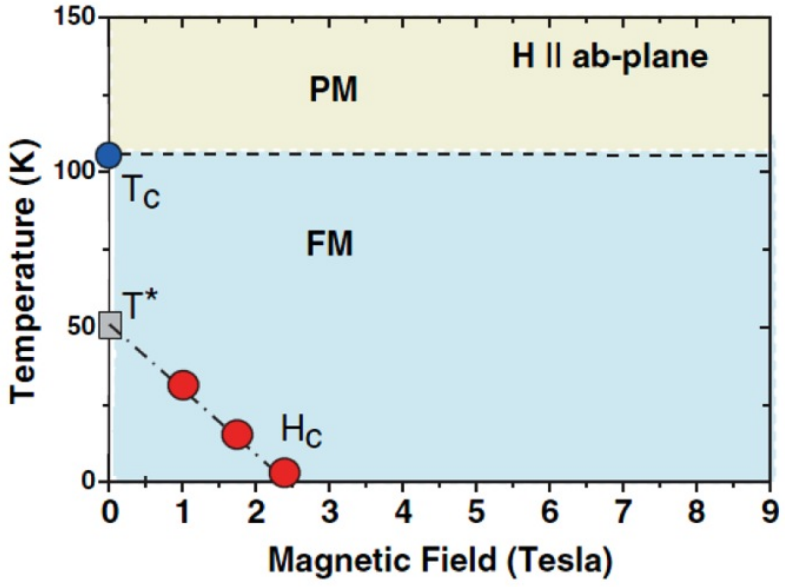


Figure 5.22: The phase diagram of $Sr_4Ru_3O_{10}$, with the still unclear magnetic transition H_C, leading to a FM behavior up to the Curie temperature T_C [172].

The O *1s* XAS and XES spectra for the three systems were acquired with fixed incident $\theta_{inc} = 60°$ angle and photon polarization varying from horizontal ($\vec{E} \wedge c = 60° \rightarrow \vec{E} \parallel c$) to vertical ($\vec{E} \parallel ab$), as shown in figure 5.23, permitting a precise study of the XAS/XES polarization dependence without introducing geometrical factors due to different optical paths in the process and in order to get rid of self-absorption effects. Due to the dipole selection rules, the in-

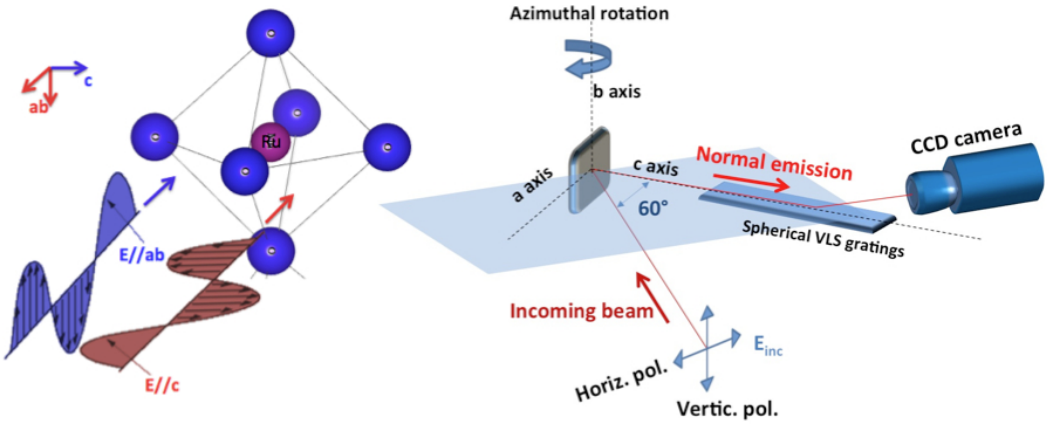


Figure 5.23: Scheme of the light electric field components with respect to the in-plane and out-of-plane crystal orientation (c and ab) and the Ru-O octahedra of the SRO single crystals. The vertical light ($E \parallel c$) polarization (blue) probes the out-of-plane states and the horizontal ($E \parallel ab$) one (red) probes the in-plane states. Right: scattering geometry of the RXES measurements.

plane field induces O $1s \rightarrow$ O $2p_{xy}$ excitations only, while the out-of-plane field induces exclusively O $1s \rightarrow$ O $2p_z$ transitions. Thus, by changing the $\vec{E}$ from horizontal to vertical, states with different orbital symmetries are probed. The propagation and polarization vectors of the incoming radiation are depicted in Fig.5.23. The data were corrected for the energy-dependent incident photon flux and normalized to tabulated cross sections in an energy range about 40 eV above the O $1s$ threshold energy.

The excitations for the XES measurements were determined from the O $1s$ x-ray absorption spectroscopy measurements (using total electron yield mode); the chosen energies correspond to the location of the main XAS features and an energy well above the K resonance.

5.2.4 Results and discussion

5.2.4.1 O *1s* edge spectra of SRO (n=1,2,3)

Fig.5.24 shows the polarization dependent O K-edge XANES spectra in the photon energy range 528-536 eV for vertical ($\vec{E} \parallel ab$) and horizontal ($\vec{E} \parallel c$) polarizations collected for all the SRO (n=1,2,3) compounds. Fig.5.24 presents the O K-edge XES spectrum recorded with excitation energies above the absorption threshold and the O K-edge XAS spectra all plotted on a common

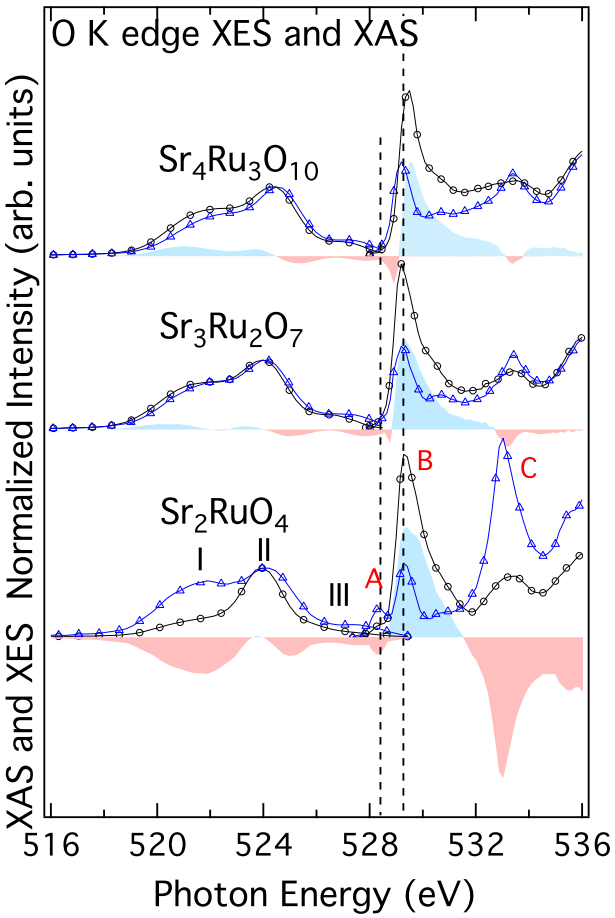


Figure 5.24: Normalized O 1*s* polarization dependent XAS and XES spectra, measured with the electric field $\vec{E}$ along the *c*-axis (black curve) and with $\vec{E}$ in the *ab*-plane (blue curve) of the $Sr_{n+1}Ru_nO_{3n+1}$ crystals. The XES spectra are taken on off-resonance conditions with photon energy 550 eV. The x-ray emission spectra are aligned in energy relative to the E_F. The XES (XAS) spectra reflect the O *2p* occupied (unoccupied) oxygen partial density of states.

binding energy scale. The corresponding linear dichroic (LD) spectra, defined as the difference between the out-of-plane and the in-plane polarizations, i.e. LD_{XAS}=$XAS_{\vec{E}\|c}$-$XAS_{\vec{E}\|ab}$ and LD_{XES}=$XES_{\vec{E}\|c}$-$XES_{\vec{E}\|ab}$ are also reported. The latter will be discussed in the following paragraph. All the XAS spectra display three prominent spectral feature (A, B and C) and a remarkable linear dichroism attributed to the many-fold O_{2p}-Ru_{4d} hybridization, which are extensively discussed in reference [173]. In brief, there are two main absorption regions: a low-energy one that extends from E_0 to E_1 = 530 eV and a high-energy one from E_1 to E_2 = 536 eV. In the low-energy region, Sr_2RuO_4 exhibits a double-peak structure (A and B features), which can be ascribed [184] to the energy difference between apical (O_A) and planar (O_P) oxygen 1s core levels. The double peak turns into a single peak with a shoulder in $Sr_3Ru_2O_7$ and $Sr_4Ru_3O_{10}$. The energy separation between peaks B and C is

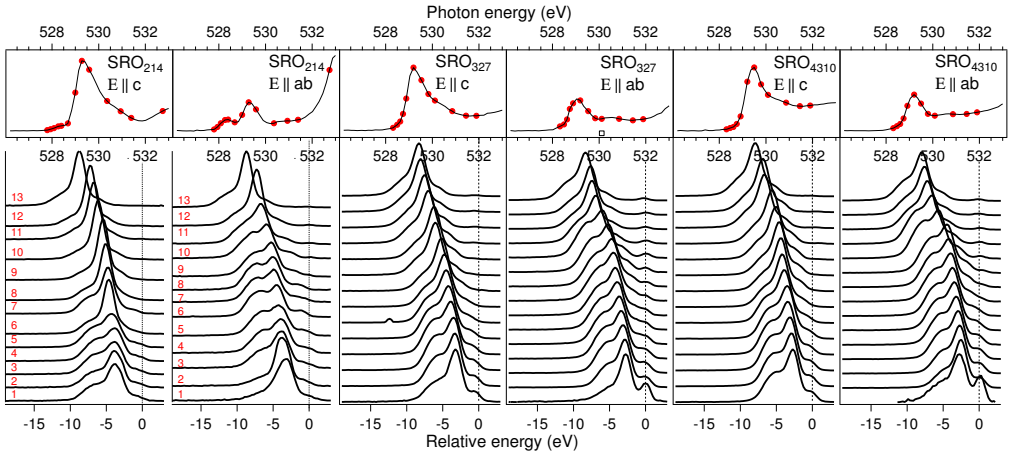


Figure 5.25: Top panels: O K-edge x-ray absorption spectra of SRO (n=1,2,3) for two polarizations ($\vec{E} \parallel c$ and $\vec{E} \parallel ab$). Dots in the O K-edge absorption spectra indicate the exitation energies at which the resonant x-ray emission spectra were recorded. Bottom panels: O K_α ($2p \rightarrow 1s$) RXES spectra obtained for SRO (n=1,2,3) at 300 K for several excitation energies across the O K edge (top panels) for $\vec{E} \parallel c$ and $\vec{E} \parallel ab$. The resonant x-ray emission spectra are plotted from bottom to top with increasing energy of incident photons. The spectra consist of elastically scattered light, conserving the photon energy, and inelastically scattered light. The energy positions of the XES spectra are aligned to the elastic peak (dotted line) and plotted versus the energy loss. Each emission spectrum is normalized according to its maximum value.

about 4 eV in Sr_2RuO_4 and slightly increases to n = 2,3, mainly because the feature C drifts to higher energy. The spectral weight between B and C increases as n grows. In all systems, a dramatic spectral weight transfer from the high- to the low-energy region is observed by changing $\vec{E}$ from $\vec{E} \parallel c$ to $\vec{E} \parallel ab$. Finally, for $\vec{E} \parallel ab$, peak C is considerably reduced for the bilayered and trilayered materials. Finally, the spectral behavior of the A component as a function of the polarization direction and across the RP series strongly reflects the overall trend of the RuO_2 local structure. The energy position of absorption edge for the in-plane component is nearly identical for the three samples whereas a chemical shift is observed for the out-of-plane component of the $Sr_4Ru_3O_{10}$.

Because of the different orbital geometry and the difference in the absorption energy for the O_P and O_A (different binding energies), the measured LD XAS signals exhibit features that support the above assignments. The calculations reported in Fig.5.26 corroborate the observed linear dichroism by revealing that the Ru t_{2g} states and e_g states extend for 5 eV above the E_F. The main resonance at about 529 eV corresponds to the apical O^a_{2p}-Ru_{4d} hybridization. A second spectral feature is present at 533 eV corresponding to the planar O^p_{2p}-Ru_{4d} hybridized states. Ergo, the different p-DOS distributions of the O $2p_z$ (parallel to the c-axis) and O $2p_{xy}$ DOS (parallel to the ab-plane) explain the dichroic effect observed in the O K XAS spectra.

Our results (see reference [173] for an in-depth discussion) show that at

low energy the most significant difference among the three systems is the rearrangement of t_{2g} orbital occupations. We find that this rearrangement stems from the interplay between the dimensionality and the t_{2g} crystal field and it is associated with a change in the position of the E_F in the density of states (DOS).

5.2.4.2 RXES on the O *K* edge

O *2p-1s* RXES spectra recorded at two polarizations across the near edge of the O K threshold are displayed in Fig.5.25 (bottom row panels). The top row panels show the corresponding XAS spectra, while the excitation photon energies are indicated by dots.

The XES spectra have been normalized and plotted versus relative energy in a stacked fashion for comparison across all of the excitation energies. The vertical offset of the RXES spectra is scaled to the incident energy axis of the XAS spectra. Relative energy is defined as the difference between the incident photon (E_{in}) and the emitted photon energies. The change in the excitation energy can be easily monitored due to the presence of the peak from the elastically scattered radiation in all the spectra (see vertical dotted lines in figure 5.25). Finally, the elastic peak energy position is set to zero.

For all the excitation energies, (see Fig.5.24) the spectra are dominated by a strong central peak labeled II in the figure with weaker features I and III to high and low photon energy, respectively.

This spectral profile is consistent with the O $K\alpha$ XES spectra measured on Sr_2RuO_4 as reported elsewhere [185]. Due to the different $4d_{Ru}$-$2p(O)$ hybridization the valence band splits into apical and planar oxygen contributions. Indeed, the measured valence band exhibits a two sub-band structure.

This spectral shape agrees with the dual band XES character predicted by the calculated partial density of states of Ru and O as shown in Fig.5.26 and discussed below [173].

Interestingly though, the measured off-resonance XES spectra exhibit a not negligible linear dichroism LD_{XES} upon change of the x-ray polarization. Correspondingly, the off-resonance dichroic features of the LD_{XES} profiles reflect either the in-plane or the out-of-plane nature of the associated orbital states. Consistently, the LD_{XES} profiles match with the LD_{XAS} line profile in indicating that the electronic structure crossing the E_F has an in-plane character, as is confirmed by the calculated p-DOS shown in Fig.5.26 and discussed in the following.

Particularly intriguing is the different profile variation of the resonant XES lineshape at the two polarizations. For $\vec{E} \parallel c$ and $\vec{E} \parallel ab$ and for all the excitation energies, peak II results to be non resonant for all the measured compounds. This can be ascribed to the prevalent Sr - O *2p* hybridized orbital character of this spectral energy region as consistently supported by the calculated symmetry projected Sr and O density of states shown in Fig.5.26 panel *c*, *d* and *e*. In more detail, the simulated site resolved XES line profile

Table 5.2: Energy ranges (e.r.) of the resonant intensity I_I for the two polarizations and for all the samples. The energy difference ΔE is also reported.

SRO	e.r. $_{\vec{E}\|c}$ (eV) (ΔE (eV))	e.r. $_{\vec{E}\|ab}$ (eV) (ΔE (eV))
214	528.9 – 529.5 (0.6)	529 – 531.8 (2.8)
327	529.5 – 530.6 (1.1)	529.6 – 533.5 (3.9)
4310	529.5 – 531.4 (1.9)	530 – 534 (4)

(5.26, *b*) allows us to assign peak II to the core-hole recombination of the apical oxygens whose *2p*$_z$ orbital hybridizes with the Sr orbitals. On the other hand, peak I displays a remarkable different resonant behavior for $\vec{E} \parallel c$ and $\vec{E} \parallel ab$ and as a function of n. The corresponding profile variations in the hybridization shoulder I, with respect to the incident energy, reflect the interaction of the atomic orbitals of Ru with the symmetry combinations of the surrounding oxygen hybrid orbitals. Consistently, the excitation energy dependence can be associated with site specific contributions from the different oxygen sites in $Sr_{n+1}Ru_nO_{3n+1}$, namely the in-plane, or equatorial O_p site, and the out-of-plane, or apical O_a site. Similar effects have been observed in previous works dealing with other highly anisotropic materials as Sr_2RuO_4 or NaV_2O_5 [185].

The calculated XES spectra and the corresponding O *2p* and Ru *4d* projected DOS corroborate these observations by revealing that peak I can be ascribed to the O_P $2p_z$- Ru $4d_{xz}$ (panel *f* and *c* of Fig.5.26, α yellow line).

The amplitudes of the three spectral features ($I_{I,II,III}$) as a function of the excitation photon energies have been calculated by decomposing the resonant XES spectra in a linear combination of three Lorentzian profiles centered at 1.3, 4.6 and 7 eV below the E_F as shown in figure 5.26, panel *a*. In Fig.5.27, the intensity (I_I) of the resonant peak I normalized with respect to the intensity of the non-resonant peak II (I_{II}) for the two polarizations and for all the measured compounds, are plotted as a function of the excitation photon energies (the resonant energy ranges reported in table 5.2). Also included in Fig.5.27 are the out-of-plane/in-plane XAS LDs for direct comparison.

The I_I/I_{II} profiles exhibit remarkable in-plane/out-of-plane anisotropies that are ascribed to the anisotropic orbital topology of the O *2p* states for the non equivalent planar/apical O sites. For $\vec{E} \parallel c$, I_I/I_{II} displays a resonant behavior peaked at 529 eV for the SRO_{214} compound (530 eV for SRO_{327} and SRO_{4310}). On the other hand, for $\vec{E} \parallel ab$, I_I/I_{II} displays a resonant regime broader in energy than the previous case. Interestingly, the two resonant regimes partially overlap at low photon excitation energies. Moreover, the energy widths of the observed resonant regimes (reported in table 5.2 for the two polarizations and for the three compounds) increases with the number of layers n, while an abrupt energy shift is observed in passing from $n = 1$ to $n = 2, 3$.

Considering that the Ru $4d_{xz,yz}$ orbitals mostly hybridize with O_A $2p_{xy}$ and O_P $2p_z$ respectively (see Ru *4d* and O *2p* *p*-DOS profiles reported in Fig.5.27,

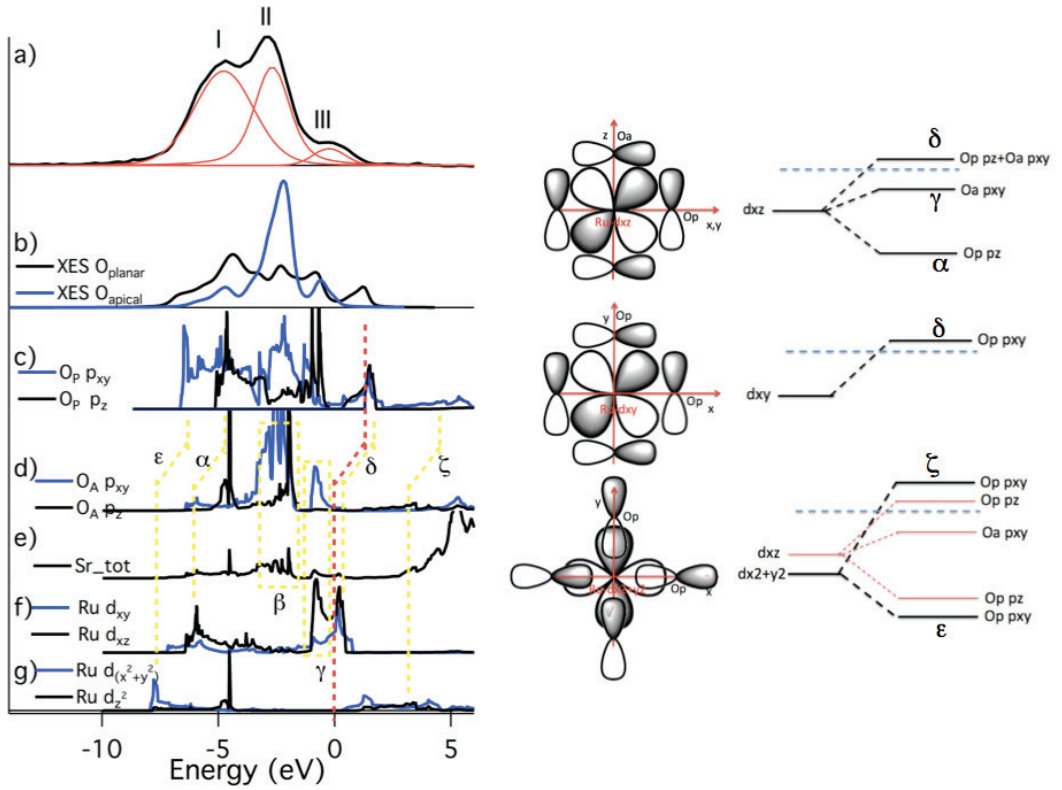


Figure 5.26: a) Resonantly excited O K_α x-ray fluorescence spectrum (black line) of Sr_2RuO_4 recorded at an excitation energy of 529 eV. Each measured XES spectrum is decomposed into three spectral components (I, II and III, red curves) with various two-hole final states (see text) using a set of Lorentzian lines. The sum and the band-like components are shown; b) Site resolved O 2p-XES spectra calculated for Sr_2RuO_4 and broadened for instrumental resolution $\Delta E = 0.3$ [110]; c) and d): O_A and O_P $2p$ density of states distribution in the valence band of Sr_2RuO_4 taken from local-density approximation band-structure calculations of Sr_2RuO_4[173]. The energy scale of the planar O 2p-DOS is shifted by 1.3 eV to account for the O planar/apical chemical shift; panels *e*, *f* and *g*: Sr $3d$ and Ru $4d$ density of states distribution in the valence band of Sr_2RuO_4 [173]; vertical dashed yellow line and rectangles (α, β, γ, δ, ϵ, ζ) indicate overlapping energy regions between hybridized Ru *4d* (Sr *3d*) orbitals and O *2p* orbitals. Right panel: schematic representation of the orbital topology of the hybridized Ru-4d O-2p orbitals and the corresponding electronic energy levels.

panel *d*), while the Ru d_{xy} and $d_{x^2-y^2}$ orbitals hybridizes with O_P $2p_{xy}$, thus for $E_{\|ab}$, I_I reflects the overall width and the energy range of the O_A p_{xy}-Ru $d_{xz,yz}$ and of the O_P p_{xy}-Ru $d_{x^2-y^2}$ unoccupied band.

On the other hand, for $E\| c$, I_I displays a resonant behavior in the 0-0.5 eV energy range above the E_F (see table 5.2, first column, for the corresponding excitation photon energies) where no hybridization is found between the out-of-plane (p_z) orbitals and the Ru *4d* states as shown in Fig.5.27 panel *e*.

The I_I profile thus indicates that intrinsic $2p_z$ holes exists on the apical oxygens, which are attributed to the Sr d_{z^2} - O_A $2p_z$ hybridization. The associated Sr-*d* O-$2p$ states near the E_F is in contrast with the common assumption

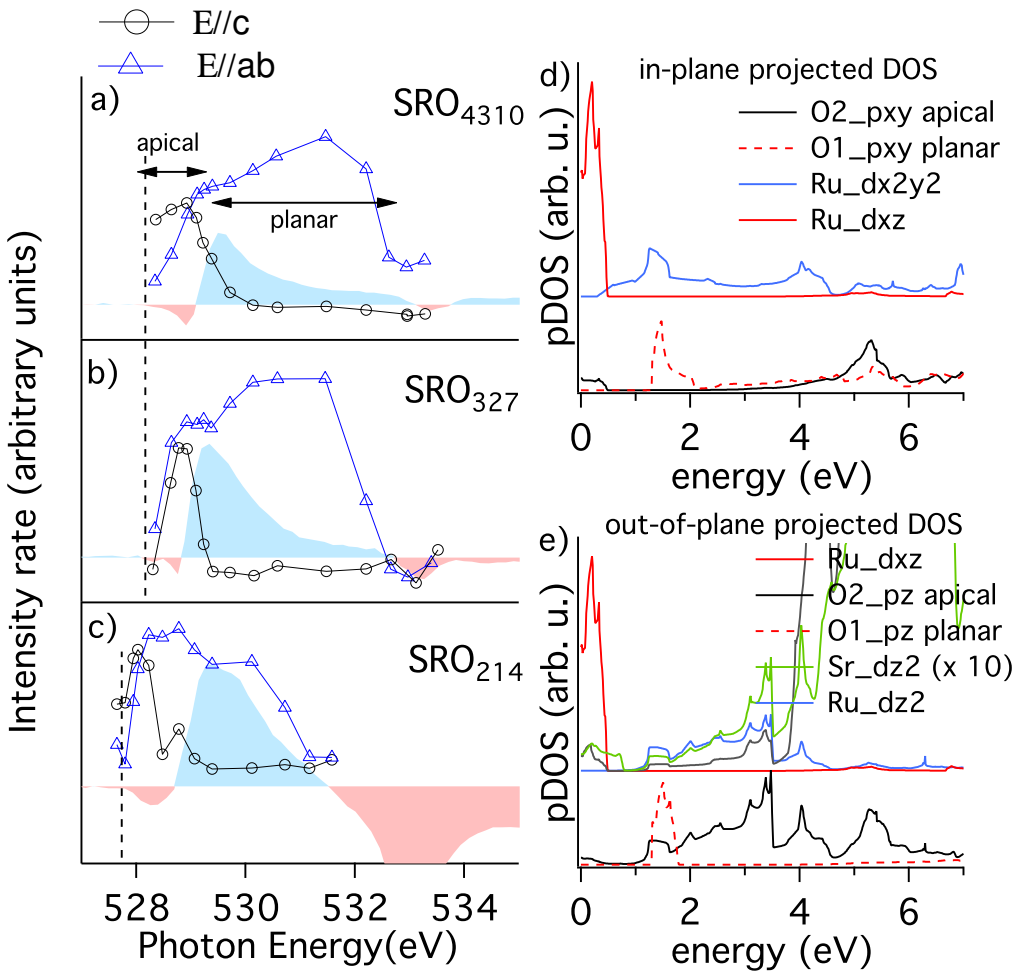


Figure 5.27: *a*, *b* and *c* panels: the intensity (I_I) of the resonant peak I normalized with respect to the intensity of the non-resonant peak II (I_{II}) for the two polarizations and as a function of the excitation photon energies ($\vec{E} \parallel c$ (black empty dots) and $\vec{E} \parallel ab$ (blue empty triangles)) for the three SRO compounds; the arrows in panel *a* indicate the energy ranges of the *2p* states of the apical and planar oxygens; the vertical dashed lines in panel *a*, *b* and *c* indicate the E_F. Filled curves: out-of-plane/in-plane x-ray absorption linear dichroism (as in figure 5.25); *d* and *e* panels: O *2p*, Ru *4d* and Sr *d* partial density of states projected along in-plane/out-of-plane directions.

of a fully Ru-4*d* O-2*p* ground state at the E_F.

This can potentially have important consequences for the microscopic understanding of the low temperature behavior of the system. This assignment is confirmed by comparing the latter profile with respect to the XLD lineshapes displayed in Fig.5.27. The observed dichroism reflects the anisotropy in the orbital topology of the electronic ground state: a O_A character in the 0-0.5 eV energy range and a O_P orbital character between 1 and 5 eV.

5.2.5 Conclusions

In conclusion, by combining soft x-ray spectroscopic techniques and *ab-initio* many body calculations, we have investigated the orbital topology and electronic structure of the occupied and unoccupied electronic states near the E_F of the anisotropic $Sr_{n+1}Ru_nO_{3n+1(n=1,2,3)}$ series leading to a number of results. By measuring the polarization resolved XAS and resonant XES spectra at the O K edge along the *c*-axis and the *ab*-plane of the SRO single crystals, we have disentangled the site specific p-DOS of the $2p$ orbitals of each inequivalent O ion. In addition, we have demonstrated explicitly the effects of the number n of Ru-O layers on the O sites, specifically the role of the apical O ion in determining the occupied and unoccupied low energy structure of the $Sr_{n+1}Ru_nO_{3n+1(n=1,2,3)}$ compounds. Finally we have found that Sr $3d$ bands are crucial to understand the resonant dependence of the XES spectra on the polarization direction. Correspondingly, and contrary to common assumption, we have shown that Sr *3d* orbitals participate to the electronic structure across the E_F level through the direct hybridization with the *2p* orbitals of the apical oxygens.

Chapter 6

Conclusions

This thesis work is focused on two case-study systems, both exhibiting important properties intimately related to a complex interplay among the crystal lattice, spin, charge and orbital degrees of freedom, and where the crystal dimensionality plays a crucial role.
The first compound that has been investigated is the single layered half-doped $Pr_{0.5}Ca_{1.5}MnO_4$. Temperature dependence measurements by XAS linear dichroism (XLD) have been performed at the O-K and Mn-L_3 thresholds in order to elucidate the role of Mn $3d$ - O $2p$ orbital topology. The experimental data, supported by ab-initio LDA+U, shed light on the charge redistribution and p-DOS changes at the charge-orbital ordering (CO-O) and antiferromagnetic (AFM) transitions. The results obtained show that the competitive interplay between the local atomic distortion, necessary for accomodating the CO-O, and the charge dynamics of the hopping mechanism regulates the orbital state of the charge carriers.
Furthermore, on the basis of theoretical studies, predicting the formation of transient hidden orbital and structural phases by optical stimulation, the unoccupied DOS of the optically induced metastable state in PCMO have been investigated by means of time resolved XAS. This experiment offers a unique tool to measure site and symmetry projected DOS of metastable states in matter. The time evolution of the XAS lineshapes across the optically photoinduced CO-O transition results different respect to the adiabatic XAS measurements, suggesting the existence of a photoinduced hidden phase in PCMO, whose nature is still debated.
For the layered $Sr_{n+1}Ru_nO_{3n+1(n=1,2,3)}$ family I have investigated the interplay between the electronic structures and the hybridization of O $2p$ states by combining polarization dependent O-K ($2p$-$1s$ transition) XAS and RXES spectroscopies. The effects of the Ru-O layers (n) on the O sites, and in particular the role of the apical O, have been elucidated. Furthermore, I have shown that Sr $3d$ orbitals participate to the electronic structure across the Fermi energy through the direct hybridization with the $2p$ orbitals of the apical oxygens.

Bibliography

[1] Y Tokura. *Colossal Magnetoresistive Oxides*. Advances in Condensed Matter Science, Volume 2. CRC PressINC, 2000.

[2] Y Tokura and N Nagaosa. Orbital physics in transition-metal oxides. *Science*, 288(5465):462–468, 2000.

[3] D Huang, W Wu, G Guo, H-J Lin, T Hou, C Chang, C Chen, A Fujimori, T Kimura, H Huang, A Tanaka, and T Jo. Orbital Ordering in La0.5Sr1.5MnO4 Studied by Soft X-Ray Linear Dichroism. *Physical Review Letters*, 92(8), February 2004.

[4] JM Longo, PM Raccah, and JB Goodenough. Magnetic properties of SrRuO3 and CaRuO3. *Journal of Applied Physics*, 39(2):1327–1328, 1968.

[5] Y Maeno, H Hashimoto, K Yoshida, S NishiZaki, T Fujita, J G Bednorz, and F Lichtenberg. Superconductivity in a layered perovskite without copper. *Nature*, 372(6506):532–534, December 1994.

[6] P A Cox. *Transition Metal Oxides: An Introduction to Their Electronic Structure and Properties*. The International Series of Monographs on Chemistry. OUP Oxford, 1992.

[7] C N R Rao and B Raveau. *Transition Metal Oxides*. VCH, 1995.

[8] S N F Mott. *Metal-Insulator Transitions, 2nd Edition*. CRC PressINC, 1990.

[9] J. Hubbard. *Proc. Roy. Soc. Lond. A*, 276(238), 1963.

[10] C Zener. Interaction between the d-shells in the transition metals. ii. ferromagnetic compounds of manganese with perovskite structure. *Phys. Rev.*, 82:403–405, May 1951.

[11] C N R Rao and J Gopalakrishnan. *New Directions in Solid State Chemistry*. Cambridge University Press, 1997.

[12] A K Cheetham and P C Day. *Solid State Chemistry*. Oxford Science Publications. Clarendon Press, 1987.

[13] J B Goodenough. *Magnetism and the Chemical Bond*. Wiley, New York, 1963.

[14] J B Goodenough. Metallic oxides. *Progress in Solid State Chemistry*, 5:145 – 399, 1971.

[15] L J de Jongh and A R Miedema. *Adv Phys*, 23(1), 1974.

[16] A L Kuzemsky and I G Kuzemskaya. Structural sensitivity of superconducting properties of layered systems. *Physica C: Superconductivity and its Applications*, 383(1-2):140–158, 2002.

[17] N C Mishra and X Oudet. *Physica C*, 212:465, 1993.

[18] Jeroen van den Brink. Orbital-only models: ordering and excitations. *New Journal of Physics*, 6:201–201, January 2004.

[19] R Mathieu, M Uchida, Y Kaneko, J He, X Yu, R Kumai, T Arima, Y Tomioka, A Asamitsu, Y Matsui, and Y Tokura. Bandwidth-disorder phase diagram of half-doped layered manganites. *Physical Review B - Condensed Matter and Materials Physics*, 74(2), July 2006.

[20] T A Kaplan and S D Mahanti. *Physics of Manganites*. Kluwer Academic, 1999.

[21] Elbio Dagotto. Open questions in CMR manganites, relevance of clustered states and analogies with other compounds including the cuprates. *New Journal of Physics*, 7:67–67, January 2005.

[22] M.B. Salamon and M. Jaime. The physics of manganites: Structure and transport. *Reviews of Modern Physics*, pages 583–628, 2001.

[23] A P Ramirez. Colossal magnetoresistance. *J Phys: Condens Matter*, 9:8171–8199, September 1997.

[24] E. O. Wollan and W. C. Koehler. Neutron Diffraction Study of the Magnetic Properties of the Series of Perovskite-Type Compounds La1-xCaxMnO3. *Phys. Rev.*, 100:545–563, Oct 1955.

[25] Ryo Maezono, Sumio Ishihara, and Naoto Nagaosa. Orbital polarization in manganese oxides. *Phys. Rev. B*, 57:R13993–R13996, Jun 1998.

[26] S Ruddlesden and P Popper. *Acta Crystallogr.*, 11(541), 1958.

[27] H Moritomo Y Asamitsu, A Kuwahara and Y Tokura. Giant magnetoresistance of manganese oxides with a layered perovskite structure. *Nature*, 380:141, 1996.

[28] P D Battle, S J Blundell, M A Green, W Hayes, M Honold, A K Klehe, N S Laskey, J E Millburn, L Murphy, M J Rosseinsky, N A Samarin, J Singleton, N E Sluchanko, S P Sullivan, and J F Vente. Colossal magnetoresistance in Sr2-xNd1+xMn2O7 (x = 0.0, 0.1). *Journal of Physics: Condensed Matter*, 8(32):L427, 1996.

[29] John B. Goodenough. Theory of the Role of Covalence in the Perovskite-Type Manganites [La, M(II)]MnO_3. *Phys. Rev.*, 100:564–573, Oct 1955.

[30] Y. Okimoto, T. Katsufuji, T. Ishikawa, A. Urushibara, T. Arima, and Y. Tokura. Anomalous Variation of Optical Spectra with Spin Polarization in Double-Exchange Ferromagnet: La1-xSrxMnO3. *Phys. Rev. Lett.*, 75:109–112, Jul 1995.

[31] P. Schiffer, A. P. Ramirez, W. Bao, and S-W. Cheong. Low Temperature Magnetoresistance and the Magnetic Phase Diagram of La1-xCaxMnO3. *Phys. Rev. Lett.*, 75:3336–3339, Oct 1995.

[32] P. G. Radaelli, D. E. Cox, M. Marezio, and S-W. Cheong. Charge, orbital, and magnetic ordering in La0.5Ca0.5MnO3. *Phys. Rev. B*, 55:3015–3023, Feb 1997.

[33] T Mizokawa. Spin, charge, and orbital ordering in Mn perovskite oxides studied by model Hartree-Fock calculations. *Phys. Rev. B*, 56(2):1–4, June 1997.

[34] Tetsuya Mutou and Hiroshi Kontani. Charge-orbital stripe structure in $la_{1-x}ca_xmno_3$ ($x = 1/2, 2/3$). *Phys. Rev. Lett.*, 83:3685–3688, Nov 1999.

[35] Daniel Khomskii and Jeroen van den Brink. Anharmonic effects on charge and orbital order. *Phys. Rev. Lett.*, 85:3329–3329, Oct 2000.

[36] Priya Mahadevan, K Terakura, and D Sarma. Spin, Charge, and Orbital Ordering in La0.5Sr1.5MnO4. *Phys. Rev. Lett.*, 87(6), July 2001.

[37] Z Popović and S Satpathy. Origin of Charge-Orbital Order in the Half-Doped Manganites. *Phys. Rev. Lett.*, 88(19), April 2002.

[38] F.A. Lima, C.J. Milne, D.C.V. Amarasinghe, M.H. Rittmann-Frank, R.M.V.D. Veen, M. Reinhard, V.-T. Pham, S. Karlsson, S.L. Johnson, D Grolimund, C. Borca, T. Huthwelker, M. Janousch, F Van Mourik, R Abela, and M Chergui. A high-repetition rate scheme for synchrotron-based picosecond laser pumpx-ray probe experiments on chemical and biological systems in solution. *Review of Scientific Instruments*, 82(6):063111, 2011.

[39] Majed Chergui and Ahmed H Zewail. Electron and X-Ray Methods of Ultrafast Structural Dynamics: Advances and Applications. *ChemPhysChem*, 10(1):28–43, January 2009.

[40] C Bressler and M Chergui. Ultrafast X-ray absorption spectroscopy. *Chemical reviews*, 104(4):1781–1812, 2004.

[41] Yoshinori Tokura. Photoinduced Phase Transition: A Tool for Generating a Hidden State of Matter. *Journal of the Physical Society of Japan*, pages 1–3, December 2005.

[42] K. Miyano, T. Tanaka, Y. Tomioka, and Y. Tokura. Photoinduced insulator-to-metal transition in a perovskite manganite. *Phys. Rev. Lett.*, 78:4257–4260, Jun 1997.

[43] M Fiebig, K Miyano, Y Tomioka, and Y Tokura. Sub-picosecond photoinduced melting of a charge-ordered state in a perovskite manganite. *Applied Physics B*, 71(2):211–215, August 2000.

[44] Takeshi Ogasawara, Katsuhiro Tobe, Tsuyoshi Kimura, Hiroshi Okamoto, and Yoshinori Tokura. Photo-Induced Dynamics of Charge/Orbital Order in Perovskite Manganite Nd0.5Ca0.5MnO3. *Journal of the Physical Society of Japan*, 71(10):2380–2383, 2002.

[45] T M Rice and M Sigrist. Sr2RuO4: an electronic of 3He? *J. Phys.: Condens. Matter*, 7:L643, 1995.

[46] Zhong Fang, Kiyoyuki Terakura, and Naoto Nagaosa. Orbital physics in ruthenates: first-principles studies. *New Journal of Physics*, 7:66–66, January 2005.

[47] M Haverkort, I Elfimov, L Tjeng, G Sawatzky, and A Damascelli. Strong Spin-Orbit Coupling Effects on the Fermi Surface of Sr2RuO4 and Sr2RhO4. *Physical Review Letters*, 101(2):026406, July 2008.

[48] J Lee, Y Lee, T Noh, K Char, Jonghyurk Park, S-J Oh, J-H Park, C Eom, T Takeda, and R Kanno. Optical investigation of the electronic structures of Y2Ru2O7, CaRuO3, SrRuO3, and Bi2Ru2O7. *Physical Review B - Condensed Matter and Materials Physics*, 64(24):245107, December 2001.

[49] Y. S. Lee, Jaejun Yu, J. S. Lee, T. W. Noh, T.-H. Gimm, Han-Yong Choi, and C. B. Eom. Non-Fermi liquid behavior and scaling of the low-frequency suppression in the optical conductivity spectra of CaRuO3. *Phys. Rev. B*, 66:041104, Jul 2002.

[50] J. Okamoto, T. Mizokawa, A. Fujimori, I. Hase, M. Nohara, H. Takagi, Y. Takeda, and M. Takano. Correlation effects in the electronic structure of SrRuO3. *Phys. Rev. B*, 60:2281–2285, Jul 1999.

[51] S. Nakatsuji and Y. Maeno. Quasi-Two-Dimensional Mott Transition System Ca2-xSrxRuO4. *Phys. Rev. Lett.*, 84:2666–2669, Mar 2000.

[52] G. Cao, S. McCall, M. Shepard, J. E. Crow, and R. P. Guertin. Magnetic and transport properties of single-crystal Ca2RuO4: Relationship to superconducting Sr2RuO4. *Phys. Rev. B*, 56:R2916–R2919, Aug 1997.

[53] M. Braden, G. André, S. Nakatsuji, and Y. Maeno. Crystal and magnetic structure of Ca2RuO4: Magnetoelastic coupling and the metal-insulator transition. *Phys. Rev. B*, 58:847–861, Jul 1998.

[54] T. Mizokawa, L. H. Tjeng, G. A. Sawatzky, G. Ghiringhelli, O. Tjernberg, N. B. Brookes, H. Fukazawa, S. Nakatsuji, and Y. Maeno. Spin-Orbit Coupling in the Mott Insulator Ca2RuO4. *Phys. Rev. Lett.*, 87:077202, Jul 2001.

[55] S. Nakatsuji and Y. Maeno. Switching of magnetic coupling by a structural symmetry change near the Mott transition in Ca2-xSrxRuO4. *Phys. Rev. B*, 62:6458–6466, Sep 2000.

[56] Uwe Bergmann and Pieter Glatzel. X-ray emission spectroscopy. *Photosynthesis Research*, 102(2-3):255–266, August 2009.

[57] F de Groot and Kotani A. *Core Level Spectroscopy of Solids*. Taylor and Francis Group, 2008.

[58] F De Groot. High-Resolution X-ray Emission and X-ray Absorption Spectroscopy. *Chemical reviews*, July 2000.

[59] J. J. Rehr and R. C. Albers. Theoretical approaches to x-ray absorption fine structure. *Rev. Mod. Phys.*, 72:621–654, Jul 2000.

[60] P. A. Lee, P. H. Citrin, P. Eisenberger, and B. M. Kincaid. Extended x-ray absorption fine structure—its strengths and limitations as a structural tool. *Rev. Mod. Phys.*, 53:769–806, Oct 1981.

[61] J. and M.G. Samant. Liquid crystal alignment by rubbed polymer surfaces: a microscopic bond orientation model. *Journal of Electron Spectroscopy and Related Phenomena*, 98-99(0):189 – 207, 1999.

[62] Ali Oguz Er, Jie Chen, and Peter M Rentzepis. Ultrafast time resolved x-ray diffraction, extended x-ray absorption fine structure and x-ray absorption near edge structure. *Journal of Applied Physics*, 112(3):031101, 2012.

[63] J Workman, M Nantel, A Maksimchuk, and D Umstadter. Application of a picosecond soft x-ray source to time-resolved plasma dynamics. *Applied Physics Letters*, 70(3):312–314, 1997.

[64] F Ráksi, KR Wilson, Z Jiang, A Ikhlef, CY Côté, and J-C Kieffer. Ultrafast x-ray absorption probing of a chemical reaction. *Journal of Chemical Physics*, 104(15):6066–6069, 1996.

[65] Ferenc Raksi, Kent R Wilson, Zhiming Jiang, Abdelaziz Ikhlef, Christian Y Cote, and Jean-Claude Kieffer. Ultrafast 2.5-keV x-ray absorption probing of a chemical reaction with 3-ps time resolution. *Proceedings of SPIE - The International Society for Optical Engineering*, 2523:306–315, 1995.

[66] Y Okano, K Oguri, T Nishikawa, and H Nakano. Soft x-ray imaging system for picosecond time-resolved absorption spectroscopy using a femtosecond-laser-plasma source. *Review of Scientific Instruments*, 77:046105, 2006.

[67] K Oguri, Y Okano, T Nishikawa, and H Nakano. Dynamics of femtosecond laser ablation plume studied with ultrafast x-ray absorption fine structure imaging. *AIP Conference Proceedings*, 1278:656–664, 2010.

[68] H Nakano, K Oguri, Y Okano, and T Nishikawa. Picosecond time-resolved XAFS measurements using femtosecond laser-produced plasma soft x-ray as a probe. *Proceedings of SPIE - The International Society for Optical Engineering*, 6614, 2007.

[69] H Nakano, Y Goto, P Lu, T Nishikawa, and N Uesugi. Time-resolved soft x-ray absorption spectroscopy of silicon using femtosecond laser plasma x rays. *Applied Physics Letters*, 75(16):2350–2352, 1999.

[70] M Zangrando, M Zacchigna, M Finazzi, D Cocco, R Rochow, and F Parmigiani. Polarized high-brilliance and high-resolution soft x-ray source at ELETTRA: The performance of beamline BACH. *Review of Scientific Instruments*, 75(1):31–36, 2004.

[71] M Zangrando, M Finazzi, G Paolucci, G Comelli, B Diviacco, R P Walker, D Cocco, and F Parmigiani. BACH, the beamline for advanced dichroic and scattering experiments at ELETTRA. *Review of Scientific Instruments*, 72(2):1313–1319, 2001.

[72] Daniele Cocco. ComIXS on BACH: a compact soft x-ray spectrometer operating at Elettra. *AIP Conference Proceedings*, 705:873–876, February 2004.

[73] L. Galli. *Tesi di Laurea: Toward a comprehensive picture of the orbital polarization and the magnetic properties of ruthenates.* Universita' degli studi di Trieste, 2010.

[74] G Coslovich. *Tesi di Laurea: Disclosing the ultrafast dynamics of competing phases in high-temperature superconductors by time-resolved optical spectroscopy.* Universita' degli studi di Trieste, 2010.

[75] Mira Seed and Rega 9050. *manuals, Coherent Inc.*

[76] T Abebaw. *Master's thesis*.

[77] L. Stebel, M Malvestuto, V Capogrosso, P Sigalotti, B Ressel, F Bondino, E Magnano, G Cautero, and F Parmigiani. Time-resolved soft x-ray absorption setup using multi-bunch operation modes at synchrotrons. *Review of Scientific Instruments*, 82(12):123109, 2011.

[78] AM March, A Stickrath, G Doumy, Elliot Kanter, Bertold Krassig, S Southworth, K Attenkofer, C Kurtz, L Chen, and L Young. Development of high-repetition-rate laser pump/x-ray probe methodologies for synchrotron facilities. *Review of Scientific Instruments*, 82:073110, 2011.

[79] W Gawelda, VT Pham, M Benfatto, Y Zaushitsyn, M Kaiser, D Grolimund, SL Johnson, R Abela, A Hauser, and C Bressler. Structural determination of a short-lived excited iron (II) complex by picosecond x-ray absorption spectroscopy. *Physical Review Letters*, 98(5):57401, 2007.

[80] W Gawelda, M Johnson, FMF de Groot, R Abela, C Bressler, and M Chergui. Electronic and Molecular Structure of Photoexcited [RuII (bpy) 3] 2+ Probed by Picosecond X-ray Absorption Spectroscopy. *Journal of the American Chemical Society*, 128(15):5001–5009, 2006.

[81] W Gawelda, C Bressler, M Saes, M Kaiser, AN Tarnovsky, D Grolimund, SL Johnson, R Abela, and M Chergui. Picosecond time-resolved x-ray absorption spectroscopy of solvated organometallic complexes. *Physica Scripta T*, T115:102–106, 2005.

[82] M Saes, F Van Mourik, W Gawelda, M Kaiser, M Chergui, C Bressler, D Grolimund, R Abela, TE Glover, and PA Heimann. A setup for ultrafast time-resolved x-ray absorption spectroscopy. *Review of Scientific Instruments*, 75:24, 2004.

[83] C Bressler, M Saes, M Chergui, R Abela, and P Pattison. Optimizing a time-resolved X-ray absorption experiment. *Nucl. Instrum. Methods Phys. Res., A*, 467-468(1):1444–1446, 2001.

[84] C Bressler, M Saes, M Chergui, D Grolimund, R Abela, and P Pattison. Towards structural dynamics in condensed chemical systems exploiting ultrafast time-resolved x-ray absorption spectroscopy. *The Journal of Chemical Physics*, 116:2955, 2002.

[85] M Saes, C Bressler, R Abela, D Grolimund, SL Johnson, PA Heimann, and M Chergui. Observing photochemical transients by ultrafast x-ray absorption spectroscopy. *Phys. Rev. Lett.*, 90(4):474031–474034, 2003.

[86] L.X. Chen. Taking snapshots of photoexcited molecules in disordered media by using pulsed synchrotron X-rays. *Angewandte Chemie - International Edition*, 43(22):2886–2905, 2004.

[87] EM Dufresne, B Adams, M Chollet, R Harder, Y Li, H Wen, SJ Leake, L Beitra, X Huang, and IK Robinson. A technique for high-frequency laser-pump X-ray probe experiments at the APS. *Nuclear Instruments and Methods in Physics Research, Section A: Accelerators, Spectrometers, Detectors and Associated Equipment*, 2011.

[88] T Matsunaga, J Akola, S Kohara, T Honma, K Kobayashi, E Ikenaga, RO Jones, N Yamada, M Takata, and R Kojima. From local structure to nanosecond recrystallization dynamics in AgInSbTe phase-change materials. *Nature Materials*, 10(2):129–134, 2011.

[89] T. Gießel, D. Bröcker, P. Schmidt, and W. Widdra. Time-resolving and energy-dispersive photoelectron detector for combined laser and synchrotron radiation experiments. *Review of Scientific Instruments*, 74(11):4620–4624, 2003.

[90] JC Labiche, O Mathon, S Pascarelli, MA Newton, GG Ferre, C Curfs, G Vaughan, A Homs, and DF Carreiras. Invited article: The fast readout low noise camera as a versatile x-ray detector for time resolved dispersive extended x-ray absorption fine structure and diffraction studies of dynamic problems in materials science, chemistry, and catalysis. *Review of Scientific Instruments*, 78:091301, 2007.

[91] AM Lindenberg, I Kang, SL Johnson, T Missalla, PA Heimann, Z Chang, J Larsson, PH Bucksbaum, HC Kapteyn, and HA Padmore. Time-resolved x-ray diffraction from coherent phonons during a laser-induced phase transition. *Phys. Rev. Lett.*, 84(1):111–114, 2000.

[92] J Larsson, P A Heimann, A M Lindenberg, P J Schuck, P H Bucksbaum, R W Lee, H A Padmore, J S Wark, and R W Falcone. Ultrafast structural changes measured by time-resolved X-ray diffraction. *Applied Physics A: Materials Science and Processing*, 66(6):587–591, June 1998.

[93] C Rischel, A Rousse, I Uschmann, PA Albouy, JP Geindre, P Audebert, JC Gauthier, E Fröster, JL Martin, and A Antonetti. Femtosecond time-resolved X-ray diffraction from laser-heated organic films. *Nature*, 390(6659):490–492, 1997.

[94] Christopher P Barty, Ferenc Raksi, Christoph G Rose-Petruck, Kenneth J Schafer, Kent R Wilson, Vladislav V Yakovlev, Koichi Yamakawa, Zhiming Jiang, Abdelaziz Ikhlef, Christian Y Cote, and Jean-Claude Kieffer. Ultrafast x-ray absorption and diffraction. *Proceedings of SPIE - The International Society for Optical Engineering*, 2521:246–257, 1995.

[95] V Petkov, S Takeda, Y Waseda, and K Sugiyama. Structural study of molten germanium by energy-dispersive X-ray diffraction. *Journal of Non-Crystalline Solids*, 168(1-2):97–105, 1994.

[96] H Ichikawa, S Nozawa, T Sato, A Tomita, K Ichiyanagi, M Chollet, L Guerin, N Dean, A Cavalleri, S-I Adachi, T-H Arima, H Sawa, Y Ogimoto, M Nakamura, R Tamaki, K Miyano, and S-Y Koshihara. Transient photoinduced 'hidden' phase in a manganite. *Nature Materials*, 10(2):101–105, 2011.

[97] N. Bergeard, M.G. Silly, D. Krizmancic, C. Chauvet, M. Guzzo, J.P. Ricaud, M. Izquierdo, L. Stebel, P Pittana, R. Sergo, G Cautero, G. Dufour, F Rochet, and F. Sirotti. Time-resolved photoelectron spectroscopy using synchrotron radiation time structure. *Journal of Synchrotron Radiation*, 18(2):245–250, March 2011.

[98] *Hamamatsu Photonics, www.hamamatsu.com*. May 2008.

[99] E A Stern, D L Brewe, K M Beck, S M Heald, and Y Feng. Subnanosecond time resolved XAFS of laser excited thin Ge films. *Physica Scripta T*, T115:1044–1046, 2005.

[100] C Li, K Lu, Y Wang, K Tamura, S Hosokawa, and M Inui. Electronic structure study of liquid germanium based on x-ray-absorption near-edge structure spectroscopy. *Physical Review B*, 59(3):1571–1574, 1999.

[101] A. Di Cicco, B. Giovenali, R. Gunnella, E. Principi, and S. Simonucci. Metallization of the Ge(111) surface at high-temperature probed by energy-loss and Auger spectroscopies. *Solid State Communications*, 134(9):577–582, 2005.

[102] A. Filipponi and A. Di Cicco. Short-range order in crystalline, amorphous, liquid, and supercooled germanium probed by x-ray-absorption spectroscopy. *Phys. Rev. B*, 51:12322–12336, May 1995.

[103] A Filipponi, VM Giordano, and Marco Malvestuto. Lattice expansion and ge solubility in the ag1-vGev terminal solid solution. *Physica Status Solidi (B) Basic Research*, 234(2):496–505, 2002.

[104] A Goldoni, A. Santoni, M. Sancrotti, V.R. Dhanak, and S. Modesti. Photoemission and photoabsorption study of the high-temperature phases of the Ge(111) surface. *Surface Science*, 382(1-3):336–348, 1997.

[105] S.R. Stiffler, M.O. Thompson, and P.S. Peercy. Nucleation of amorphous germanium from supercooled melts. *Applied Physics Letters*, 56(11):1025–1027, 1990.

[106] A Filipponi, M Borowski, and F Natali. Multiple-scattering x-ray absorption investigation of the local structure around substitutional Ge impurities in Ag. *Physical Review B*, 60(1):6–9, 1999.

[107] P Castrucci, R. Gunnella, M. De Crescenzi, M Sacchi, G. Dufour, and F Rochet. Electronic density of empty states of Ge/Si(111) epitaxial layers: Theory and experiment. *Phys. Rev. B*, 60(8):5759–5769, 1999.

[108] S Cottenier. *Density Functional Theory and the Family of (L)APW-methods: a step-by-step introduction*. 2004.

[109] V I Anisimov, J Zaanen, and O K Andersen. Band theory and Mott insulators: Hubbard U instead of Stoner I. *Phys. Rev. B*, 44(3):943–954, 1991.

[110] P Blaha and K Schwarz. *WIEN2k,User's Guide, www.wien2k.at*. 2011.

[111] P E Blöchl, O Jepsen, and O K Andersen. Improved tetrahedron method for Brillouin-zone integrations. *Phys. Rev. B*, 49(23):16223, 1994.

[112] A. Neckel and K Schwarz. *Microchim. Acta, Suppl.6, 257*, 1975.

[113] K Schwarz and A Neckel. *J.Phys.F:Metal Phys. 9, 2509*, 1979.

[114] K Schwarz and E Wmmer. *J.Phys.F:Metal Phys. 10, 1001*, 1980.

[115] D. Okuyama, Y. Tokunaga, R Kumai, Y. Taguchi, T Arima, and Y Tokura. Lattice-form-dependent orbital shape and charge disproportionation in charge- and orbital-ordered manganites. *Physical Review B - Condensed Matter and Materials Physics*, 80(6):064402, 2009.

[116] I S Elfimov, V I Anisimov, and G A Sawatzky. Orbital ordering, Jahn-Teller distortion, and anomalous x-ray scattering in manganates. *Physical Review Letters*, 82(21):4264–4267, 1999.

[117] M. Imada, A Fujimori, and Y Tokura. Metal-insulator transitions. *Reviews of Modern Physics*, 70(4 PART I):1039–1263, 1998.

[118] Y Tokura. Orbital Physics in Transition-Metal Oxides. *Science*, 288(5465):462–468, April 2000.

[119] M Ibarra, R Retoux, M Hervieu, C Autret, A Maignan, C Martin, and B Raveau. Charge–orbital ordering above room temperature in the 2D Pr1-xCa1+xMnO4 manganites. *Journal of Solid State Chemistry*, 170(2):361–367, February 2003.

[120] K S Chao, D J Huang, J Okamoto, H-J Lin, C-H Hsu, Y Kaneko, R Mathieu, W B Wu, Y Tokura, and C T Chen. Orbital ordering of layered manganites from resonant soft X-ray scattering. *Journal of Magnetism and Magnetic Materials*, 310(2):819–821, March 2007.

[121] S Chi, F Ye, P Dai, J A Fernandez-Baca, Q Huang, J W Lynn, E W Plummer, R Mathieu, Y Kaneko, and Y Tokura. Effect of antiferromagnetic spin correlations on lattice distortion and charge ordering in Pr0.5Ca1.5MnO4. In *Proceedings of the National Academy of Sciences of the United States of America*, pages 10796–10801, 2007.

[122] F Ye, S Chi, J A Fernandez-Baca, A. Moreo, E Dagotto, J W Lynn, R Mathieu, Y Kaneko, Y Tokura, and P Dai. Electronic Self-Organization in the single-layer manganite Pr1-xCa1+xMnO4. *Physical Review Letters*, 103(16), 2009.

[123] V Capogrosso, M Malvestuto, I P Handayani, P H M van Loosdrecht, A A Nugroho, E Magnano, and F Parmigiani. Effects of charge-orbital order-disorder phenomena on the unoccupied electronic states in the single layered half doped Pr0.5Ca1.5MnO4. *Phys. Rev. B*, accepted 2013.

[124] M Merz, P Reutler, B Büchner, D Arena, J Dvorak, Y U Idzerda, S Tokumitsu, and S Schuppler. O1s and Mn2p NEXAFS on single-layered La1-xSr1+xMnO4: crystal field effect versus orbital coupling mechanism. *The European Physical Journal B*, 51(3):315–319, June 2006.

[125] M Merz, G Roth, P Reutler, B Büchner, D Arena, J Dvorak, Y Idzerda, S Tokumitsu, and S Schuppler. Orbital degree of freedom in single-layered La1-xSr1+xMnO4: Doping- and temperature-dependent rearrangement of orbital states. *Physical Review B - Condensed Matter and Materials Physics*, 74(18):184414, November 2006.

[126] W B Wu, D J Huang, G Y Guo, H-J Lin, T Y Hou, C F Chang, C T Chen, A Fujimori, T Kimura, H B Huang, A Tanaka, and T Jo. Orbital polarization of LaSrMnO4 studied by soft X-ray linear dichroism. *Journal of Electron Spectroscopy and Related Phenomena*, 137-140:641–645, July 2004.

[127] M Platé, F Bondino, M Zacchigna, M Zangrando, I Alessandri, M Affronte, L Malavasi, and F Parmigiani. Lattice effects in the ferromagnetic insulating phase of manganites. *Physical Review B - Condensed Matter and Materials Physics*, 72(8), 2005.

[128] Javier Herrero-Martín, Joaquín García, Gloria Subías, Javier Blasco, and María Sánchez. Polarized x-ray absorption spectra of La1-xSr1+xMnO4: Electronic state of Mn atoms. *Physical Review B - Condensed Matter and Materials Physics*, 72(8), 2005.

[129] G. Subías, J. García, M.C. Sánchez, J. Blasco, and M.G. Proietti. Soft x-ray absorption spectroscopy (Mn L2,3 and O K) in mixed valence manganites. *Surface Review and Letters*, 9(2):1071–1078, 2002.

[130] K Kuepper, F Bondino, K C Prince, M Zangrando, M Zacchigna, A F Takács, T Crainic, M Matteucci, F Parmigiani, A Winiarski, V R Galakhov, Ya M Mukovskii, and M Neumann. Direct Investigation of Orbital Ordering in a Colossal Magnetoresistance Manganite by Means of X-ray Linear Dichroism at the Mn LEdge. *J. Phys. Chem. B*, 109(33):15667–15670, August 2005.

[131] J-H Park, T Kimura, and Y Tokura. Competition between lattice distortion and charge dynamics for the charge carriers of double-layered manganites. *Physical Review B*, 58(20):R13330–R13333, 1998.

[132] F M F de Groot, J.C. Fuggle, B.T. Thole, and G A Sawatzky. 2p x-ray absorption of 3d transition-metal compounds: An atomic multiplet description including the crystal field. *Physical Review B*, 42(9):5459–5468, 1990.

[133] FMF de Groot, M Grioni, JC Fuggle, J Ghijsen, GA Sawatzky, and H Petersen. Oxygen 1s X-ray-absorption edges of transition-metal oxides. *Physical Review B*, 40(8):5715–5723, 1989.

[134] J Stohr, K Baberschke, R Jaeger, R Treichler, and S Brennan. Orientation of chemisorbed molecules from surface-absorption fine-structure measurements: CO and NO on Ni (100). *Physical Review Letters*, 47(5):381–384, 1981.

[135] F M F de Groot. X-ray absorption and dichroism of transition metals and their compounds. *Journal of Electron Spectroscopy and Related Phenomena*, 67(4):529–622, August 1994.

[136] C Aruta, G Ghiringhelli, A Tebano, N Boggio, N Brookes, P Medaglia, and G Balestrino. Strain induced x-ray absorption linear dichroism in La0.7Sr0.3MnO3 thin films. *Physical Review B*, 73(23), June 2006.

[137] M Grioni, M.T. Czyzyk, F M F de Groot, J.C. Fuggle, and B E Watts. Unoccupied electronic states of CuO: An oxygen 1s x-ray-absorption spectroscopy investigation. *Physical Review B*, 39(8):4886–4890, 1989.

[138] I.P. Handayani; P.H.M. van Loosdrecht et al. Private communication.

[139] J-H Park, C T Chen, S-W Cheong, W Bao, G Meigs, V Chakarian, and Y U Idzerda. Electronic aspects of the ferromagnetic transition in manganese perovskites. *Physical Review Letters*, 76(22):4215–4218, 1996.

[140] K Horiba, H Kawanaka, Y Aiura, T Saitoh, C Satoh, Y Kikuchi, M Yokoyama, Y Nishihara, R Eguchi, Y Senba, H Ohashi, Y Kitajima, and S Shin. Electronic structure of SrRu1-xMnxO3 studied by photoemission and x-ray absorption spectroscopy. *Physical Review B - Condensed Matter and Materials Physics*, 81(24), 2010.

[141] Hua Wu, C Chang, O Schumann, Z Hu, J Cezar, T Burnus, N Hollmann, N Brookes, A Tanaka, M Braden, L Tjeng, and D Khomskii. Orbital order in La_0.5Sr_1.5MnO_4: Beyond a common local Jahn-Teller picture. *Physical Review B*, 84(15):155126, 2011.

[142] G. Zampieri, M Abbate, F. Prado, A. Caneiro, and E. Morikawa. XPS and XAS spectra of CaMnO3 and LaMnO3. *Physica B: Condensed Matter*, 320(1-4):51–55, 2002.

[143] O. Toulemonde, F. Millange, F. Studer, B Raveau, J-H Park, and C T Chen. Changes in the Jahn-Teller distortion at the metal-insulator transition in CMR manganites (Pr, Nd) 0.7(Sr, Ca) 0.3MnO 3. *Journal of physics condensed matter*, 11(1):109–120, 1999.

[144] K.B. Garg, N.L. Saini, B R Sekhar, R K Singhal, B Doyle, S Nannarone, F Bondino, E Magnano, E Carleschi, and T Chatterji. Doped holes and Mn valence in manganites: a polarized soft x-ray absorption study of LaMnO 3and quasi-2D manganite systems. *Journal of physics condensed matter*, 20(5):055215, January 2008.

[145] M Abbate, J Fuggle, A Fujimori, L Tjeng, C Chen, R Potze, G Sawatzky, H Eisaki, and S Uchida. Electronic structure and spin-state transition of LaCoO3. *Physical Review B - Condensed Matter and Materials Physics*, 47(24):16124–16130, June 1993.

[146] M Abbate, F M F de Groot, J.C. Fuggle, O Strebel, F Lopez, M Domke, G Kaindl, G A Sawatzky, M Takano, Y Takeda, H Eisaki, and S Uchida. Controlled-valence properties of La1-xSrxFeO3 and La1-xSrxMnO3 studied by soft-x-ray absorption spectroscopy. *Physical Review B - Condensed Matter and Materials Physics*, 46(8):4511–4519, August 1992.

[147] J. Herrero-Martín, A Mirone, J Fernández-Rodríguez, P Glatzel, J. García, J. Blasco, and J Geck. Hard x-ray probe to study doping-dependent electron redistribution and strong covalency La1-xSr1+xMnO4. *Physical Review B*, 82(7):075112, 2010.

[148] C Aruta, C Adamo, A Galdi, P Orgiani, V Bisogni, N Brookes, J Cezar, P Thakur, C Perroni, G De Filippis, V Cataudella, D Schlom, L Maritato, and G Ghiringhelli. Evolution of magnetic phases and orbital occupation in (SrMnO3)n/(LaMnO3)2n superlattices. *Physical Review B*, 80(14):140405, 2009.

[149] F Bondino, M Platé, M Zangrando, M Zacchigna, D Cocco, A Comin, I Alessandri, L Malavasi, and F Parmigiani. Doping Dependence of the Electronic Structure of La1-xNa xMnO3 by Resonant X-ray Emission and X-ray Absorption Spectroscopy. *Journal of Physical Chemistry B*, 108(13):4018–4023, 2004.

[150] K Nasu. *Photoinduced Phase Transitions*. World Scientific, 2004.

[151] Shin ya Koshihara and Shin ichi Adachi. Photo-induced phase transition in an electron–lattice correlated system —future role of a time-resolved x-ray measurement for materials science—. *Journal of the Physical Society of Japan*, 75(1):011005, 2006.

[152] P. Huai and Keiichiro Nasu. Difference between photoinduced phase and thermally excited phase. *Journal of the Physical Society of Japan*, 71(4):1182–1188, 2002.

[153] H Shaked, JD Jorgensen, O Chmaissem, S Ikeda, and Y Maeno. Neutron diffraction study of the structural distortions in Sr3Ru2O7. *Journal of Solid State Chemistry*, 154(2):361–367, 2000.

[154] M Crawford, R Harlow, W Marshall, Z Li, G Cao, R Lindstrom, Q Huang, and J Lynn. Structure and magnetism of single crystal Sr4Ru3O10: A ferromagnetic triple-layer ruthenate. *Physical Review B*, 65(21), May 2002.

[155] E Gorelov, M Karolak, T O Wehling, F Lechermann, A I Lichtenstein, and E. Pavarini. Nature of the Mott Transition in Ca2RuO4. *Physical Review Letters*, 104(22), June 2010.

[156] N E Hussey, A P Mackenzie, J R Cooper, Y Maeno, S NishiZaki, and T Fujita. Normal-state magnetoresistance of Sr2RuO4. *Physical Review B*, 57(9):5505–5511, 1998.

[157] Ikeda, Y Maeno, S Nakatsuji, M Kosaka, and Y Uwatoko. Ground state in Sr_ 3 Ru_ 2 O_ 7: Fermi liquid close to a ferromagnetic instability. *Physical Review B - Condensed Matter and Materials Physics*, 2000.

[158] A P Mackenzie, R K W Haselwimmer, A W Tyler, G G Lonzarich, Y Mori, S NishiZaki, and Y Maeno. Extremely strong dependence of superconductivity on disorder in Sr2RuO4. *Physical Review Letters*, 80(1):161–164, 1998.

[159] Z Q Mao, Y Mori, and Y Maeno. Suppression of superconductivity in Sr2RuO4 caused by defects. *Physical Review B*, 60(1):610–614, 1999.

[160] A Mackenzie and Y Maeno. The superconductivity of Sr2RuO4 and the physics of spin-triplet pairing. *Reviews of Modern Physics*, 2003.

[161] Q Huang, J W Lynn, R W Erwin, J Jarupatrakorn, and R J Cava. Oxygen displacements and search for magnetic order in Sr3Ru2O7. *Physical Review B*, 58(13):8515–8521, 1998.

[162] M Iliev, V Popov, A Litvinchuk, M Abrashev, J Backstrom, Y Sun, R Meng, and C Chu. Comparative Raman studies of , and. *Physica B: Condensed Matter*, 358(1-4):138–152, April 2005.

[163] J Hooper, M Fang, M Zhou, D Fobes, N Dang, Z Mao, C Feng, Z Xu, M Yu, C Oconnor, G Xu, N Andersen, and M Salamon. Competing magnetic fluctuations in Sr3Ru2O7 probed by Ti doping. *Physical Review B - Condensed Matter and Materials Physics*, 75(6):060403, February 2007.

[164] K Kitagawa, K Ishida, R Perry, T Tayama, T Sakakibara, and Y Maeno. Metamagnetic Quantum Criticality Revealed by O17-NMR in the Itinerant Metamagnet Sr3Ru2O7. *Physical Review Letters*, 95(12):127001, September 2005.

[165] MB Stone, MD Lumsden, R Jin, BC Sales, D Mandrus, SE Nagler, and Y Qiu. Temperature-dependent bilayer ferromagnetism in Sr3Ru2O7. *Physical Review B - Condensed Matter and Materials Physics*, 73(17), 2006.

[166] L Capogna, EM Forgan, SM Hayden, A Wildes, JA Duffy, AP Mackenzie, RS Perry, S Ikeda, Y Maeno, and SP Brown. Observation of two-dimensional spin fluctuations in the bilayer ruthenate Sr3Ru2O7 by inelastic neutron scattering. *Physical Review B - Condensed Matter and Materials Physics*, 67(1):125041–125044, 2003.

[167] SA Grigera, RA Borzi, AP Mackenzie, SR Julian, RS Perry, and Y Maeno. Angular dependence of the magnetic susceptibility in the itinerant metamagnet Sr3Ru2O7. *Physical Review B - Condensed Matter and Materials Physics*, 67(21):2144271–2144278, 2003.

[168] S A Grigera. Disorder-Sensitive Phase Formation Linked to Metamagnetic Quantum Criticality. *Science*, 306(5699):1154–1157, November 2004.

[169] R Perry, L Galvin, S Grigera, and L Capogna. Metamagnetism and Critical Fluctuations in High Quality Single Crystals of the Bilayer Ruthenate Sr3Ru2O7. *Physical Review Letters*, 2001.

[170] G Cao, L Balicas, W H Song, Y P Sun, Y Xin, V A Bondarenko, J W Brill, S Parkin, and X N Lin. Competing ground states in triple-layered Sr_4Ru_3O_10: Verging on itinerant ferromagnetism with critical fluctuations. *Physical Review B - Condensed Matter and Materials Physics*, 68(17):7, November 2003.

[171] W Bao, Z Mao, M Zhou, J Hooper, and J Lynn. Magnetic transition and magnetic structure of Sr4Ru3O10. *Arxiv preprint cond-mat*, 2006.

[172] R Gupta, M Kim, H Barath, S L Cooper, and G Cao. Field- and Pressure-Induced Phases in Sr4Ru3O10: A Spectroscopic Investigation. *Phys. Rev. Lett.*, 96:067004, Feb 2006.

[173] M Malvestuto, E Carleschi, R Fittipaldi, E Gorelov, E. Pavarini, M Cuoco, Y Maeno, F Parmigiani, and A Vecchione. Electronic structure trends in the Srn+ 1RunO3n+ 1 family (n= 1, 2, 3). *Phys. Rev. B*, 83(16):165121, 2011.

[174] A Kotani and S Shin. Resonant inelastic x-ray scattering spectra for electrons in solids. *Reviews of Modern Physics*, 2001.

[175] K Okada and A Kotani. Theory of oxygen 1s resonant X-ray emission spectroscopy in copper-based oxides. *Journal of Synchrotron Radiation*, 8(2):243–245, 2001.

[176] A Kotani. Theory of resonant X-ray emission spectra in strongly correlated electron systems. *Journal of Electron Spectroscopy and Related Phenomena*, 110:197–212, 2000.

[177] J A Carlisle, E L Shirley, L J Terminello, E A Hudson, J J Jia, T A Callcott, F J Himpsel, D L Ederer, and R.C.C. Perera. Resonant soft x-ray fluorescence studies of novel materials. In *Materials Research Society Symposium - Proceedings*, pages 15–20, 1995.

[178] S.M. Butorin, J. Guo, N Wassdahl, and E.J. Nordgren. Tunable-excitation soft X-ray fluorescence spectroscopy of high-Tc superconductors: An inequivalent-site seeing story. *Journal of Electron Spectroscopy and Related Phenomena*, 110:235–273, 2000.

[179] Z Q Mao, Y. Maenoab, and H Fukazawa. Crystal growth of Sr2RuO4. *Materials Research Bulletin*, 35(11):1813–1824, 2000.

[180] Rosalba Fittipaldi, Daniela Sisti, Antonio Vecchione, and Sandro Pace. Crystal Growth of a Lamellar Sr3Ru2O7–Sr4Ru3O10 Eutectic System. *Crystal Growth & Design*, 7(12):2495–2499, December 2007.

[181] RS Perry and Y Maeno. Systematic approach to the growth of high-quality single crystals of Sr3Ru2O7. *Journal of Crystal Growth*, 271(1-2):134–141, 2004.

[182] M Zhou, J Hooper, D Fobes, Z Mao, V Golub, and C Oconnor. Electronic and magnetic properties of triple-layered ruthenate SrRuO single crystals grown by a floating-zone method. *Materials Research Bulletin*, 40(6):942–950, June 2005.

[183] D Cocco, M Matteucci, KC Prince, and M Zangrando. ComIXS: A compact inelastic x-ray spectrometer. *Proceedings of SPIE - The International Society for Optical Engineering*, 4506:46–55, 2001.

[184] M Schmidt, T R Cummins, M Bürk, D H Lu, N Nücker, S Schuppler, and F Lichtenberg. Nature of the electronic states in the layered perovskite noncuprate superconductor Sr 2RuO 4. *Phys. Rev. B*, 53(22):R14761–R14764, 1996.

[185] E Z Kurmaev, S. Stadler, D L Ederer, Y Harada, S Shin, M.M. Grush, T A Callcott, R.C.C. Perera, D.A. Zatsepin, N. Ovechkina, M Kasai, Y Tokura, T Takahashi, K. Chandrasekaran, R. Vijayaraghavan, and U.V. Varadaraju. Electronic structure of Sr2RuO4: X-ray fluorescence emission study. *Phys. Rev. B*, 57(3):1558–1562, 1998.

List of publications

- ***Time-resolved soft x-ray absorption setup using multi-bunch operation modes at synchrotrons***

  Authors: L. Stebel, M. Malvestuto, V. Capogrosso, P. Sigalotti, B. Ressel, F. Bondino, E. Magnano, G. Cautero, and F. Parmigiani

  Review of Scientific Instruments 82, 123109, Published 16 December 2011

- ***Effects of charge-orbital order-disorder phenomena on the unoccupied and electronic states in the single layered half doped*** $Pr_{0.5}Ca_{1.5}MnO_4$

  Authors: V. Capogrosso, M. Malvestuto, I. P. Handayani, P. H. M. van Loosdrecht, A. A. Nugroho, E. Magnano, and F. Parmigiani

  Accepted in Phys. Rev. B

- ***Resonant x-ray emission study of the*** $Sr_{n+1}Ru_nMnO_{3n+1}$ ***(n=1,2,3) family: role of the apical and planar oxygen sites***

  Authors: M. Malvestuto, V. Capogrosso, L. Galli, E. Gorelov, E. Pavarini, E. Carleschi, E. Magnano, M. Yablonskikh, R. Fittipaldi, M. Cuoco, Y. Maeno, A. Vecchione, and F. Parmigiani

  In preparation